POST PLASMA ETCH RESIDUE REMOVAL USING CARBON DIOXIDE BASED FLUIDS

A Dissertation
Presented to
The Academic Faculty

By

Satyanarayana Myneni

In Partial Fulfillment
Of the Requirements for the Degree
Doctor of Philosophy in Chemical Engineering

Georgia Institute of Technology
December 2004

POST PLASMA ETCH RESIDUE REMOVAL USING CARBON DIOXIDE BASED FLUIDS

Approved by:

Dr. Dennis W. Hess, Advisor (ChBE)

Dr. Charles A. Eckert (ChBE)

Dr. Charles L. Liotta (CHEM)

Dr. J. Carson Meredith (ChBE)

Dr. Amyn S. Teja (ChBE)

October 13, 2004

ACKNOWLEDGEMENTS

First of all, I would like to thank my advisor Dr. Dennis Hess for his guidance and support during this research. His extensive knowledge of this area and constant encouragement has been invaluable for the successful completion of this project. The best thing I liked about working with Dr. Hess was that he was always available to guide my research while encouraging me to pursue independent ideas. He has always encouraged critical thinking and attention to details of any problem without losing focus of the bigger picture. I also want to thank Dr. Charles Eckert, Dr. Charles Liotta, Dr. Carson Meredith, and Dr. Amyn Teja for serving on my committee and providing valuable suggestions during this work. Funding for this work has been provided by Novellus Systems, Inc., and National Center for Environmental Research STAR program (EPA contract no. R-82955401) and is greatly appreciated. I also want to thank Novellus Systems, Inc. for providing low-*k* etch residue samples.

This work would not have been complete without direct contribution from Dr. Galit Levitin. In addition to performing phase behavior measurements, she has provided experimental assistance and valuable suggestions throughout the project. I am grateful to her for being a great mentor and a friend. I want to thank every member, present and past, of Dr. Hess's research group for helping me with ideas and making life at graduate school a very enjoyable and memorable experience. In particular, many thanks to Chris Timmons for helping me with setting up equipment and for brainstorming with me, to Jie Diao for help with cleanroom processing and providing the code for ARXPS, and to Sudeep Vaswani for depositing fluorocarbon films in his plasma reactor.

During this research, I have obtained assistance from several faculty and research groups. I am grateful to Dr. Charles Eckert, Dr. Cliff Henderson, Dr. Paul Kohl, Dr. Amyn Teja, and Dr. Brent Carter (MSE) for allowing me to use the equipment in their labs. I want to thank Dr. David Gidley and his graduate student Huagen Peng at University of Michigan for performing the PALS measurements. I also want to thank the staff at Microelectronics Research Center (in particular Gary Spinner and Scott Fowler) for always willing to help with any equipment related issues. Many thanks also to Linda Perry and Gloria Beale of ChBE for placing countless purchase orders that allowed my work to run smoothly. Jeff Andrews of the ChBE machine shop has fabricated the optical window assembly and the ATR-FTIR cell, which made all my *in-situ* experiments possible.

I want to thank all my friends at Georgia Tech for providing great company and a balance between work and life. In particular, many thanks to Suraj Nair and Rajesh Rajaram for putting up with me for four years as roommates. Finally, I want to thank my family. My parents have made great sacrifices to provide me with the best possible education and family environment. They have always had great faith in me and have supported me during every step of my life. I have received moral support and constant encouragement from every member of my family, including my sister and brother-in-law, which made this research possible.

TABLE OF CONTENTS

LIST OF FIGURES

LIST OF TABLES

SUMMARY

As feature sizes in semiconductor devices become smaller and newer materials are incorporated, current methods for photoresist and post plasma etch residue removal face several challenges. A cleaning process should be environmentally benign, compatible with dielectric materials and copper, and provide residue removal from narrow and high aspect ratio features. In this work, sub-critical CO_2 based mixtures have been developed to remove the etch residues; these mixtures satisfy the above requirements and can potentially replace the two step residue removal process currently used in the integrated circuit (IC) industry.

Based on the chemical nature of the residue being removed, additives or co-solvents to CO_2 have been identified that can remove the residues without damaging the dielectric layers. Using the phase behavior of these additives as a guide, the composition of the co-solvent was altered to achieve a single liquid phase at moderate pressures without compromising cleaning ability. The extent of residue removal has been analyzed primarily by x-ray photoelectron spectroscopy (XPS) and scanning electron microscopy (SEM). A treatment in tetramethylammonium bicarbonate (0.6 mole%), methanol (29.3 mole%) and CO_2 (70.1 mole%) mixture (followed by a rinse step in methanol) removed the etch residues completely within 15 min at 70 ^{o}C.

Various techniques such as attenuated total reflection - Fourier transform infrared (ATR-FTIR) spectroscopy, angle-resolved XPS (ARXPS), and interferometry were used to probe the interaction of cleaning fluids with residues. Model films of photoresists and plasma deposited residues were used to assist in understanding the mechanism of residue

removal. From these studies, it was concluded that residue removal takes place primarily by attack of the interface between the residue and the substrate; a solvent rinse then lifts these residues from the wafer. It has been shown that transport of the additives to the interface is enhanced in the presence of CO_2. From positronium annihilation lifetime spectroscopy (PALS) studies on a porous dielectric film, it has been shown that these high pressure fluids do not cause significant changes to the pore sizes or the bonding structure of the film. Hence, this method can be used to remove post etch residues from low-*k* dielectric films.

CHAPTER 1

INTRODUCTION

Semiconductor devices have transformed society in the last five decades by enabling rapid advances in communication, personal computing, and scientific endeavor. Tremendous improvements in fabrication technology and materials have resulted in integrated circuit (IC) devices with smaller features, greater functionality and lower cost. The first transistor developed at Bell Labs in 1947 measured about one inch in size [1], whereas the present state-of-the-art transistor in production is $<1\ \mu m^2$ in size and costs $<10^{-5}$ $ [2]. The progression of minimum feature size (also referred to as device generation) and functionality (number of transistors) in Intel microprocessors over a period of ten years is shown in Figure 1.1 [3]. By continuously scaling down device sizes, the IC industry strives to keep up with a prediction by Gordon E. Moore that the number of devices in a chip doubles every 18-24 months [4].

IC fabrication is done in a layer-by-layer approach in which the devices are fabricated bottom-up by a series of repetitive processing steps such as ion implantation, photolithography, etching, deposition, and metallization [5]. Millions of these devices (both active and passive) are fabricated simultaneously on a wafer resulting in economy of scale. After the fabrication, the individual circuits are diced, tested, and packaged to provide resistance to the external environment. Scaling not only enables the packing of

more devices on a wafer or more transistors per device, but also leads to less power consumption and faster devices. To overcome the challenges in device operation and fabrication as scaling progresses, newer materials and processing methodologies are implemented. For example, copper and dual damascene processing have replaced aluminum and subtractive approaches previously used for metallization. The silicon based metal oxide semiconductor (MOS) transistors have the potential for terascale integration (TSI, more than 1 trillion transistors per chip) and scaling to the 10 nm generation provided that practical challenges related to manufacturing technology and costs are overcome [6]. The International Technology Roadmap for Semiconductors (ITRS) serves as a guide to the IC industry by proposing technologies necessary to keep

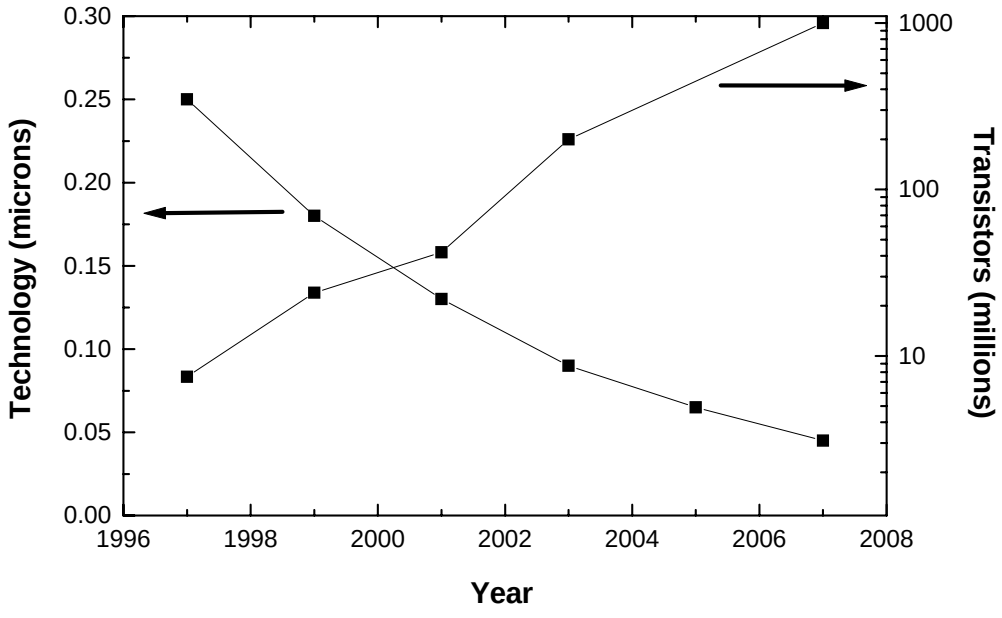

Figure 1.1. Progression of technology node and number of transistors in Intel's microprocessors [3].

pace with Moore's law [7].

One of the key enabling technologies to device scaling is lithography. Lithography is the art of patterning a thin film by selective etching and deposition in specific regions defined by exposing a radiation sensitive material (photoresist) to UV radiation through a mask [8]. Following the exposure, the photoresist is developed to remove the exposed (positive) or masked (negative) areas as illustrated in Figure 1.2. The pattern is then transferred to the underlying film by wet or dry (plasma) etching. Because of the requirements for anisotropy and etching narrow features, a plasma or glow discharge is used to remove portions of film in the form of volatile products [9]. During this process, the photoresist serves as a mask and prevents etching in the undesired areas. The photoresist undergoes modification as a result of exposure to the etch plasma. A thin residual (often a fluorocarbon) film is also deposited on the sidewalls of the features being etched which results in pattern anisotropy. Following the etch step, the photoresist and the etch residues are removed. This cleaning step follows every plasma patterning step and hence occurs more than 20 times in 90 nm complementary metal oxide semiconductor (CMOS) device fabrication [10]. Incomplete removal of these residues could lead to yield loss and performance degradation of the devices.

Currently, the residues are removed by 'ashing' in a downstream oxygen-based plasma (comprising only radicals and neutrals) [11] followed by another liquid 'stripping' step to remove the tough residues left behind in the ashing process. Because of the low cost of plasma ashing and the efficiency of liquid strippers, the industry has had continued success with this approach. However, this approach faces several

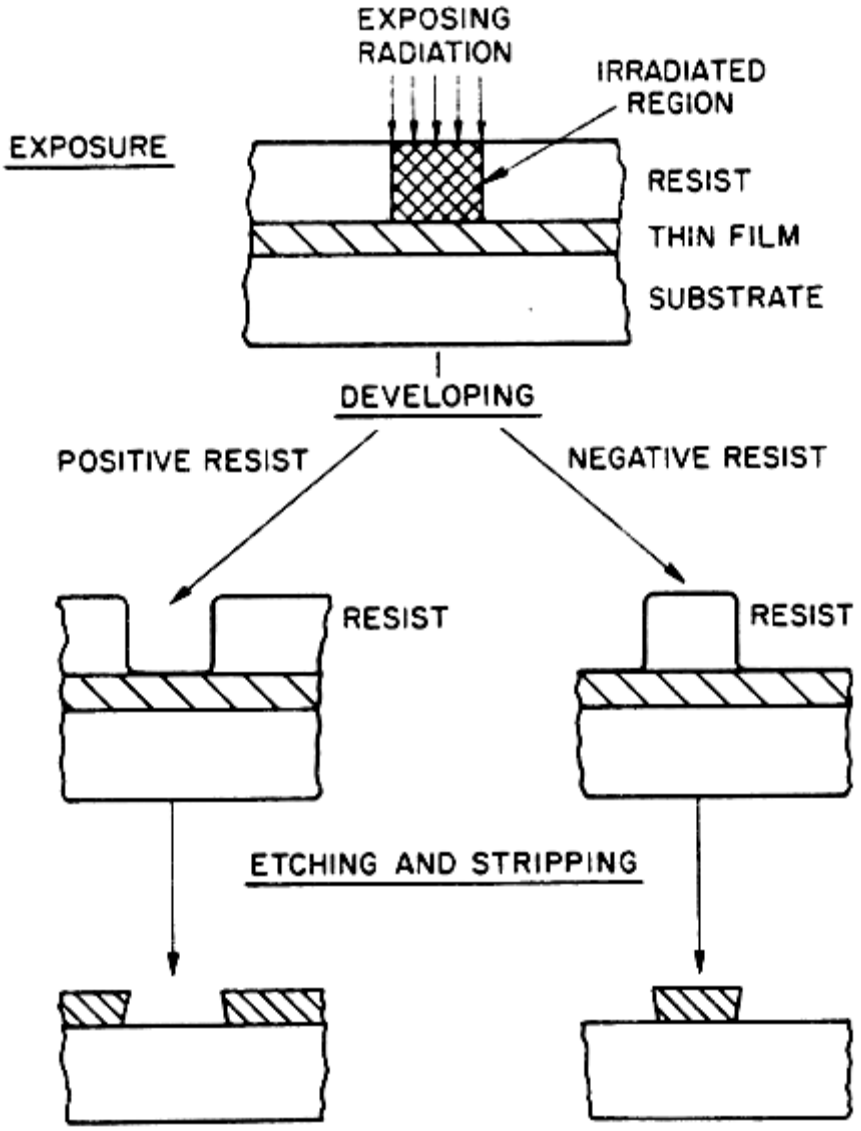

Figure 1.2. Illustration of lithography process used to pattern planar layers in IC fabrication [8].

challenges as devices are scaled to smaller dimensions. The presence of organic low-*k* dielectric films preclude the use of oxidizing plasmas to ash the residues because of possible damage to the dielectric. Reducing plasmas such as N_2/H_2 or NH_3 could avoid

this problem but may cause degradation in the functioning of the photoresist (poisoning). Photoresist poisoning occurs when residual bases from a cleaning step neutralize photoacids generated during the subsequent lithography step leading to incomplete development of the photoresist and hence improper transfer of the pattern to the underlying film. The liquid strippers are based on organic or semi-aqueous solvents. Batches of wafers are immersed in these solvent baths at elevated temperatures to remove the residues. However, these strippers are not environmentally benign and they require extensive rinsing in de-ionized water (DIW). Recently, researchers have reported the shortcomings of using liquids for IC processing in areas such as electroplating [12], feature wetting and residue removal [13]. For these reasons, alternative fluids such as supercritical fluids and gas expanded liquids are being pursued for several applications in the semiconductor industry.

Supercritical fluids such as supercritical CO_2 ($scCO_2$) have gained tremendous interest in recent years as alternative solvents. With properties such as moderate critical temperature and pressure, ease of availability, highly tunable properties, $scCO_2$ has found applications in areas such as specialty separations, waste treatment, and phase transfer catalysis [14]. The IC industry also took notice of the unique properties of $scCO_2$ [15] – recent studies have used $scCO_2$ for surface cleaning, aerogel processing, dielectric repair, metal deposition, and lithography. In particular, CO_2 has been used to remove organic contaminants, particles, and photoresist from Si wafers. These rely on physical mechanisms such as stress induced delamination, momentum transfer or simple dissolution to remove the contaminants. However, etch residues need a chemical mechanism for removal because of plasma induced structural changes in the photoresist

and deposition of fluorocarbon species. Due to the absence of a dipole moment, CO_2 is a weak solvent for polar or large molecular species such as photoresists. Hence addition of co-solvents or modifiers is necessary to improve its solvent strength. In this dissertation, CO_2 based mixtures have been developed for post plasma etch residue removal. These mixtures have the ability to remove residues without causing damage to the low-*k* dielectric. The underlying mechanism of etch residue removal is investigated and the effect of treatment conditions such as temperature, phase state, and composition investigated. The effect of these high pressure mixtures on the pore size and integrity of a porous low-*k* dielectric is also studied.

CHAPTER 2

BACKGROUND AND LITERATURE REVIEW

2.1 Dual damascene processing

Metal interconnects play a critical role in the functioning of semiconductor devices. They are used to transfer signals (electrons) from one device to another and to supply energy (power) to switch individual devices on/off. As device sizes grew smaller and packing became closer, overall chip size limitations precluded single layer interconnection of the numerous individual devices. As a result, interconnects have been fabricated by stacking layers in a 3-dimensional grid separated by intermetal (IMD) or interlevel dielectrics (ILD) as shown in Figure 2.1 [16]; current devices contain up to 9 or 10 metal levels. Because the smallest features are at the device (transistor) level, interconnects have the smallest dimensions at the lower levels – the size and also the distance traveled by the wires increases at higher levels. Until recently, aluminum has been the metal of choice for these interconnects because of its relatively high conductivity, ease of processing, high chemical stability, and its ability to be patterned by plasma etching. Tungsten plugs have been used to connect wires (conductor films) from one interconnection level to another. However, as device scaling progressed, aluminum could no longer be used due to material limitations. For instance, the conductivity of aluminum was insufficient at the global interconnect level where large currents must be carried to increasing numbers of devices. At the local interconnect level, increasing current densities cause the aluminum to experience increased electromigration with each

device generation [17]. Electromigration is the movement of metal atoms (leading to void and hillock formation) by high current densities. Ultimately, this phenomenon leads to reliability and interconnect failures. Also, with the addition of multiple levels of metal interconnects, aluminum cannot withstand the higher temperatures needed for deposition and annealing of the interlevel dielectric films because of its low melting temperature.

Among alternative metals to aluminum, copper was most favorable because of its low resistivity (1.7 μΩ cm) and high electromigration resistance. However, copper has a significant drawback with respect to its patterning ability. Copper halides are non-volatile – hence, it is difficult to pattern copper by plasma etching [18]. Several

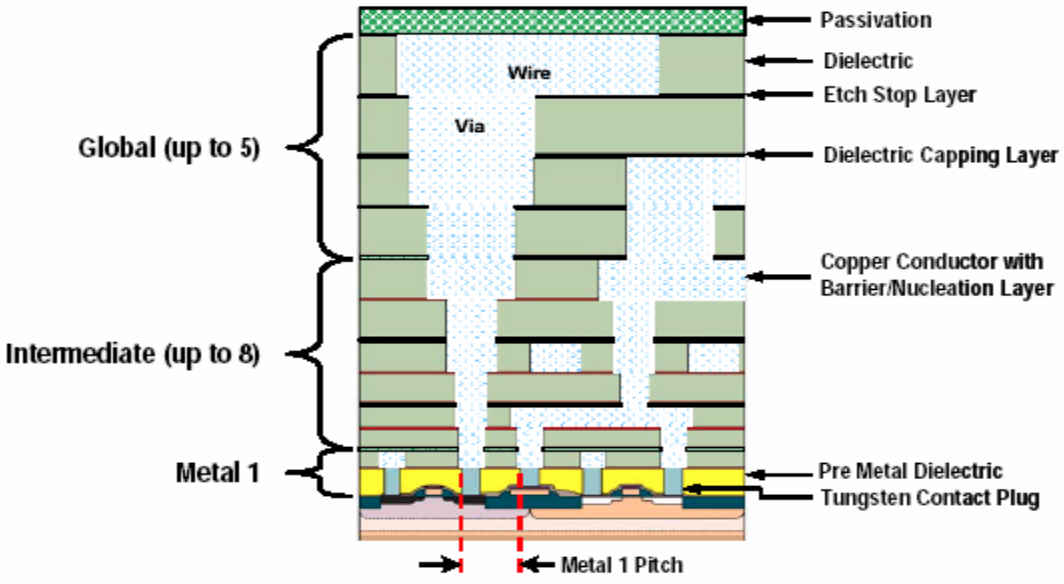

Figure 2.1. Illustration of the multi-layered interconnect structure in an integrated circuit (IC) device [16].

approaches have been investigated to improve the volatility of copper halides, such as wafer heating [19] and exposure to ultraviolet (UV) radiation [20]; however, none of these methods led to a controllable manufacturing process. Thus, an alternative method known as 'damascene processing' is used instead to pattern copper [18]. In this method, the dielectric is first patterned, thereby forming holes or vias to the underlying conductor layer; copper is then deposited into the vias to form an interconnect between conductor (metal) layers. In the 'dual damascene' method, both the via and the metal line are patterned at the same time to reduce the number of processing steps. Copper deposition is performed by electroplating, which effectively fills the vias after they are defined in the dielectric. Excess copper is then removed by chemical mechanical polishing (CMP) [18]. Intermediate layers such as etch stop layers and hard mask layers are used to assist in obtaining precise end or stop points (during plasma etching) and planar surfaces.

There are three main variants in dual damascene processing depending on how the via and the interconnect line are defined: via-first, trench-first, and buried-via approach [21]. In the via-first approach, the via is etched first in a dual stack dielectric film followed by trench lithography and etching. The main challenge with this approach is 'fencing' caused by incomplete removal of the sidewall polymer residue after via etching. In the trench first approach, the trench is etched first followed by lithography and etching of the via. This is less favorable because of the difficulty in applying photoresist uniformly at the bottom of the trench to obtain well defined vias. In the third approach, an intermediate hard-mask is first patterned before depositing the trench dielectric. After trench lithography, both the trench and the via are etched in a single step, with the hard

mask serving as a mask for the via. Any misalignment of the trench mask with the hidden hard-mask can cause defective interconnects and reliability problems.

Shown in Figure 2.2 are the various steps involved in the via-first approach to dual damascene processing. After depositing the dielectric film, a lithography step is used to define the via. After etching the via to expose the bottom etch stop layer, the photoresist and etch residues are removed. Care is taken to avoid exposure of the underlying copper to the etching process, thereby preventing copper oxidation or corrosion. The via is then filled with an anti-reflective coating to minimize reflection of the UV light from the edges. Next, another lithography step is performed to define the trench. This is followed by another etch step to pattern the trench. An intermediate etch stop layer may be used to define where the trench etch ends. Another etch residue removal step follows. A 'soft landing', or slow, carefully controlled etch process is used to open the etch stop layer thus exposing the copper. A cleaning step is used to remove any copper oxide or residues that form at the bottom of the feature. A copper diffusion barrier is then conformally deposited to prevent copper diffusion into the dielectric during heat treatments and to prevent copper corrosion upon interaction with the dielectric film. A copper seed layer is deposited by physical vapor deposition (PVD) followed by copper electroplating. These steps are repeated for every metal layer. Hence there are at least 30 cleaning steps during dual damascene patterning for a structure with 10 metal layers.

In order to reduce the interconnect delay in IC devices, the resistance-capacitance product of the interconnect structure has to be reduced. This is accomplished by replacing SiO_2 with low dielectric constant (low-*k*) materials [22] in addition to replacing

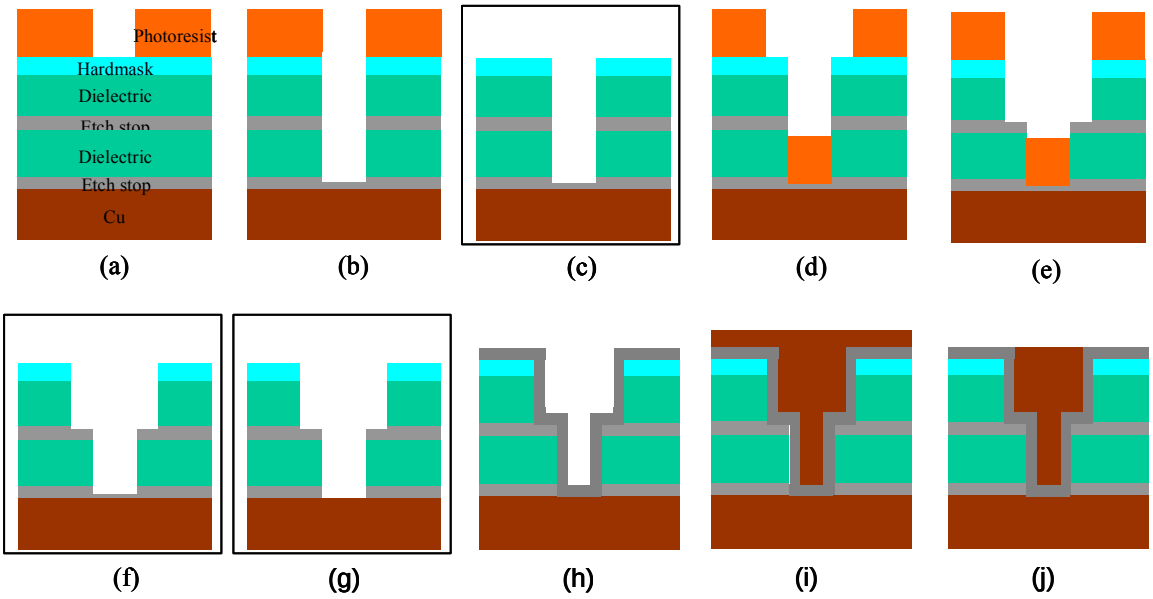

Figure 2.2. Via first dual damascene processing sequence [21]: a) film stack deposition, via lithography b) via etch c) etch residue removal d) trench lithography e) trench etch f) etch residue removal g) etch stop barrier breakthrough, metal contact clean h) copper diffusion barrier, copper seed layer deposition i) copper electroplating j) chemical mechanical polishing. The cleaning steps are enclosed in boxes.

aluminum with copper; the cross-talk between adjacent conductor lines also reduces when low-*k* dielectrics are used. The low-*k* materials may be organic (polyarylene ether, fluorocarbon, benzocyclobutene or BCB), inorganic (SiOF, hydrogen silsesquioxane or HSQ) or hybrid materials (plasma deposited C-doped SiO_2 or Si:C:O:H, methyl silsesquioxane or MSSQ). The chemical structures of some of the low-*k* materials being pursued in the industry and the academia are shown in Figure 2.3 [23].

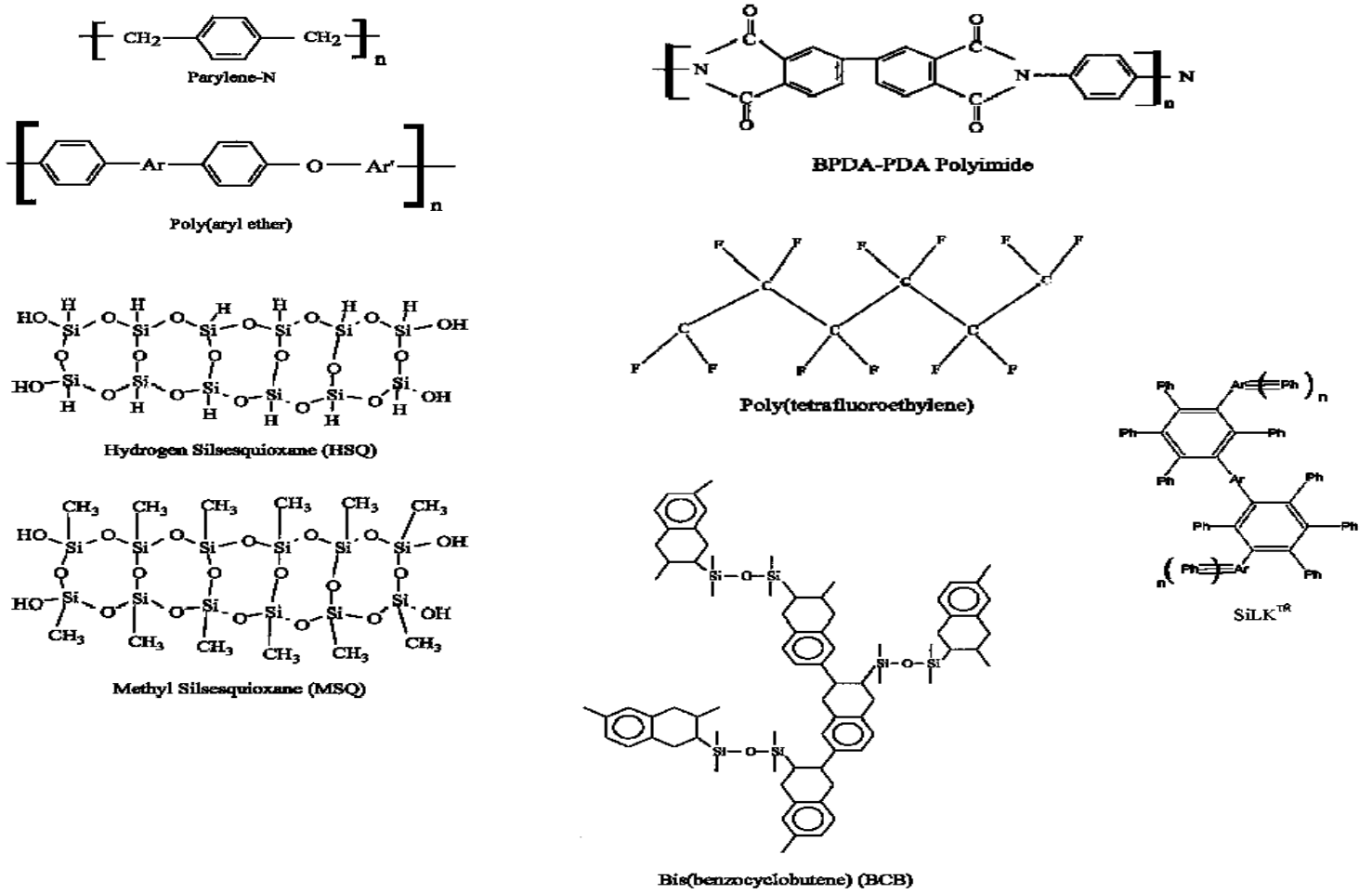

Figure 2.3. Chemical structures of some of the low dielectric permittivity materials pursued as intermetal and interlevel dielectrics [23].

2.2 Etch residue formation and characterization

2.2.1 Photoresist background

The current device generation uses deep UV (DUV) (248 nm) or 193 nm lithography to pattern the intermetal dielectric films [24]. The minimum feature size that can printed by lithography is proportional to the wavelength of the exposure radiation [25]. By using techniques such as optical proximity correction and phase shift masks, features as small as 65 nm can be printed using 193 nm lithography. The photoresists in these generations rely on the chemical amplification mechanism (shown in Figure 2.4) to undergo a material solubility change when exposed to radiation [26]. The photoresist solution consists of a backbone resin, a photosensitive compound (photoacid generator or PAG), and the solvent. The resin is generally an optically transparent polymer that provides the etch resistance and contains an acidic moiety such as phenol (248 nm) or acrylic acid (193 nm). These acidic groups are partially protected from dissolution with chemical groups such as tert-butyl ether, tert-butoxy carbonyl etc. The protecting groups are chosen based on their activation energies (for removal or deprotection) and sensitivity [27]. The PAG, as the name implies, generates H^+ ion on exposure to radiation. The H^+ ion deprotects the base resin in the exposed areas thus rendering it soluble in basic solutions. Each H^+ can cause multiple deprotections and hence behaves as a catalyst. The photoresist is then 'developed' in an aqueous base solution so that the photoresist remains in the unexposed regions.

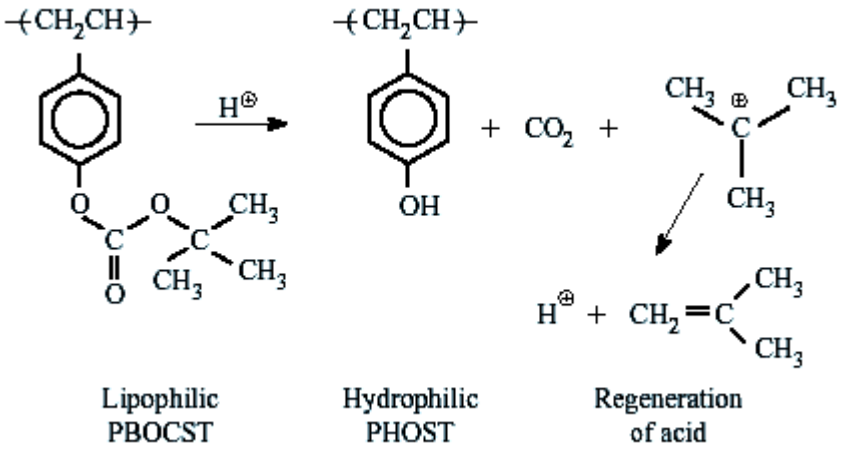

Figure 2.4. Chemical amplification mechanism in a 248 nm photoresist [26].

The greater the C to H ratio of the resin, the higher the etch resistance of the photoresist. Aromatic ring structures in the 248 nm resists provide high etch resistance.The 193 nm resists are less stable to the plasma etch environment than are 248 nm resists because of their acrylate backbone structure. The etch resistance is in fact provided by ring structures (not aromatic, because of its high absorption at that wavelength) such as adamantyl or norbornyl which are incorporated into the protecting groups [28]. Sometimes, cyclic olefins such as (norbornene carboxylic acid or t-butyl-5-norbornene-2-carboxylate) are incorporated as copolymers to acrylate groups to provide improved plasma etch resistance.

The 193 nm or even 248 nm resists are stabilized to improve their etch resistance and thermal stability. Stabilization is necessary at the local interconnect level or front end of line (FEOL) processing where high ion energies can degrade the resist or cause it

to flow leading to undesirable changes in feature sizes. Generally the wafers are heated to an elevated temperature (hard baked to 100-150 ^{o}C) to remove any residual solvent and cross-link the resin, thus improving its thermal stability and etch resistance. If especially high stability and etch resistance is required, the resist may be exposed to UV radiation in addition to heating to cause photo oxidation followed by cross-linking (photostabilization) [29]. This process, known as DUV-Bake (illustrated in Figure 2.5), is performed in an O_2 atmosphere to encourage photo oxidation. During this process, deprotection of the resin also occurs, leading to a significant shrinkage in the film

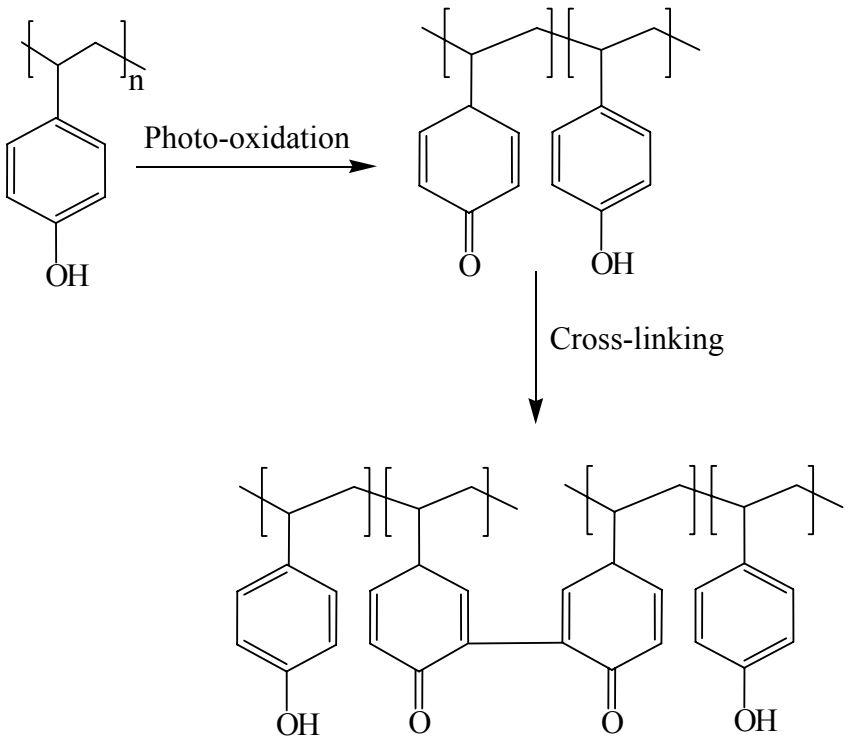

Figure 2.5. Mechanism of photoresist hardening by DUV-Bake prior to plasma etching [30].

thickness. It has been observed that the solubility of poly 4-hydroxystyrene (PHOST) based films in organic solvents decreases after DUV-Bake [31]. This observation may have ramifications on the post etch removal of photoresist residues. When the photoresist is heavily cross-linked during the plasma etching or the pre-etch DUV-Bake step, it cannot be removed by organic solvents through dissolution mechanisms alone. Indeed, similar changes in photoresists exposed to etch plasmas without prior photostabilization have been observed.

2.2.2 Dielectric etch mechanism

Plasma deposited SiO_2 has been used for more than two decades as the ILD due to its high thermal, mechanical, and chemical stability, low moisture absorption, planarizing ability and its well characterized etching and deposition properties. Fluorocarbon gas plasmas (CF_4, C_2F_6, CHF_3, C_4F_8) are used to etch SiO_2 [9]. Fluorine atoms, generated by electron impact collisions in the gas phase plasma, react with SiO_2 to form volatile etch products such as SiF_4, CO_2 and H_2O [9]. Extensive research has been done to understand the mechanism of etching SiO_2 and the surface reactions that occur in these fluorocarbon plasmas [32-35]. The role of carbon in these etch gases is to provide etch residues to ensure vertical feature profiles (anisotropy) and etch selectivity to underlying films [36]. After the etch gas dissociates into radicals, ions, and neutrals in plasma, some of the carbon containing species form oligomers or polymers and deposit on the surface. Polymerization is greatly reduced on SiO_2 because oxygen from the film removes C in the form of CO and CO_2. The electrode on which the substrate is positioned is also biased to impart enhanced energy to the impinging ions. These high energy ions promote

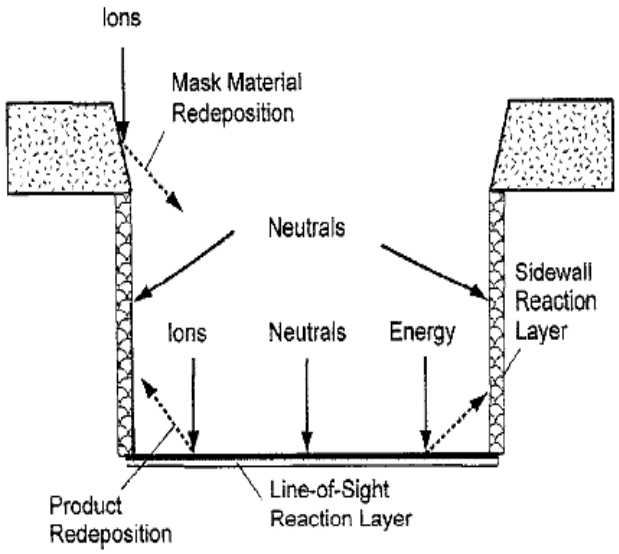

Figure 2.6. Surface processes leading to residue formation during plasma etching of a via or a line [36].

etch rates by stimulating desorption of reaction products and assisting removal of fluorocarbon layers formed on SiO_2 surfaces. A minimum ion energy is required so that dielectric etching and fluorocarbon polymerization occur simultaneously under essentially steady state conditions. Under the appropriate conditions, etchant species (primarily F radicals) can diffuse through the thin (<5 nm) fluorocarbon film and etch the underlying SiO_2. On the sidewalls, the thickness of this fluorocarbon film is larger because ions are accelerated vertically into the surface; sidewalls, therefore, receive little ion bombardment. As a result, this process generates anisotropic (vertical) etch profiles which are necessary to define small features that can be filled without leaving voids in the structure. Similar fluorocarbon plasma chemistries are used to etch low-*k* ILDs which are typically composed of SiO_2 that has been modified by the introduction of carbon

moieties [37]. The surface processes that occur during plasma patterning of a dielectric are illustrated in Figure 2.6.

Inorganic or hybrid low-*k* films are etched using the baseline plasma process developed for SiO_2 etching. Modifications are made to the process to meet the etch rate and profile requirements [38]. For example, when high levels of hydrogen are present in the low-*k* material, the etch rate decreases (due to the H scavenging F radicals) and the profile may become tapered. These effects are compensated by addition of a small amount of O_2 to the etch chemistry. Similarly, a small amount of O_2 is added to obtain higher etch rates when organic groups are present in the dielectric (e.g. methyl silsesquioxane). Completely organic (including fluorocarbon) low-*k* materials are etched in an O_2 (oxidizing) or H_2 (reducing) plasma. These gases can be mixed with a diluent and an additional gas that provides sidewall passivation. A small amount of fluorine is usually added to enhance etch rates by creating surface active centers that are attacked by oxygen species [39]. Since the etch selectivity of organic films to photoresist is only 1:1, a hard mask such as SiO_2 or Si_3N_4 has been invoked to ensure process control. Vertical profiles are maintained by tailoring the amount of ion bombardment and film deposition (passivation). In some instances, the etch process is tailored so that the photoresist is etched completely at the point where the etch stop layer is reached [40]. Provided that adequate film thickness and etch uniformity is achieved, no additional photoresist removal step is required but the sidewall polymer must be removed.

In order to avoid problems with etch residue removal, alternative etch chemistries have been studied that can eliminate or reduce polymer deposition. Chemistries such as F_2, Cl_2, and HBr have been used to etch organosilicate glass (OSG) dielectric films

CORAL™ and Black Diamond™ [41]. After etching, Black Diamond™ has shown very little surface modification, implying that little if any polymer deposition has occurred. However, etch selectivity of only 1 was achieved with respect to the photoresist. However, in this report, the authors have not performed etching with a photoresist mask which will serve as a source for C resulting in halocarbon deposition. Another approach to avoid etch residue formation involved the use of plasma etching at sub-zero temperatures. In this study, the wafer was cooled to -50 ^{o}C to decrease reaction kinetics, thus reducing the isotropic etch rate by neutral radicals [42]. Only ions can cause etching by physical bombardment of surfaces, and hence highly anisotropic profiles were achieved without addition of polymerizing gases.

2.2.3 Line-of-sight residue formation

Oehrlein and others have studied the surface reactions during fluorocarbon plasma etching of Si, SiO_2 and Si_3N_4 in high density plasma (inductively coupled plasma (ICP) or electron cyclotron resonator (ECR) systems [33, 35-37, 43-45]. In these systems, two different power sources are used to independently control the plasma density and the ion energies [9]. In reactive ion etching (RIE) systems, a single capacitive power source is connected to the electrode upon which the wafer is positioned. Since power=current×voltage, an increase in coupled power may manifest in the form of increased current and/or increased bias voltage. In high density plasmas for etching SiO_2 or Si_3N_4, three regimes have been identified that describe dependence of etch rate on RF bias voltage (Figure 2.7). When the bias voltage (ion energy) is below the threshold energy, negative etch rates (‘fluorocarbon deposition’ regime) are observed. Apparently,

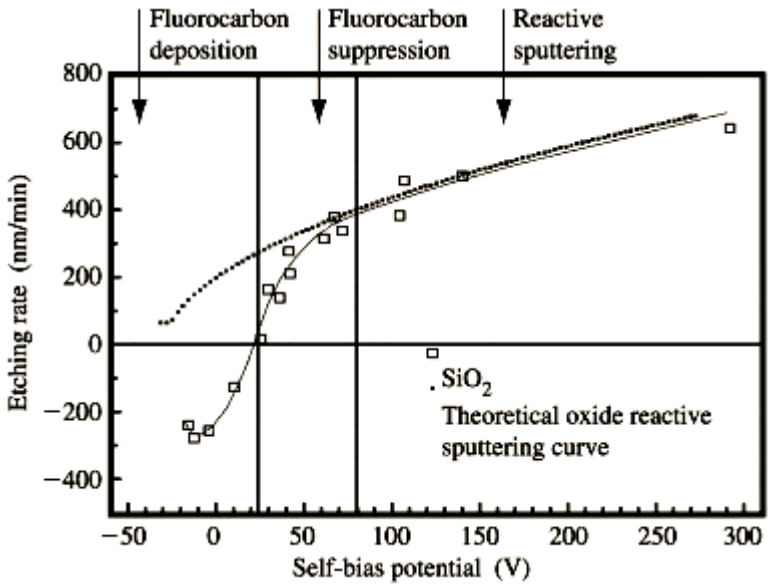

Figure 2.7. Etch rate dependence on DC bias (ion energy) for SiO_2 etching in an ICP reactor [35].

deposition occurs due to neutrals and radicals as well as low energy ions [46]. The threshold energy depends upon the etch gas and pressure and was estimated to be 10 V at 20 mTorr and 30 V at 6 mTorr for a CHF_3 ICP system [35]. At energies well above the threshold energy (>80 V), the 'reactive sputtering' regime is observed in which the energy supplied by the ions causes film ablation and thus etching. The etch rate (or yield) is proportional to the square root of ion energy [35]. In the intermediate 'fluorocarbon suppression' regime, part of the ion energy is used to thin down (ablate) the fluorocarbon film (from 0.6 nm at 30 V to 0.3 nm at 80 V) and hence the etch rates are less than those in the 'reactive suppression' regime. Most of the commercial plasma etch tools operate in the 'reactive sputtering' regime where the etch (ablation) rates are maximum and hence the thickness of the fluorocarbon film is <1 nm at the bottom of the

features. In contrast, on the underlying Si surface, the fluorocarbon film is thicker (~2.5 nm in a CF_4 ECR discharge and ~5.5 nm in CHF_3) discharge thus enabling highly selective SiO_2/Si etch. On Si_3N_4, the fluorocarbon thickness is intermediate between SiO_2 and Si and hence intermediate etch rates and selectivities to Si are observed [45]. A schematic of the fluxes incident on and outgoing from Si, SiO_2, and Si_3N_4 along with the resulting fluorocarbon film is shown in Figure 2.8 [45]. Since the residues are thin (<10 nm), x-ray photoelectron spectroscopy (XPS) is the most common technique to measure the composition, bonding structure and thickness of these residue, although ellipsometry has also been used to estimate the film thickness [33]. To estimate the thickness from XPS data, it is assumed that a uniform over layer of fluorocarbon film lies on top of the substrate [33, 45]. To perform these studies, blanket films of Si, SiO_2, Si_3N_4 or low-*k* are exposed to the etch plasmas and the resulting fluorocarbon residues are analyzed.

C_4F_8 has replaced CF_4 or CHF_3 as an etchant for Si containing dielectrics [47]. Due to the cyclic structure and smaller F:C ratio, C_4F_8 provides greater anisotropy than does CF_4 or CHF_3. The use of such strongly polymerizing chemistry also reduces surface roughness and sidewall striations in 193 nm resists [48]. The extent of dissociation of C_4F_8 in an etch plasma can be controlled by electron density, electron temperature, and gas residence time [47]. A small amount of O_2 or N_2 is added to C_4F_8 to remove excess C on the etched surface [49] and provide selective dielectric etch with respect to Si, SiC or Si_3N_4,where Si_3N_4 and SiC are used as etch stop layers for dielectric etching in damascene processing. Small amounts of H_2 have also been added to provide highly selective SiO_2/Si etching because H can abstract F from CF_x species in the gas phase [50]. Ar is often used as a carrier or diluent gas because it has multiple metastable states

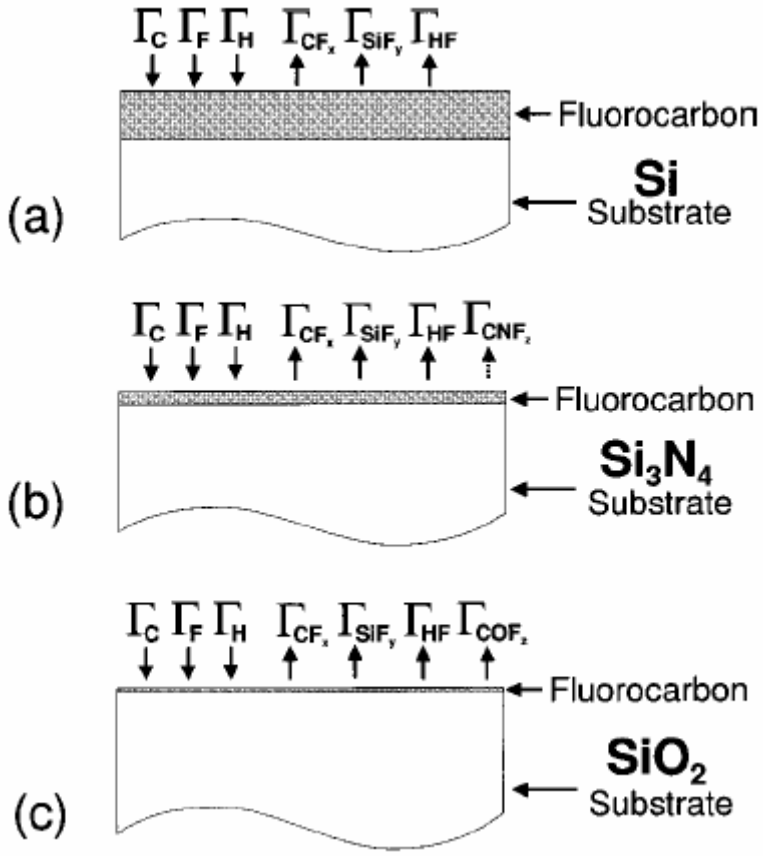

Figure 2.8. Schematic of fluxes of species that are incident on and outgoing from (a) Si, (b) Si_3N_4, and (c) SiO_2 during plasma etching. Also shown are the relative thicknesses of fluorocarbon films deposited during the etching process [45].

that can enhance the plasma-assisted dissociation of etch gases, although, Radke and others have recently shown that dissociation of C_4F_8 is almost exclusively caused by electrons and the contribution by Ar metastables is negligible [47]. Tatsumi and others have studied the surface reactions in dual frequency $C_4F_8/Ar/O_2(N_2)$ plasmas while etching Si:C:O:H dielectric films [49]. These studies reported that the C_4F_8 gas flow rate governs the rate of polymerization and hence the thickness of CF_x on the surface which in

turn governs the Si:C:O:H etch rate. The thickness of the fluorocarbon layer varied from <1 nm to ~4 nm depending on the C_4F_8 flow rate. Since the flux of CF_x inside vias is likely different from that reaching the surface of unpatterned films, the etch characteristics in patterned regions may be different from those on blanket films. Hence the flow rates must be optimized to provide desired etch rates, via profiles and selectivity.

Dual frequency plasmas were also used to study the mechanism of highly selective contact hole (via) etching using $C_4F_8/Ar/O_2$ chemistry [32]. In this study, two different frequencies were used to power the plasma and the substrate in order to independently control the plasma density and ion energies, respectively. The thickness of the fluorocarbon film on Si, Si_3N_4 and SiO_2 was estimated from XPS peak intensities. The Si2p peaks from the dielectric (via sidewalls) and the Si substrate (via bottom) were separated by differential charging techniques. According to this study, there is a small process window to achieve selective etching of SiO_2 over Si in narrow features (aspect ratios over 4) because the SiO_2 etch stop occurs with excessive deposition of fluorocarbon polymer. This is due to a decrease in ion bombardment at the bottom of the high aspect ratio features.

2.2.4 Sidewall residue formation

While ions are primarily responsible for via bottom residues (or 'line-of-sight' residues), the neutrals and scattered ions are responsible for sidewall polymer formation. In addition, some of the material being etched is sputtered onto the sidewalls by high energy ions. Because less ion bombardment occurs on the sidewalls, the fluorocarbon

film is expected to be less cross-linked than the line of sight polymer. Therefore, sidewall polymer contains -CF_2- rich bonding structures as opposed to C-CF_x groups at the via bottom. Since the process is neutral species driven, an increase in plasma pressure enhances the sidewall polymer formation due to higher concentration of neutrals and also increased ion scattering [51]. Thus, the use of high density plasmas which operate at lower pressures compared to RIE plasmas, was expected to alleviate this deposition, at least to some extent.

Compositional or topological analysis of sidewall polymer is quite difficult because of small feature dimensions and high aspect ratios. Unlike sidewall polymer, one can simulate via bottom residues by exposing a blanket dielectric film to the etch plasma. It is possible to deposit residues similar to sidewall polymer by placing a wafer parallel to the electric field (perpendicular to the electrode) in a fluorocarbon etch plasma. However, issues such as temperature control, non uniformity of the electric field (sample dimensions much larger than the via) and absence of micro loading effects may result in residues which are not exact replicas. The most common approach to characterizing sidewall polymers is by imaging techniques such as cross sectional scanning electron microscopy (SEM) (Figure 2.9) or transmission electron spectroscopy (TEM). SEM or TEM micrographs are taken before and after a clean step to ascertain if the sidewall polymer is removed [52]. These may be combined with energy dispersive spectroscopy (EDS) [51, 53] or electron energy loss spectroscopy (EELS) [54] to analyze the composition of the sidewall and via bottom residues. Some times, the etch chemistry is intentionally tailored to deposit excessive sidewall residue to better judge the cleanliness from SEM micrographs [55]. Secondary ion mass spectroscopy (SIMS), which is a

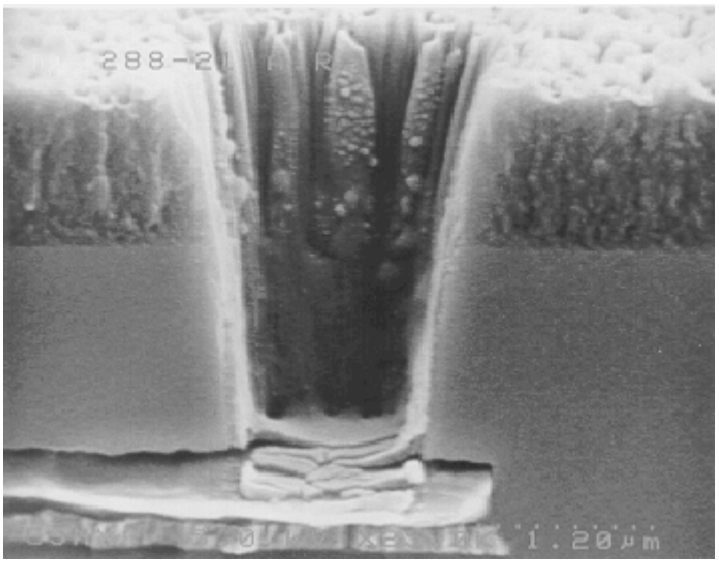

Figure 2.9. Cross-sectional SEM image of a plasma etched via with sidewall polymer [52].

destructive technique, has also been used to analyze sidewall polymer composition from different chemistries and in vias of different sizes and aspect ratios [56]. In this case, arrays of vias were sputtered from the top of the via down into the via while analyzing the evolution of ionization products with depth of the via. Auger electron spectroscopy (AES) was also used to study the atomic composition of the residues on the sidewalls by scanning along the length of a via [57]. The advantage of such electron or ion beam based techniques is their ability to probe very small areas (<100 nm spot size). Finally, an indirect way to detect the presence of sidewall polymer is by electrical measurements – test structures have been built to measure the sidewall conductivity of vias. Sidewall polymer deposited from gases such as ($F_2C=CF_2$) has conjugated linkages and, hence, higher electrical conductivity than polymers formed from C_4F_8 gas [58].

2.2.5 Photoresist residue formation

When photoresist is used as a mask for dielectric etching in a fluorocarbon plasma, it is bombarded by ions, electrons and the neutral species from the plasma and is thus modified. The surface of the photoresist becomes cross-linked [59] and fluorine is incorporated into the resist. Shown in Figure 2.10 is the cross-sectional SEM image of a line structure with approximately top one-third of the photoresist cross-linked due to plasma etching [60]. During the etching process, a thin fluorocarbon layer is deposited on the photoresist analogous to the process described above for SiO_2 etching. Photoresist has more carbon than a SiO_2 based dielectric and more oxygen than Si – hence, the thickness of the fluorocarbon layer is intermediate between that formed on SiO_2 and Si. The photoresist also acts as a source for carbonaceous species in the plasma which contribute to fluorocarbon residues deposition on other areas of the wafer. The fluorocarbon layer thickness was estimated to be ~1 nm on a novolak resist exposed to a CHF_3 plasma [43]. XPS is again used to measure the surface atomic composition and to estimate the thickness of this fluorocarbon film. The thickness of the fluorocarbon film and its fluorine content decreased with increasing ion bombardment, consistent with observations on the via bottom residues. It was also observed that the etch rate of the photoresist film was inversely proportional to the thickness and the extent of cross-linking of this fluorocarbon layer.

Entrapment of volatile fragments by the deposited amorphous fluorocarbon polymer during etching leads to surface morphology distortions [61]. These fragments may be protecting groups released by sample heating or radiation during etching, or,

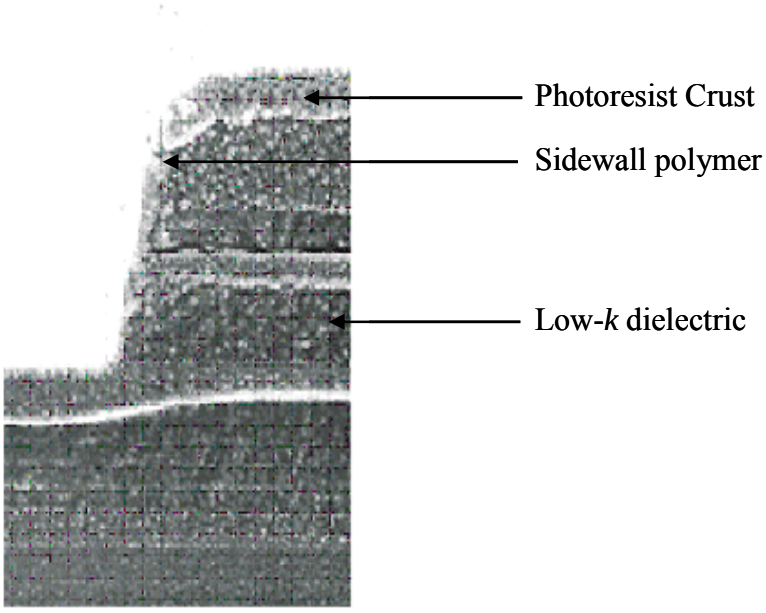

Figure 2.10. Cross-sectional SEM image showing post plasma etch photoresist residue [60].

volatile chain scission products from the resin itself (e.g. CO_2 and isobutene evolve from PHOST-t-butyl acrylate based 248 nm resists as a result of electron bombardment). This deprotection can occur due to UV radiation in the plasma, ion bombardment, substrate heating or generation of acidic moieties in the plasma. Transmission FTIR measurements were performed on a 248 nm resist exposed to C_4F_8 and C_5F_8 based SiO_2 etch plasmas in an ICP system [62]. Under wafer bias conditions, the photoresist resin (partially protected PHOST) underwent deprotection as a result of ion bombardment. The aromatic part of the resist did not show any sign of damage or etching. Surface analysis by XPS also showed that C_5F_8 resulted in fluorine rich films containing more CF_x bonds. In contrast, C_4F_8 resulted in C-C/C-H rich films indicating less polymerizing ability than

C_5F_8. In fact, the shape of carbon XPS peak from C_4F_8 was very similar to the peak from samples used in the studies reported in this thesis.

The nature of the plasma also plays an important role in the photoresist deprotection process [27]. Acidic plasmas such as Cl_2/O_2 which is used to etch chromium masks cause more deprotection than basic NH_3 plasmas. Acidic species such as HCl which are generated in these plasmas can cause deprotection even in the absence of a PAG. Fluorocarbon plasmas can be considered slightly acidic because of the presence of HF species. The extent of deprotection also depends on the activation energy barrier of the leaving groups. For example, acetal groups (Ea<25 kcal/mol) are more labile than t-butyl acrylate (Ea>30 kcal/mol) because of their low activation energy [27]. Inadvertent heating of the resist caused by exposure to the plasma can also cause deprotection [28]. For example, the surface temperature of 193 nm resists while etching 130 nm vias in SiO_2 was found to be 60 ^oC higher than the electrode temperature. When the activation energy of the protecting group is exceeded, the protecting groups are released, causing bubble formation, and flow of the resist due to lowering of Tg. The etch resistance of the resist also drops when the released protecting groups have ring structures such as norbornyl or adamantyl which are intended to provide etch stability to the resin.

Similar changes have been observed in organic low-*k* films exposed to O_2/NF_3 afterglow (downstream) plasma when studying their modification in etch plasmas [39]. Due to fluorination of the films, the refractive index of the films decreased significantly. The films also became resistant to a 4:1 mixture of H_2SO_4 and H_2O_2 mixture at 90 ^oC, unlike the original films which were easily removed. The thickness of the fluorinated

layer was estimated to be ~300 nm after 5 s exposure to an NF_3 downstream plasma. A relatively thick film was deposited because of the absence of ion bombardment and the diluent gas.

2.3 Etch residue removal

The residue at the bottom of the via adds to the contact resistance of the interconnect which becomes significant due to the very large number of interconnects in state-of-the-art IC devices. One of the consequences of using a polymerizing chemistry for via/trench etching is formation of excessive sidewall polymer that has to be removed during the subsequent cleaning step. In addition to decreasing the conductive cross section, the sidewall polymer could also contribute to corrosion of the metal vias or lines. That is, if not removed completely, the fluorocarbon residues could hydrolyze and form HF that can attack the dielectric and the metal lines. During via-first dual damascene processes, incomplete removal of the sidewall polymer after via etch can lead to fence formation during trench etch [63]. Removal of this sidewall polymer is also essential for good adhesion of barrier layers to the dielectric film [64]. Traditionally, these residues are first 'ashed' in an oxidizing plasma and any post-ash residues are removed using a liquid solvent.

2.3.1 Residue removal by plasma ashing and other dry methods

In the IC industry today, the etch residues are removed by 'ashing' in an oxygen plasma, which converts them to volatile products such as CO, CO_2, COF_2, H_2O, HF, CF_4,

etc. [11]. Plasma ashing causes less process induced contamination, is compatible with cluster tooling, and has high removal rates. Ashing is performed in a microwave (MW) or radiofrequency (RF) downstream plasma, which eliminates direct exposure of the wafer to radiation and electrons or ions which can cause damage to dielectric materials. In some instances, the presence of ions has the beneficial effect of densifying the surface of the dielectric, thus rendering it impermeable to moisture or other contaminants [65]. The wafer is placed on a heated electrode that is isolated from the discharge region by a tube with a 90 degree bend. Addition of small amounts of a fluorine containing gas (e.g. CF_4) enhances the ashing rates due to the ability of F to abstract H from the polymer; addition of fluorine also increases O_2 dissociation in these plasmas, which increases etch rates due to the increased concentration of O [11]. Fluorine-containing plasmas have also proven to be effective in removing sidewall polymer by slightly etching the interface between the polymer and the dielectric. An O_2 plasma is very effective in organic residue removal because it attacks the fluorocarbon film at unsaturated bonds and forms volatile products. Indeed, the etch residues contain unsaturated bonds as shown by their relatively high electrical conductivity [58]. A very short (<5 sec) O_2 plasma flash may also be used to remove fluorocarbon residue that is deposited on top of the hard mask after etching an organic low-*k* film (BCB) [64]. Even a 1 second O_2 ash or Ar^+ beam exposure has been shown to remove this residue. However, damage to the dielectric and incomplete removal of sidewall polymer are concerns with this approach when applied to organic or hybrid low-*k* films.

Ashing in O_2 plasmas is ineffective when non-volatile metal or other inorganic (e.g. Si) species are present in the etch residue. For instance, with copper metallization,

unacceptable oxidation of the metal can occur in the ashing plasmas which increases the contact resistance in the vias. In addition, metal can be sputtered onto sidewalls during the etch stop breakthrough step [51] and the over-etch step. Usually, a certain amount of over-etch time is employed to account for non uniformities in etch rates and in film thickness across the wafer. This may result in the formation of organometallic ($MC_xF_yO_z$) compounds on the sidewall and bottom of the vias. If these materials have low vapor pressures, the organometallics remain on the surface after oxygen ashing. An additional liquid-based cleaning step is used to remove these residues completely. Plasma processes are also capital intensive, can cause radiation damage and result in resist 'popping' [66] due to film heating.

Most importantly, oxygen based plasmas are problematic when the dielectric material consists of organic materials or carbon additions to inorganic dielectrics. In these cases, the dielectric material is modified due to oxidation, thereby increasing the dielectric permittivity of the film [41, 67, 68]. Furthermore, the film becomes hydrophilic and moisture absorption is then an issue in the subsequent processing; post ash treatments must be implemented to restore the hydrophobicity [69]. Even directional ashing of the resist in an oxidizing plasma with a hard mask over the low-*k* material can modify the low-*k* material along the sidewalls. The modified (oxidized) thickness was estimated to be as large as 0.2 μm [54], which is unacceptable when the feature sizes themselves are <0.2 μm. Hence, reducing chemistries such as H_2 [55], H_2/N_2 [70] or NH_3 plasmas [65] have been suggested. These chemistries remove the residues in the form of HCN, HF, CF_xH_y and leave the surface hydrophobic (H_2). However, these plasmas do not remove the residue completely [71] and require an additional liquid step. For

example, ~1 nm of defluorinated carbonaceous residue was left behind on the sidewalls even after H_2 plasma ashing of post etch SiO_2 residue [55]. In addition, reducing plasmas have been shown to generate residual amine moieties in the dielectric which can cause photoresist poisoning [54]. With chemically amplified resists, even small amounts of these basic species can shift the UV dose required to effectively expose the resist to a much higher value. Novel but energy intensive methods such as laser cleaning have also been studied for efficient removal of via-etch-induced polymers [72]. However, a separate ashing step was used to remove the photoresist before an excimer laser was used to break down the remaining residue into small fragments.

2.3.2 Post ash cleaning

Because of the inability of plasma ashing to remove residues completely, post ash residue removal is performed with a liquid solvent. After the ashing removes the top CF_x residues and exposes the resilient SiO_xF_y or $MC_xF_yO_z$ residues underneath, dilute HF [73] is used to remove the remaining residues, leaving behind a fresh Si or SiO_2 surface. A mixture of sulfuric acid, hydrogen peroxide with small amount of HF (ppm level) was also used to remove the post ash residues from metal structures [74]. The HF treatment is effective because it attacks Si-O bonds while the sulfuric acid removes metal oxides in these residues. However, excellent process control is necessary to prevent excessive etching or interfacial delamination of SiO_2 [51]. In the case of copper, even dilute HF (at room temperature) was incapable of removing Cu_2O or CF_x residues at the bottom of the via [73]. Hydroxylamine (NH_2-OH) based commercial strippers (e.g. EKC 265™) are effective in removing organometallic residues containing aluminum [51]. EKC 265™ is

basic and, hence, can dissolve residues that are Lewis acids. Solution agitation was also necessary for two reasons: to enhance the diffusion of the solvent to the vias and to physically remove the tough residues after they were loosened by the solvent.

2.3.3 Residue removal by liquids

Post etch cleaning using liquids has been very attractive because of low cost, fast stripping rates under mild conditions, and ease of disposal as opposed to hazardous gases used in ashers or etchers. Batches of wafers are immersed in solvent baths at elevated temperatures to accelerate the chemical attack. Spray tools have gained wide interest due to their greater uniformity with increasing wafer sizes, and because they impart mechanical force to assist remove of particles and residues. Wafer drying is also performed in the same spray tool to prevent cross contamination from wafer handling. With aluminum metallization, commercial formulations based on hydroxylamine-based solvents have been employed to remove the metal etch residue. In the case of copper metallization, fluoride-based chemistries (semi-aqueous chemistries or SAC™) are employed since hydroxylamine-based solvents are not compatible with Cu [75] and some low-*k* materials such as HSQ [76]. These SAC™ chemistries (pH between 8 and 10) consist of water, an organic solvent and a small amount of buffered fluoride salt which is the chemically active species. These chemistries display differences in their residue removal mechanism [77] - hydroxylamine-based chemistries dissolve the residue from the surface, whereas, SAC™ chemistries act by diffusion of the active species through the residue, breaking it into smaller fragments. A subsequent de-ionized water (DIW) rinse removes the fragmented residue. However, the commercial fluoride-based

chemistries resulted in unacceptable levels of critical dimension (CD) loss in vias etched in SiO_2 or organic low-*k* material (SiLK™) even at very low concentrations [75].

Microwave downstream plasmas have been used in conjunction with densified fluid cleaning (DFC) to remove post via etch and post metal etch residue [52]. In densified fluid cleaning, the wafer (maintained at 20 ^{o}C) is exposed to dense hot ammonia vapor at 20-25 atm. Megasonic energy is applied to transfer mechanical energy to the wafer through the densified fluid layer formed on the wafer. However, this process is extremely sensitive to any moisture in the ammonia that can cause corrosion of metal lines. Alternatively, DIW/O_3 mixtures have received considerable attention [78] for photoresist removal due to their high removal rates; unfortunately, they are not compatible with organic low-*k* materials. For better mass transfer characteristics, some researchers have used ozone vapor with additives such as H_2O_2 or acetic acid [79]. The vapors containing the additives and ozone condense on the wafer and form a thin film with higher concentration of the chemically reactive species, but with low resistance to mass transfer. Other chemistries studied include sulfuric acid/hydrogen peroxide mixtures (SPM) and ammonium hydroxide/hydrogen peroxide mixtures (APM). These mixtures primarily oxidize the organic contaminants and break the residue into smaller fragments. A subsequent DIW rinse is used to remove the resulting fragments and any chemicals adsorbed on the surface. In addition to being incompatible with organic moieties in the dielectric materials, these wet processing steps also use large amounts of DIW and are toxic (SPM). Sometimes, an intermediate rinse is required to prevent metal corrosion due to 'pH shock' [80]. The rinse solvent may be IPA (to displace the cleaning solvent due to its low surface tension), a buffered chelating agent (to remove fluorides or

other active species) or CO_2 sparged water [77] (to neutralize any residual amines). An additional drying step (IPA vapor drying) is required after the DIW rinse step. Naturally, all of these additional steps add to process cost and the waste generated.

On average, a wet bench for cleaning and surface preparation uses 53 liters of ultra-pure water (UPW) per 300 mm wafer per cleaning cycle. The ITRS roadmap has recommended a reduction in net UPW usage from the present 5.9 liters/cm^2 wafer area to 3.5 liters/cm^2 by 2010 [81]. At 5.9 liters/cm^2, a fabrication facility producing 40,000 wafers/month uses 44 million gallons of UPW per month. This puts a great strain on the local water resources and contributes significantly to the manufacturing costs. Since residue removal and surface preparation account for a significant portion of the DIW consumption, an alternative cleaning process that uses no/less water is necessary.

The dielectric constant of SiO_2 is reduced by incorporating organic or fluorine containing groups. However, for sub-100 nm device generations, porous low-*k* materials will be employed to achieve a dielectric constant <2.3. These materials pose additional challenges to residue removal. It has been shown that fluorocarbon deposition takes place inside the nanometer scale pores during etching of porous xerogels [37]. Liquids may have difficulty entering these small pores to remove the residue. DI water used during subsequent rinsing steps might diffuse into the small pores and cause corrosion of metal lines if not removed completely. It is also suspected that liquids might not be effective in entering small and high aspect ratio features due to transport limitations [82]. Hence, an ideal alternative to the present methods would be a vapor phase single step etch residue removal method with cluster-tool compatibility.

2.4 CO_2 based fluids for etch residue removal

In a recent modeling study on the limitations of liquids for cleaning inside small vias, it was identified that the time for a liquid to wet a via depends on the contact angle of the liquid on the sidewall polymer [83]. Hence, for an aqueous solvent on fluorocarbon residues (high contact angle), the wetting time can become significant compared to the cleaning time needed to remove the residue. However, under similar conditions of gas-liquid interfacial tension and contact angle of the liquid on via sidewall, the estimated wetting time decreased as the aspect ratios of the features increased. Experimental and model based investigations also indicated that high surface tension liquids (e.g. water) can cause collapse of photoresist patterns due to capillary forces [84]. This can occur while the photoresist is being rinsed and dried after developing in an aqueous base solution. As the feature sizes decrease and the aspect ratio of the pattern in the photoresist increases, this problem is exacerbated. Hence, drying with a low surface tension fluid such as supercritical CO_2 ($scCO_2$) should be able to displace water without causing this collapse [85, 86]. Compared to liquids, supercritical or near critical CO_2 has very low surface tension and high diffusivity; thus, it can wet the residues faster without causing pattern collapse in the dielectric or photoresist. These fluids can also enter the pores in a low-*k* film (sub 10 nm) and likely remove residues incorporated in them. CO_2 also enables drying in the same chamber after processing – hence cluster tooling is possible which is necessary to reduce the costs and the tool footprint in a fabrication facility. Since CO_2 is obtained by separation from flue gases or natural sources, it is relatively cheap and is not an environmental hazard. Its moderate critical temperature (31 ^{o}C) and critical pressure (73.8 bar) [87] also make it favorable from safety and energy

considerations. Another significant advantage of these fluids is the ability to tune their solvent properties as a function of pressure. The Hildebrand solubility parameter (δ), which is an indicator of solvent strength, changes from 3.1 $(cal/cm^3)^{1/2}$ to 7.4 $(cal/cm^3)^{1/2}$ as the density of CO_2 changes from 0.4 g/cm^3 to 1.0 g/cm^3 at 50 ^oC [88]. Hence, solutes can be easily separated from CO_2 by reducing the pressure and causing precipitation since the solvent power has been diminished.

2.4.1 CO_2 applications in the IC industry

Due to its superior transport and solvent properties, carbon dioxide has found several potential applications in semiconductor manufacturing. CO_2 has been used to clean precision parts, thereby replacing the ozone depleting chlorofluorocarbons [89] as well as gas/solid jet sprays [90]. These high pressure processes are effective in at least partially removing contaminant molecules such as silicone oils, fluoroethers and hydrocarbons. Recently, Ober et al. have developed diblock copolymer resists for 193 nm lithography using $scCO_2$ as the developing solvent [91]. These negative tone photoresists consist of a $scCO_2$ insoluble chain linked to a fluorous or siloxane type chain, making it slightly soluble in CO_2. Upon exposure to radiation, the copolymer undergoes fragmentation, making the resist insoluble in CO_2. Liquid CO_2 has also been used as a solvent for spin coating resists for lithography [92] and as a developer for a fluorocarbon resist after e-beam patterning [93]. The resist undergoes fragmentation after e-beam exposure and becomes more soluble in CO_2. Several groups also have investigated the production of porous materials using $scCO_2$ as a solvent and/or foaming agent [94-96]. Due to its low surface tension, $scCO_2$ was used to dry photoresist in order

to prevent pattern collapse [85, 86]. Another interesting application of $scCO_2$ is in metal deposition – metal films of Pt, Pd, Au, Rh, Ni and Cu were deposited by reducing their precursors in CO_2 [97, 98]. This process, known as 'chemical fluid deposition' (CFD), is a low temperature alternative to chemical vapor deposition (CVD) and has demonstrated highly conformal coverage in high aspect ratio features due to the excellent transport properties of CO_2.

2.4.2 CO_2 for cleaning applications

Bok et al. first reported a wafer cleaning process using $scCO_2$ in 1992 [99]. Pressure pulsation was used to dislodge particles and remove organic contaminants from small features. Due to its linear structure, CO_2 has zero dipole moment but has a small quadrupole moment. It is therefore a weak solvent for polar, ionic or large molecular weight species due to very weak van der Waals interactions [100]. Hence, addition of co-solvents or modifiers is necessary to enhance the solvent strength of CO_2. Only molecules with low solubility parameter and low polarizability such as fluoroalkyl or siloxane molecules are considered 'CO_2-philic' [101]. CO_2 also has Lewis acid - base type interactions with polymers such as poly(methylmethacrylate) (PMMA) and poly(styrene) (PS) with CO_2 acting as a Lewis acid [102]; CO_2 swells these polymer films and increases the free volume between the chains. Thickness measurements have revealed more than 27 vol% swelling in free standing PMMA films [103] and up to 20 vol% in thin films of PMMA on Si wafers [104]. CO_2 has been used to remove photoresist and residue after ion implantation and etch step [105, 106]. In these studies, propylene carbonate was used as a co-solvent to improve the solvent properties of the

fluid. Pressure pulsing was also used to crack and peel the film (PMMA based negative resist) from the substrate. Solvents such as γ-butyrolactone and dimethyl sulfoxide (DMSO) were also used as co-solvents to remove photoresists [107]. For post etch residues, two phase mixtures of these solvents and CO_2 were shown to be more effective. The condensed liquid solvent was thought to provide dissolution of the unmodified resist while the CO_2 facilitates diffusion through the crust. A number of patents also have reported using $scCO_2$ along with additives for post etch residue removal [108, 109]. However, detailed information such as composition of these mixtures, interactions between the additives and CO_2, phase behavior of the mixtures or the removal mechanisms has not been reported. Several groups have built high pressure chambers to process wafers of different sizes [99, 110-112]. These systems operate in a closed loop in which the CO_2 is recycled after removing the co-solvents and the solutes. A solid CO_2 jet spray has also been employed to remove particles and molecular contaminants from wafers [90] and is probably the most mature of the CO_2 technologies. Cleaning appears to occur by two mechanisms: thermal shock or abrasion, and solvation of the contaminants in the transient liquid film formed by the impacting CO_2 particles. Companies such as Ecosnow manufacture nozzles of different shapes and sizes for generating CO_2 jet spray depending on the application [48].

2.4.3 Surfactants for CO_2

An alternative way to improve the solvent strength of CO_2 is through the use of surfactants. Surfactants are ambivalent molecules with CO_2-philic and hydrophilic (or liphophilic) groups that can form microemulsions of water-in-CO_2 (or hydrocarbon-in-

CO_2). Microemulsions involving hydrocarbons and water have been used in cleaning product formulations, polymerization media, chemical reaction media, etc. [113]. Recently, water-in-CO_2 microemulsions have been developed to improve the solubility of polar molecules in CO_2 [114]. Due to the polar nature of water, it has limited solubility in CO_2 at moderate temperatures and pressures (e.g. 0.2 wt% at 40 ^oC and 3000 psi). By using surfactants, more water can be solubilized in CO_2. The ability of a surfactant to solubilize water is denoted by water-to-surfactant molar ratio W_o^c and values up to 28 have been achieved to date [115]. Some of the surfactants are not commercially available and were synthesized by the research groups [116, 117]. Recently, water-in-CO_2 microemulsions were used for post plasma etch residue removal by Johnston's group at the University of Texas [118]. Although CO_2+surfactant or CO_2+water mixtures did not remove the residues, water-in-CO_2 microemulsions stabilized by the surfactant were able to remove most of the particles generated in the vias after partly ashing the post plasma etch residue. However, photoresist removal was not investigated in this study. Rather, the role of the surfactant was to reduce the interfacial tension between the particle and CO_2, and the wafer and CO_2 so that the attractive force between the wafer and the particle was overcome. No damage was observed to the low-*k* dielectric after these treatments. The same surfactant ((octa)ethylene glycol) 2,6,8-trimethyl-4-nonyl ether) was also used to dry high aspect ratio photoresist patterns after developing them in aqueous solutions [100]. Even pure supercritical CO_2 was able to dry the patterns without collapsing them due to the low interfacial surface tension between water and CO_2 (20 mN/m). Addition of the surfactant accelerates the water removal rate and further decreases the interfacial tension to 1 mN/m.

2.5 Organization of the thesis

From the discussion in the previous sections, it is clear that the current methods of post etch residue removal may not satisfy the technical and environmental requirements for future device generations. CO_2 based approaches may solve some of the issues such as via wetting, conservation of chemicals and DIW, compatibility with low-*k* etc. Although CO_2-co-solvent mixtures and microemulsions in CO_2 have been demonstrated recently for photoresist processing, post etch and post ash residue removal, there is a lack of fundamental understanding regarding how these residues interact with the cleaning solutions and what criteria must be met for a mixture to be effective in removing these residues. Some of these mixtures also failed to remove the residues when they were evaluated on test samples used in this work. As shown by Perrut and others [107], solubility parameter may not be a reliable method to predict solubility in CO_2 even in the case of a simple photoresist. The etch residues are much more complex than photoresists and little information is available on how to select co-solvents to remove these residues. In some cases, the approach is mostly Edisonian with a multitude of solvents added to CO_2 in a closed vessel and conclusions drawn based on the wafer being clean or not clean. There has been very little information on the phase behavior of some of these mixtures, and the surface processes that occur in these systems. In this dissertation, a single phase liquid mixture has been developed that appears to remove etch residues without adverse impact on low-*k* films. This thesis also focuses on the development of an understanding of the chemical nature of the residues and how they interact with the CO_2 based cleaning mixtures.

Chapter 3 describes the experimental apparatus used and the analytical techniques employed in this study. A brief description of the experimental procedures is provided along with the theory behind the various surface analytical and compositional techniques used to characterize film samples and surfaces. Chapter 4 contains a detailed analyses of the patterned dual stack CORAL™ samples that are used as test structures in this thesis. In order to understand how the crust interacts with the cleaning mixture, blanket fluorocarbon films were deposited on Si wafers to emulate the etch residues. Their deposition procedure and compositional and bonding analysis is described. In Chapter 5, appropriate co-solvents are identified that can remove the etch residues completely. The phase behavior of these mixtures is reported in the form of bubble point curves in Chapter 6. Cleaning studies showing the effect of parameters such as treatment time, temperature, and composition are also reported. The importance of the phase state on cleaning is delineated. Chapter 7 contains results from mechanistic studies performed on blanket fluorocarbon and various photoresist films. The role of each component in the cleaning mixture is investigated along with insight into residue removal mechanisms. Chapter 8 contains results from compatibility studies performed on a porous dielectric film (MSSQ). Besides blanket etch rates and bonding analyses, pore size measurements were also performed on porous low-*k* films to understand the effect of high pressure as well as specific chemical additives. Chapter 9 summarizes the contributions of this research and provides suggestions for future work in this area.

CHAPTER 3

EXPERIMENTAL METHODS AND ANALYTICAL TECHNIQUES

3.1 High pressure cleaning system

From a safety point of view, it is desirable to minimize the volume of high pressure equipment such as reactors, pumps, tubing etc. Another advantage of having small reactor volumes for cleaning studies is conservation of consumables such as CO_2, co-solvents, test samples etc. Hence the high pressure cleaning experiments in this work were performed in a table top system that is capable of handling samples 1cm×1cm in size. The schematic of the system is shown in Figure 3.1. It consists of a stainless steel four-way cross (Swagelok, ¾″) installed vertically and equipped with necessary tubing and high pressure valves. Two high pressure syringe pumps (Isco, models 500D and 260D) are used to pressurize and pump CO_2 and the co-solvent mixture. Check valves (Swagelok, CH series) are used to prevent any backflow into the pumps. The fluids are mixed in another four-way cross (horizontal) with a magnetic Teflon lined stir bar. The intermixed fluids also pass through a 6″ static mixer (Koflo, series 275) with helical groves inside to facilitate better mixing of the streams. The mixing chamber, tubing and the cleaning chamber are all heated with heating tapes. The cell and the tubing are heated uniformly to ensure that the fluid inside reaches the desired temperature. The sample is fixed on a small stub by a hex cap screw and is loaded through one of the ports on the cross. The fluid enters through a second port behind the sample and leaves through the port underneath. The fourth port is used for measuring temperature in the cell about 1″

from the sample surface using a thermocouple (Omega, K-type). The cleaning process is run at constant flow rates of CO_2 and the co-solvents while the pressure is kept constant using a micrometering valve (Hoke, 1300 series with C_v=0.01) at the exit. The micrometering valve is also heated to prevent it from getting blocked by the dry ice formed as a result of Joule-Thompson cooling. The liquid from the exhaust condenses into a waste container while the gas is exhausted into the fume hood.

It is important to know if fluid in contact with the sample is in the desired phase state. Due to incomplete mixing or insufficient time for equilibration, more than one phase may be in contact with the sample. The flow rates in the high pressure system are kept low (200 ml/hr for CO_2 and <100 ml/hr for the co-solvent) so that the fluids have time to mix and equilibrate before they reach the cell. At 200 ml/hr, the residence time of CO_2 in the system is 15 min. The cell is also equipped with an optical grade sapphire window (Esco products, 3 mm thick) to allow visual monitoring during the cleaning process. A borescope (Olympus, Model D040-032-000-60) connected to a video monitor (Philips, Model LTC 2814/60) provides an expanded view of the surface and also the capability to record the observations. The fluid inlet is on the backside of the sample holder so that any entrained liquid droplets cannot condense directly on the sample surface. Another precaution taken to prevent liquid condensation on the sample is inclusion of a long purge step (with CO_2) after the exposure time. Depressurization is also done slowly (>5 min) to prevent residual liquids in the lines from condensing on the sample. Samples with condensed liquid on the surface are discarded and the experiment repeated.

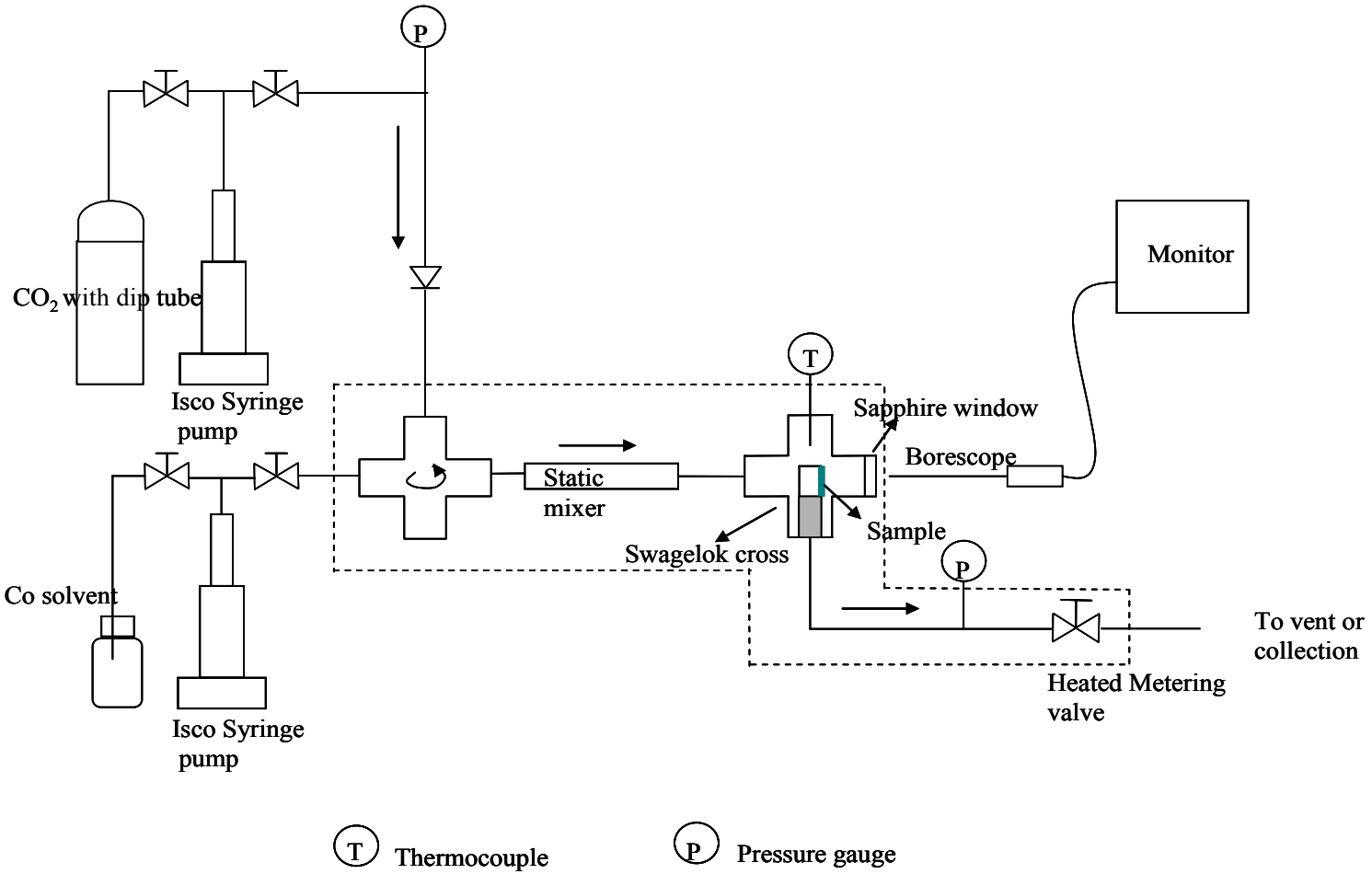

Figure 3.1. Schematic of the table top high pressure cleaning system used in this work. The section inside the dotted lines is heated.

The tubing and the high pressure valves on the system are rated to at least 3500 psi. However, the system is limited in pressure by the sapphire window assembly to ~3200 psi. Hence, the sapphire window is used only when a new recipe or new conditions are tested. When using previously studied additives or conditions, the port is capped off with a plug. The entire system is enclosed in a Plexiglass (¼″) enclosure connected to the house exhaust so solvent vapors from possible leaks do not enter the lab atmosphere. This enclosure also serves as an additional line of protection against potential rupture of the sapphire disk.

3.2 Titrimetric analysis

Titrations are used to identify the nature and concentration of the salt in the cleaning solutions. As CO_2 is bubbled through these basic solutions, acid-base reactions take place leading to formation of carbonate/bicarbonate salts. Titrimetric analysis is also used to determine the optimum protocol for cleaning the system after each experiment to avoid cross contamination and thus anomalous results. After each experiment, de-ionized water was flushed through the system and a sample collected for titration analysis to estimate the concentration of residual salts. A simple test to identify bicarbonate over carbonate or hydroxide is by adding a drop of phenolphthalein indicator – the solution turns pink if pH>8.3 (hydroxide or carbonate) or remains colorless when pH<8.3 (bicarbonate). The exact concentrations of tetramethylammonium hydroxide (TMAH), tetramethylammonium carbonate (TMA_2CO_3), and tetramethylammonium bicarbonate ($TMAHCO_3$) are determined by HCl titration. The end points are detected by a pH indicator as well as a calibrated pH meter (Corning, model 440). Non-aqueous solutions

are diluted in DIW for the titrations. Because of the difference in pK_a (or basicity) of the anions, the shape of the titration curve is different when more than one anion is present in the solution. Figure 3.2 displays typical titration curves of TMAH and TMAH-TMA_2CO_3 mixtures. The double inflexion the in TMAH-TMA_2CO_3 mixture corresponds to the phenolphthalein end point (OH^- only) and acid end point (total alkalinity). In such mixtures of TMAH and TMA_2CO_3, the titrimetric analysis is used to estimate the individual species concentrations [119].

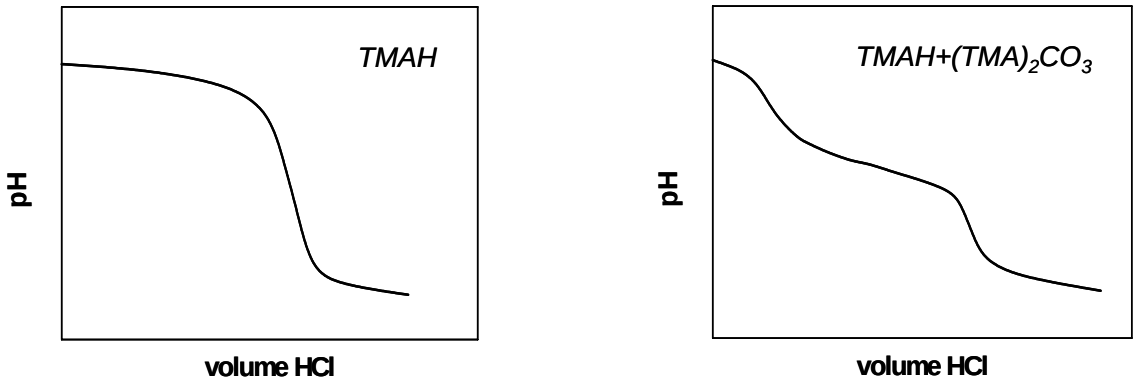

Figure 3.2. Typical titration curves of TMAH (left) and a mixture of TMAH and TMA_2CO_3 (right).

The solution is first titrated with a standard acid solution (0.1 N HCl) to acid end point to determine the total alkalinity. The total alkalinity in these solutions is given by:

$$\text{Total alkalinity} = [OH^-] + 2[CO_3^{2-}] \quad (3.1)$$

An excess of neutral barium chloride (10 wt% in water) is added to a second aliquot of the sample to precipitate the carbonate ion as $BaCO_3$; the solution is then titrated to the acid end point to determine the OH^- concentration. The carbonate concentration is then back calculated from Equation 3.1. A similar method is used for analysis of bicarbonate/carbonate mixtures. An aliquot of solution is treated with excess standard NaOH to convert all HCO_3^- to CO_3^{2-}; carbonates are then precipitated with $BaCl_2$. Excess NaOH is immediately titrated with standard HCl to determine the amount of HCO_3^-. The CO_3^{2-} is then estimated from the total alkalinity ($[HCO_3^-]+2[CO_3^{2-}]$ in this case) by titrating a second aliquot to acid endpoint. The presence of the sparingly soluble barium carbonate does not interfere in these titrations provided that the concentration of barium ion is greater than 0.1 M [119].

3.3 X-ray photoelectron spectroscopy

X-ray photoelectron spectroscopy (XPS), also known as electron spectroscopy for chemical analysis (ESCA), is a highly sensitive technique for measuring surface atomic composition [120]. It has been extensively used in the microelectronics area to evaluate cleaning and surface preparation, as well as composition and bonding structures of dielectric and barrier films. XPS has also been used to study the composition of fluorocarbon residues that are generated during plasma etching.

XPS relies on measuring the binding energy of photoelectrons emitted from core shells when a monochromatic x-ray beam hits the sample (photoelectric effect, Figure 3.3). Binding energy is a measure of the attractive force between the electron and the

nucleus. The magnitude of this force depends on the charge of the nucleus – hence, every atom has a characteristic binding energy and XPS uses this principle to identify atoms. During this process, photoelectrons are also emitted from outer shells of the atom – however, the electrons emitted from a core shell without inelastic energy losses are the ones that are used to calculate the composition. The concentration of the atom giving rise to the photoelectron is estimated by taking into account the geometry of the system, atomic mass, photoemission cross-section, electron attenuation length, and spectrometer transmission and detection efficiency. In order to minimize loss of kinetic energy of the photoelectrons, the analysis is done under ultra-low vacuum ($<5\times10^{-9}$ torr) to avoid collisions with other electrons or residual gas molecules. Ultra-low vacuum also prevents spectral interference from adsorbed gas molecules that may occur at higher pressures. An electron energy analyzer collects the photoelectrons and measures their kinetic energy while an electron detector counts the number of photoelectrons emitted. The binding energy of the electrons is related to the kinetic energy by the expression:

$$E_{KE,P} = h\upsilon - E_{BE,P} - \phi_{sp} \tag{3.2}$$

where, $E_{KE,P}$ is the kinetic energy of the photoelectron (measured by the detector), $h\upsilon$ is the energy of the x-ray beam, $E_{BE,P}$ is the binding energy of the photoelectron, and ϕ_{sp} is the work function (which is a constant for a given spectrometer). Because of the low kinetic energy of the photoelectrons, the electron attenuation lengths are very small (order of 3 nm) and therefore this technique is highly surface sensitive. Only electrons emitted within 3-5 times the attenuation lengths reach the detector and hence only the top 1-10 nm of the surface is probed. The sensitivity of this technique is 0.01-1 atomic%.

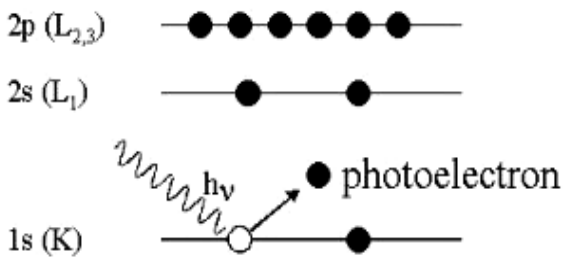

Figure 3.3. Schematic of photoelectric effect which is the basis of XPS.

Besides atomic composition, XPS also provides information on the bonding structure and composition variation with depth into a film or surface. When an atom is bonded to a more electronegative atom, the outer shell electrons are pulled towards the electronegative atom leading to a slight positive charge on the nucleus. This leads to the inner core electrons being held more strongly by the nucleus. Hence, the binding energy of the core electrons shifts to higher energies. This shift in binding energy can provide information on the bonding structure of the material being analyzed. For example, when C is bonded to a single fluorine atom, the binding energy of its primary photoelectron shifts from 284.8 eV to about 288 eV. If it is bonded to more than one fluorine atom, the shift is even higher (around 290 eV for $–CF_2$- and 293 eV for $–CF_3$). By fitting Gaussian-Lorentzian shapes to carbon peaks, one can estimate the percentage of atoms with various bonding configurations (from the area under the peaks). The intensity of photoelectrons also depends on the geometry of the system – the angle between the sample surface and total intensity is an integral over the photoelectrons emitted at various depths. The

detector can be changed to probe deeper or shallower into the film. At any angle, the intensity of photoelectrons I_A from an element A is given by [121]:

$$I_A = \sigma_A^X(h\upsilon)D(E_A)\int_{\gamma=0}^{\pi}\int_{\varphi=0}^{2\pi} L_A(\gamma)\int_{y=-\infty}^{\infty}\int_{x=-\infty}^{\infty} J_0(x, y, \delta)T(x, y, \gamma, \varphi, E_A) \times \int_{z=0}^{\infty} N_A(x, y, z)\exp\left[-\frac{z}{\lambda_M(E_A)\cos\theta}\right] dxdydzd\varphi d\gamma \quad (3.3)$$

where,

$\sigma_A^X(h\upsilon)$: cross-section of electron emission from shell X by a photon of energy $(h\upsilon)$

$D(E_A)$: detection efficiency for each electron transmitted by the electron spectrometer

$\gamma, \varphi, \delta, x, y, z$: coordinates as shown in Figure 3.4

$L_A(\gamma)$: angular symmetry of the photoemission intensity from each atom

$J_0(x, y, \delta)$: flux of the x-ray photons per unit area at point (x,y) on the sample

$T(x, y, \gamma, \varphi, E_A)$: analyzer transmission function

$N_A(x, y, z)$: atom density of A at point (x,y,z)

$\lambda_M(E_A)$: attenuation length of the photoelectrons of energy E_A from level X of atom A in matrix M

θ : angle of emission of photoelectrons from sample normal

By measuring I_A, one can estimate $N_A(x,y,z)$ using the above expression after certain mathematical manipulations. An algorithm to reconstruct concentration depth profile based on Fick's second law of diffusion from angle-resolved XPS (ARXPS) data is used in this work. The procedure and assumptions involved in this algorithm are

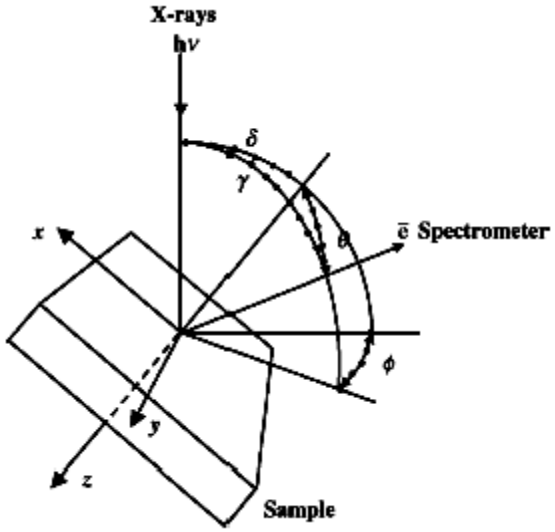

Figure 3.4. Geometry of XPS analysis configuration [121].

described in detail elsewhere [122]. For extracting composition versus depth information, XPS spectra are collected over several angles, and the data is fed into a MATLAB program [122]. A model for the concentration depth profile is assumed based on the physical processes in the film; for example, an infinite source diffusion model can describe surface oxidation of a polymer film reasonably well [122]. The program then estimates the parameters for this model by fitting the data with those estimated from Equation 3.3. This method is sensitive to the accuracy in the measured photoelectron intensities as well as in the bulk composition.

All XPS measurements in this dissertation are made on a PHI 1600 model XPS system with a work function ϕ of 3.7 eV. It is equipped with a monochromatic AlKα source (1486.7 eV) generated using a water cooled anode operating at a power of 350 W.

Data collection is performed using PHI Explorer software (Physical Electronics, v3.4) and is analyzed using Multipak software (Physical Electronics, v5.0A). The photoelectrons emitted are collected and analyzed in an 180^{o} hemispherical analyzer and multichannel detector. The C1s peak (284.8 eV) is used as a reference to maximize the photoelectron count by adjusting the position of the sample relative to the source and the detector. Survey (low resolution) scans are collected first (0.5 eV, 50 ms/step) to identify all the chemical elements on the surface. Then, high resolution spectra are collected with a different set of conditions (0.05 eV and 200 ms/step) for each of the elements detected. Unless specified, these spectra are collected at 45^{o} and a pass energy of 23.5 eV. For angle-resolved XPS (ARXPS), the spectra are collected at photoemission angles ranging from 20^{o} to 70^{o} at 5^{o} intervals. Non conducting samples undergo surface charging that results in drifting peak positions – this is overcome by using a low energy electron flood gun to neutralize the charge buildup. The C1s peak at 284.8 eV is again used as a reference to adjust the neutralizer settings. If necessary, peak deconvolution is performed using Gaussian-Lorentzian peaks while minimizing the error between the actual data and the sum of the deconvoluted peaks.

3.4 Attenuated total reflection – Fourier transform infrared spectroscopy

Attenuated total reflection - Fourier transform infrared (ATR-FTIR) spectroscopy relies on measuring the time resolved FTIR absorption of an evanescent wave propagating through the material being analyzed [123] and is illustrated in Figure 3.5. When an electromagnetic wave passes from a dense to a rare material, total internal

reflection of the wave occurs provided that the angle of incidence of the wave satisfies the relation:

$$\theta > \theta_c = \sin^{-1}\left(\frac{n_1}{n_2}\right) \tag{3.4}$$

where, θ_c is the critical angle of incidence, n_1 and n_2 are the refractive indices of the dense and rare media respectively. When this occurs, an exponentially decaying electromagnetic wave called evanescent wave propagates through the rare medium. The magnitude of the wave (E) can be expressed as:

$$\frac{E}{E_0} = \exp\left(-\frac{z}{d_p}\right) \tag{3.5}$$

where, E_0 is the field strength at the interface, z is the depth into the rare medium, and d_p is the depth of penetration of the wave. The penetration depth of this wave is defined as the distance where the intensity falls to 1/e of the original intensity. The penetration depth can be estimated using the equation:

$$d_p = \frac{\lambda}{2\pi n_1 \sqrt{\sin^2\theta_1 - \left(\frac{n_2}{n_1}\right)^2}} \tag{3.6}$$

where, λ is the wavelength of light, n_1 is the refractive index of the dense medium, n_2 is the refractive index of the rare medium, and θ_1 is the angle of incidence of the wave. If a film or a liquid of interest is placed within this penetration depth, the characteristic spectrum of the material can be collected. By having the wave reflect internally multiple

times, the effective path length, and hence, the absorbance can be increased. This is an advantage of ATR-FTIR – it has improved sensitivity for thin films. Hence FTIR spectra of very thin films such as self-assembled monolayers (SAMs) or Langmuir-Blodgett films [124] can be collected by this approach. Another advantage of this method is the ability to perform *in-situ* analysis while the film is being exposed to a liquid or a vapor.

A common application of this *in-situ* technique is estimation of diffusivities of molecules through polymer systems or inter-diffusion of polymers [124, 125]. In particular, specific interactions such as hydrogen bonding between the solute and the polymer or between two solutes were monitored by this technique. This is a relatively inexpensive and simple technique and can be implemented in an ordinary FTIR system with appropriate accessories.

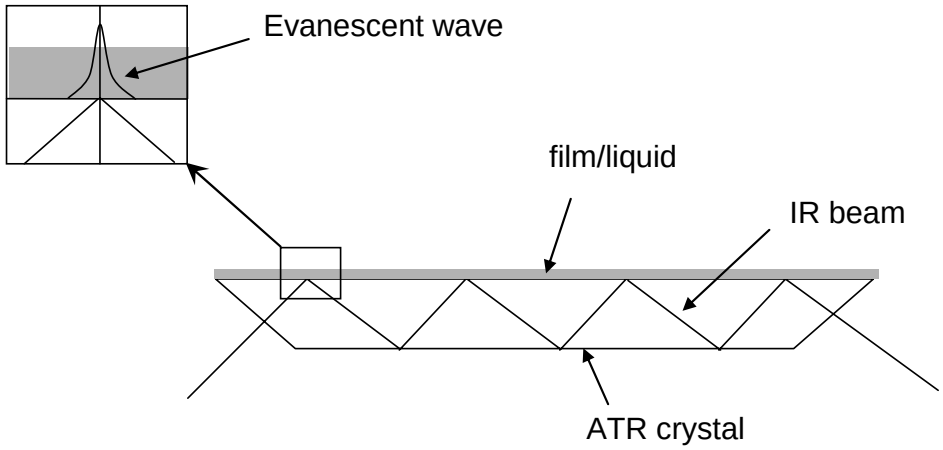

Figure 3.5. An illustration of the ATR-FTIR technique.

In this dissertation, ATR-FTIR technique is used to study the modification of plasma deposited fluorocarbon films by the cleaning solutions. These fluorocarbon films are deposited to simulate the etch residue generated during plasma-assisted patterning of dielectric films. The ATR crystal for this application has to meet the following criteria:

1. The crystal must be transparent in the range 700-3500 cm^{-1}: Many crystals have the low wavenumber cut off above 1200 cm^{-1} but the signature peaks for fluorocarbons lie in the 500-1200 cm^{-1} range.

2. The crystal must be chemically resistant to water, solvents such as methanol, and weak bases such as $TMAHCO_3$ which are constituents of the cleaning mixtures.

3. The crystal material must have a high modulus of rupture and Knoop hardness for high pressure applications.

4. The crystal should be inexpensive and be readily available.

ZnSe has a useful ATR range from 700-20000 cm^{-1}, is fairly hard (modulus of rupture of 8000 psi and Knoop hardness of 150) and is inert to common solvents and weak bases [126]. Hence, ZnSe is chosen as the ATR crystal material. It is however incompatible with acids or strong alkali solutions. The high pressure ATR cell used in this work is based on the cell designed by T. Kamal [127] that uses Si crystals polished to custom specified dimensions (72mm×30mm×3mm). Custom built ATR crystals are expensive and have delivery times of 8-12 weeks. Hence, the cell was redesigned and rebuilt to use smaller crystals that can be purchased off the shelf (Harrick Scientific, 50mm×20×2mm). The cell was made of SS-304 and has ports for fluid inlet and outlet

(1/16″ NPT) and tapped bores for a cartridge heater and a thermocouple (Figure 3.6). An O-ring made of AFLAS (American Seal, Duro 80) is used to seal the fluid between the ATR crystal and the cell. A top plate is used to apply uniform force on the crystal with the help of hex cap screws. The top plate of the cell was also modified to use 8 #6-32 hexagonal cap screws made of high strength black alloy steel (McMaster-Carr, 180000 lbf/in^2) for higher pressure rating (3500 psi with a safety factor of 3.6). The size of the crystal is 50mm×20mm×2mm and it allows 13 reflections at the top (larger) side and 12 reflections at the bottom.

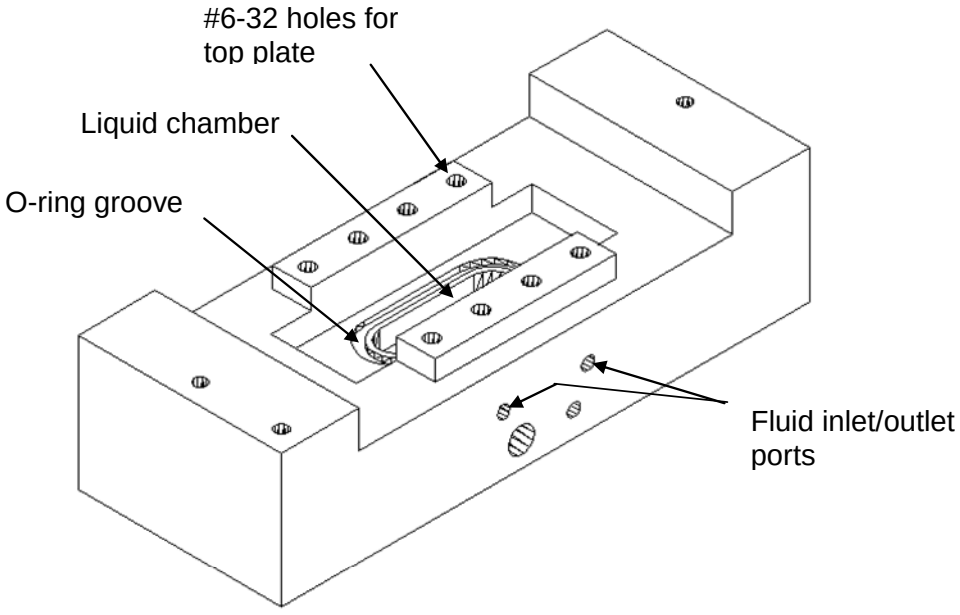

Figure 3.6. A 3-D isometric view of the high pressure ATR-FTIR cell used in this work. The top plate and the ATR crystal are not shown.

A Bruker IFS66v/S spectrometer equipped with a DTGS detector is used for the FTIR measurements. In general, 512 scans are collected from 400 cm^{-1} to 4000 cm^{-1} with and without the film on the crystal and the transmittance ratios are recorded. The sample chamber is pumped down to 2 mbar to prevent interference from H_2O or CO_2 present in the atmosphere. Data collection and analysis is performed using OPUS software (Bruker Optik GmbH, v3.1). FTIR data interpretation is performed using a handbook containing infrared characteristic group frequency tables and charts [128].

3.5 Dissolution rate monitor

A common metric employed to study development of photoresists is dissolution rate. Dissolution rate data provide information on the resist contrast and minimum radiation dose required to clear the resist. Rates can be measured *ex-situ* by measuring thickness after developing the resist for incremental periods of time. But this is time consuming and may not capture very fast dissolution rates. *In-situ* techniques for dissolution rate measurement have also been developed based on interferometry (reflectometry) and ellipsometry. Because of its simplicity and ease of implementation in a laboratory or a fabrication facility, interferometry has been used for a number of applications such as photoresist dissolution [129], plasma deposition, end point detection during plasma etching [130]. In this work, a multiwavelength interferometer (MWI) is used to study dissolution of photoresists in aqueous solutions to provide insight into the primary role of each component in the cleaning mixture.

An interferometer is based on the principle of constructive and destructive interference of light reflected from various interfaces in a film stack, which permit calculation of the thicknesses and/or optical properties of the transparent films. Shown in Figure 3.7 is an illustration showing light being reflected from various interfaces during the development of a photoresist film on a silicon substrate. n_i and k_i are the refractive index and extinction coefficient of the layer i respectively. The intensity of the resulting light can be calculated using the expression [131]:

$$I = \frac{R_1^2 + R_2^2 + 2R_1R_2\cos(2\delta - \varphi)}{1 + R_1^2R_2^2 + 2R_1R_2\cos(2\delta - \varphi)} \tag{3.7}$$

where, R_1 are R_2 are the amplitudes of the light reflected at the liquid-film and film-substrate interfaces respectively, $\varphi = \tan^{-1}\left(\frac{2n_1k_2}{n_1^2 - n_2^2 - k_2^2}\right)$ is the phase change introduced due to the absorbing substrate 2 and $\delta = \frac{2\pi dn_1}{\lambda}$ is the phase change due to the path difference introduced by the film of thickness d.

For a resist film on a silicon substrate being developed in an aqueous solution, typical values for n, k and R are given in Table 3.1. One can neglect ϕ since k_2 is small (<0.1). The denominator in Equation 3.7 is also small since it involves the product of two small (<1) numbers; hence the equation simplifies to:

$$I = R_1^2 + R_2^2 + 2R_1R_2\cos\left(\frac{4\pi dn_1}{\lambda}\right) \tag{3.8}$$

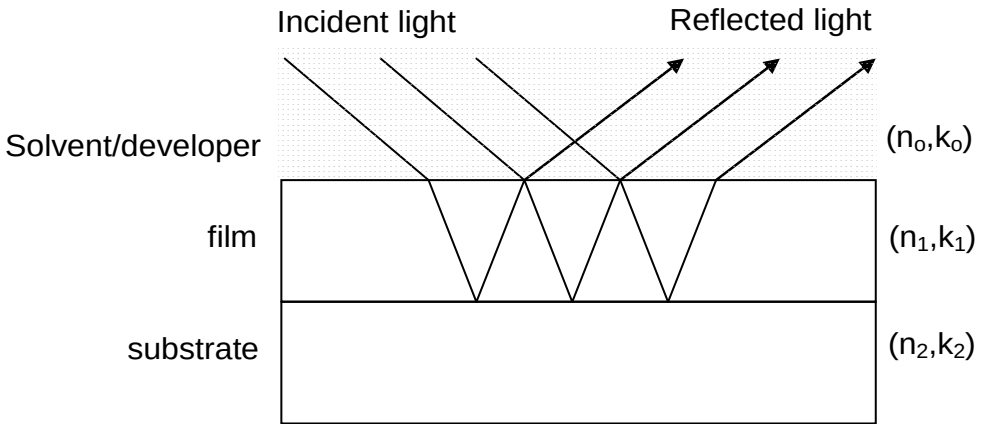

Figure 3.7. Schematic showing light reflecting from various interfaces during dissolution rate monitoring studies.

In the single wavelength configuration, monochromatic light impinges on a film and the intensity of the reflected light is monitored as a function of time. The phase difference between these waves depends on the refractive index and thickness of the film – hence, maxima and minima appear in the reflectance versus time spectrum as the film

Table 3.1. Values for n, k, and R for a PHOST film on silicon substrate being developed in an aqueous solution.

Layer number	Layer	n	k	R
0	Developer (@589 nm)	1.33	0	-
1	PHOST (@589 nm)	1.64	0	0.1043
2	Silicon substrate (@633 nm)	3.875	0.018	0.4052

dissolves. Mathematically, this occurs when the cosine term in Equation 3.8 goes to -1 or +1 for which the term $\frac{4\pi dn_1}{\lambda}$ must be an integral multiple of π. The thickness of the film can then be estimated using the equation:

$$d = \frac{p\lambda}{4n_1} \tag{3.9}$$

where, p is the peak number (an integer corresponding to the number of maxima/minima encountered starting from zero thickness), λ is the wavelength of light and n_1 is the refractive index of the film. However, the single wavelength interferometer has certain limitations [129]. It can be used only after the end point (zero thickness) is reached, and is not suitable for films that swell or those that dissolve fast (>100 nm/s). This is due to nature of expression 3.9 in which the integer p is unknown everywhere except at the end point where p=0. The thickness values can then be calculated by incrementing p by 1 at each minimum or maximum. For this reason, a more robust alternative is multiwavelength interferometry (MWI) in which a multiwavelength light source is used to collect reflectance versus wavelength data [129].

In MWI, expression 3.8 is again used to calculate the thickness but with data at various wavelengths. The reflected intensity is modeled as a function of λ at any given time during dissolution. Hence, thickness can be estimated at more points than when a single wavelength approach is used – this enables detection of surface inhibition or surface acceleration effects during photoresist dissolution that are difficult to capture using single wavelength techniques. In addition, the data is more accurate as more points

are used for curve fitting. This technique can also be applied to films that swell or those that are very thin (<200 nm) [129].

The dissolution rate monitor (DRM) used in this work is described in detail elsewhere [129] and is shown in Figure 3.8. It consists of an Ocean Optics PC2000 plug-in spectrometer operating in the 450–950 nm range. An optical probe with 6 incident light fibers and 1 reflectance fiber is used to illuminate the sample and collect the reflected light from the sample. The light source used is a LS-1 tungsten halogen white light source (360 nm – 1100 nm). The probe is aligned normal to the sample using micrometers to maximize the reflected intensity. A background reflected intensity is first collected from the substrate without the film or the developing solution present. A

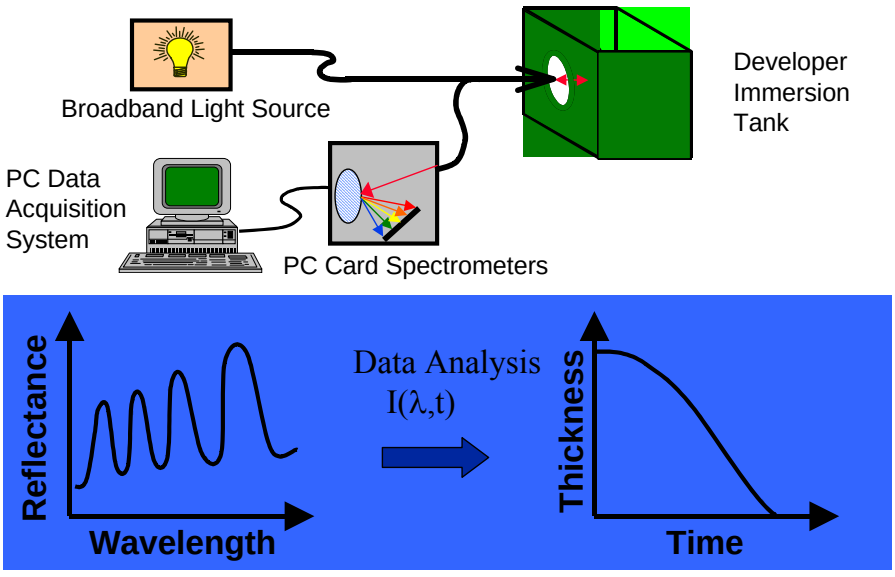

Figure 3.8. Schematic of the DRM set-up and data analysis [129].

puddle of solution is then dispensed on the sample while simultaneously starting data collection. Data acquisition is done using a LabVIEW software application [129]. The data obtained from this set-up consists of scans of reflectance versus wavelength at different time intervals during the dissolution process. This data is then used to estimate thickness of the film as a function of time. From Equation 3.8, it is clear that reflected intensity at any time is a periodic function of $\frac{n_1}{\lambda}$. Hence, reflected intensity is plotted as a function of this variable (also known as 'effective frequency', f). The experimental intensity is then fitted to a model of the form:

$$I = \left(af^2 + bf + c\right)\cos\left(4\pi df\right) + \left(ef^2 + gf + h\right) \tag{3.10}$$

where the thickness d and fitting parameters (a, b, c, e, g, h) are the unknowns. This procedure is repeated on data collected at different times to produce resist dissolution profiles.

The above analysis assumes that k_2 and the denominator in Equation 3.7 are negligible. In cases when these assumptions do not hold, Equation 3.8 can be modified accordingly but the procedure remains unchanged. However, the optical constants of the film (n_1, k_1) may not be constant as the film dissolves – this occurs when the film is swollen or chemically modified by the solvent. In such a scenario, the refractive index of the film may also be considered an unknown (along with the thickness). In addition to the periodicity of the spectrum, the intensity of the reflected light is also used to obtain both the refractive index and the optical constants. Expressions based on rigorous analysis have been developed to compute the reflected intensity as a function of thickness

and optical properties of the film – these expressions can be used to fit the experimental data [13].

3.6 Variable angle spectroscopic ellipsometry

Ellipsometry is a very sensitive technique to analyze thin films and surfaces using elliptically polarized light. In this technique, the change in polarization of incident light is correlated to the properties of the material being analyzed such as thickness, refractive index, surface roughness, anisotropy etc. [132]. Its high sensitivity arises from the fact that only the ratio and not the actual intensities of reflected light is used. Hence, it is not affected by small fluctuations in the incident light intensity and is highly reproducible. A simple ellipsometer consists of a light source, polarizer, sample stage, and a detector. Light from a broadband light source passes through a monochromator and a polarizer where it is linearly polarized at each wavelength before it illuminates the sample. The incident light is partly reflected from the surface and partly refracted into the film. Upon interaction with the film, the reflected light undergoes a change in polarization from linear to elliptical (hence the name 'ellipsometry'). The intensity and polarization state of the reflected light is measured by the detector and two parameters ψ and Δ are estimated using the following equations:

$$\frac{R_p}{R_s} = \tan(\psi)e^{i\Delta} \tag{3.11}$$

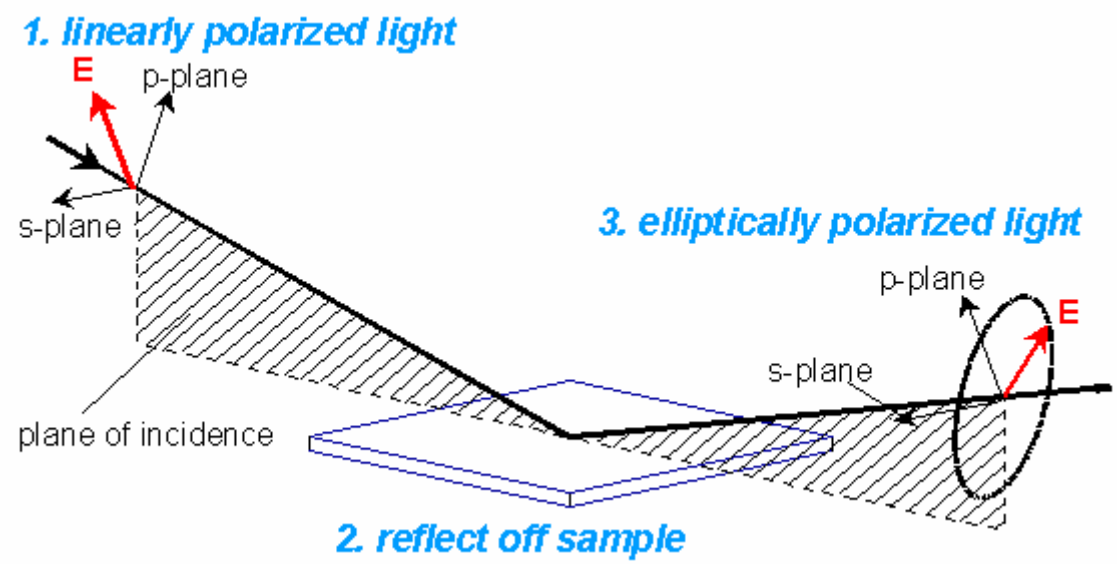

Figure 3.9. Geometry of ellipsometric measurement [133].

where, R_p and R_s are the reflectance of p-polarized (parallel to the plane of incidence) and s-polarized (perpendicular to the plane of incidence) light respectively. R_p and R_s are known as Fresnel coefficients and can be calculated theoretically by considering the infinite series of reflections and transmissions that occur at various interfaces. The optical constants (refractive index, n and extinction coefficient, k) and thicknesses of each layer determine the reflected, transmitted and refracted intensities and angles and the corresponding phase changes. The experimental data is then fitted to calculated values from a model for determining the unknown optical constants and the thicknesses. Appropriate initial guesses will lead to faster convergence of the optimization algorithm. A model consists of a known number (and order) of layers with appropriate dispersion relations for each layer. For simple dielectric, polymer and semiconductor films analyzed

in this work, Cauchy relation can be used to model the dependence of optical constant on wavelength [134]:

$$n(\lambda) = A + \frac{B}{\lambda^2} + \frac{C}{\lambda^4} \tag{3.12}$$

where, A, B, and C are known as Cauchy parameters. Even in materials that absorb in the UV range, Cauchy relationships can be used in the visible and near-IR range.

A variable angle scanning ellipsometer (VASE) collects data at multiple angles over a range of wavelengths providing better data fit and hence accurate parameter values. Hence, films with non idealities such as surface roughness, anisotropic optical properties or thickness non uniformities can also be analyzed due to the availability of large amounts of data from this technique (as opposed to single wavelength ellipsometry). Film measurements in this dissertation have been performed on two different ellipsometers – VASE and M-2000 (J. A. Woollam Co.). For a more accurate point-by-point fit of n and k, a VASE instrument is used. It consists of a rotating analyzer for greater accuracy and is insensitive to source polarization. Most of the measurements are made over the wavelength range of 200 nm-1100 nm with a step size of 2 nm at three different angles 65^o, 70^o, and 75^o. These angles are chosen because the maximum sensitivity of this technique to material properties occurs at the Brewster angle of the film. For solid films, the Brewster angle lies between 56^o and 80^o. All other routine thickness measurements are made on a phase modulation ellipsometer (M-2000 instrument). It has a photo elastic modulator and is CCD based – therefore, it can collect data over a wide range of wavelengths simultaneously. Hence, it has faster theoretical data collection rates but at broader resolution. Data collection and analysis are performed

using WVASE32™ software [134]. The software uses a Marquardt-Levenberg algorithm to determine the best fit by minimizing the mean square error (MSE) between the experimental and calculated model data. The resulting fit was evaluated to ensure that it is physically meaningful and satisfies common rules such as:

1. n must decrease with increasing wavelength for films with k=0 (normal dispersion).
2. For absorbing samples, k>0 (anamolous dispersion).
3. For metals, n and k generally increase with wavelength.
4. The values for thicknesses, n, or k must be non negative.

3.7 Positronium annihilation lifetime spectroscopy

In this work, the pore size and pore interconnectivity in a methyl silsesquioxane (MSSQ) film is measured before and after treatment in CO_2-$TMAHCO_3$-methanol cleaning mixtures to ensure that the cleaning mixtures are compatible with porous low-*k* films. The techniques to study pore sizes in thin films can be classified [135] as stereological (transmission electron microscopy, atomic force microscopy, scanning tunneling microscopy), nonintrusive methods based on radiation scattering (wave propagation, positronium annihilation lifetime spectroscopy), and intrusive methods based on gas adsorption, mercury porosimetry, and calorimetric methods. Positronium annihilation lifetime spectroscopy (PALS) has recently been used to study the integration challenges of porous low-*k* films with Cu metallization [136, 137]. In this method, a

monoenergetic positron (e^+, antiparticle of electron) beam from a radioactive source (^{22}Na) is directed at the sample. Several outcomes are possible when a positron interacts with porous material as shown in Figure 3.10 [138]. The interaction that is of interest for the PALS technique is the positronium (Ps, the electron-positron bound state) formation and subsequent decay. The positron can capture an electron from the dielectric and forms positronium – two spin configurations are possible, ortho or para. The p-Ps annihilates in 0.125 ns while the o-Ps has much larger lifetimes and hence longer path length in the medium. When a o-Ps is trapped in the pores, it decays faster due to 'pick-off' annihilation with molecular electrons from the pore surface. Hence, while the lifetime of

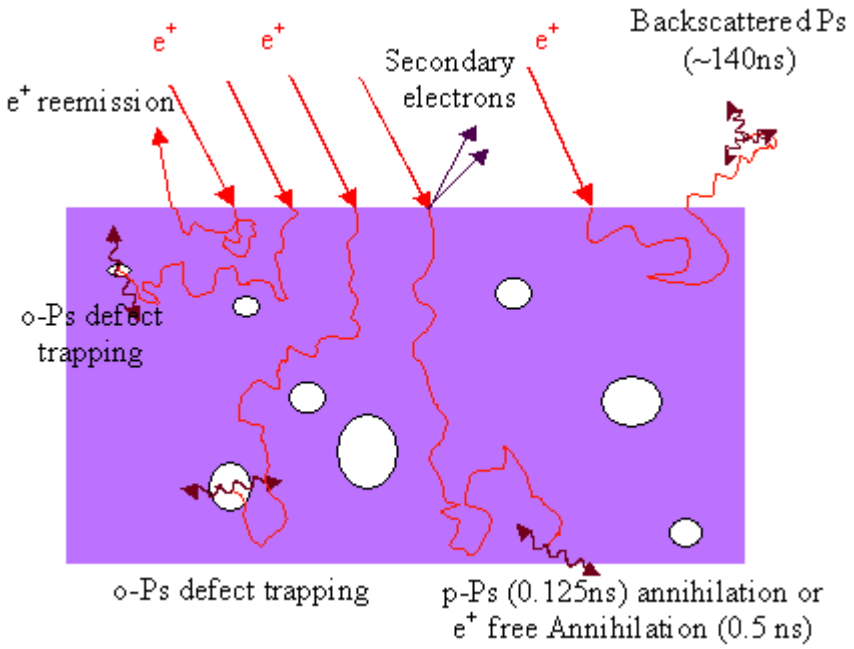

Figure 3.10. Positron and positronium interactions with porous matter [139].

a o-Ps in vacuum is 140 ns, it is smaller when trapped in pores – the decrease in the lifetime is related to the pore size (volume/surface area or l, characteristic size). Experimentally measured o-Ps lifetimes are thus converted to pore sizes using a calibration chart. It has been shown that the pore size estimates using PALS correlate well with other techniques like ellipsometric porosity, small angle neutron scattering, or gas absorption techniques [140]. M. P. Petkov and others [141] have used PALS to study the pore connectivity as a function of porogen loading in MSSQ films. They found that above 20 wt% loading, the pores become interconnected and open thus allowing the o-Ps to escape into vacuum. Barrier integrity tests on Ta and TaN coated films using PALS showed that the barrier must be at least as thick as the range of dielectric roughness [137]. PALS measurements after exposing MSSQ resist to an Ar plasma showed that the plasma caused damage to the pore structure on the surface of the film [136]. In fact, an O_2 ashing plasma completely destroyed the pore structure in these films. The strength of PALS lies in its ability to analyze both open (interconnected) and closed (isolated) pores, films under barriers (e.g. patterned features with diffusion barriers) and the ability to perform depth profiling (by changing the e^+ beam energy).

In this work, two kinds of measurements are made on MSSQ samples treated at various conditions at high pressures – % Ps formation and mean pore size. The percentage of positrons forming Ps (free Ps and trapped Ps) is dependent on the chemistry of the film. Certain functional groups or molecules (such as CCl_4) present in the film inhibit Ps formation by capturing free electrons that are captured by positrons to form Ps [142]. Similarly, certain molecules such as naphthalene can act as a positronium formation enhancer by scavenging holes or free radicals. For estimating the pore sizes, it

is desirable to have high intensity of trapped o-Ps for greater precision. For MSSQ films with ~29% porosity, the percentage of positrons leading to formation of trapped o-Ps is <50%. The remaining Ps diffuse into vacuum and decay at vacuum lifetime and, therefore, cannot provide information about the film. Hence, for pore size measurements, a thin film of SiO_2 or aluminum is deposited on to the MSSQ to confine o-Ps in the film. The deposited layer must be thin in order for the positrons to penetrate and implant in the film underneath. A 70 nm layer of SiO_2 (by RF sputtering) or aluminum (DC sputtering) has been used for this purpose. Care is taken to prevent the film from being heated during the deposition process because this may lead to diffusion of sputtered material into the pores. Sets of samples (one with the capping layer and one without) were sent to University of Michigan for PALS analyses. The lag time between sample generation and analysis is usually between 7-10 days.

CHAPTER 4

FORMATION AND CHARACTERIZATION OF TEST SAMPLES AND MODEL FILMS

4.1 Description of the test samples

The etch residue samples used in this study were generated at International SEMATECH and have arrays of vias ranging from 1 μm to 130 nm in size. International SEMATECH is a consortium of leading semiconductor manufacturers and provides test wafers to customers for various applications such as chemical mechanical polishing (CMP), surface cleaning, plasma etch etc. [143]. The objective is to provide necessary services for semiconductor manufacturers to develop efficient technologies. The wafers undergo processing that is similar to an existing production sequence or that is based on an emerging technology – hence, these test wafers are 'realistic models' of the actual samples currently generated in the integrated circuit (IC) manufacturing. Since, carbon doped low-*k* dielectrics are replacing SiO_2 as the intermetal dielectric (IMD), the test samples were generated by etching a dual stack CORAL™ film for damascene processing. CORAL™ is an amorphous carbon-doped SiO_2 low-*k* material developed and marketed by Novellus Systems, Inc., and deposited by plasma enhanced chemical vapor deposition (PECVD) from a siloxane precursor. The dielectric constant of this film is 2.7 (as opposed to 3.9 for thermal SiO_2) and can be lowered further by incorporating porosity [144].

The film stack consists of two layers of SiC to serve as etch stops for the vias and the trenches. SiC is also replacing Si_3N_4 as the etch stop material because of its lower dielectric constant and higher etch selectivity to the dielectric [145]. The stack also has a SiO_2 capping layer underneath the photoresist. Although the effective dielectric constant of the dielectric stack increases upon incorporation of a capping layer, this layer has several uses:

1. It serves as a hard mask and prevents damage to the dielectric during plasma etching.

2. It acts as a barrier to diffusion of contaminant species into the dielectric and the metal lines.

3. It prevents diffusion of bases (N-containing) from the dielectric to the photoresist that can result in resist poisoning.

4. It acts as a CMP mask – in its absence the dielectric has to bear the stress from CMP after the copper has been removed completely.

There are no metal lines in these samples – hence these samples may be similar to the wafers generated before the etch stop breakthrough step (step f in Figure 2.2) in dual damascene processing. An 8″ wafer was supplied with ~130 die (1.4cm×1.4cm in size) – each dice has thousands of vias of different sizes etched through this stack to the bottom etch stop layer. The etch chemistry and the process conditions are proprietary and therefore not disclosed. However, based on the trend in the industry today, it is likely that a high C:F ratio gas such as C_4F_8 was used to etch the low-*k* dielectric [146].

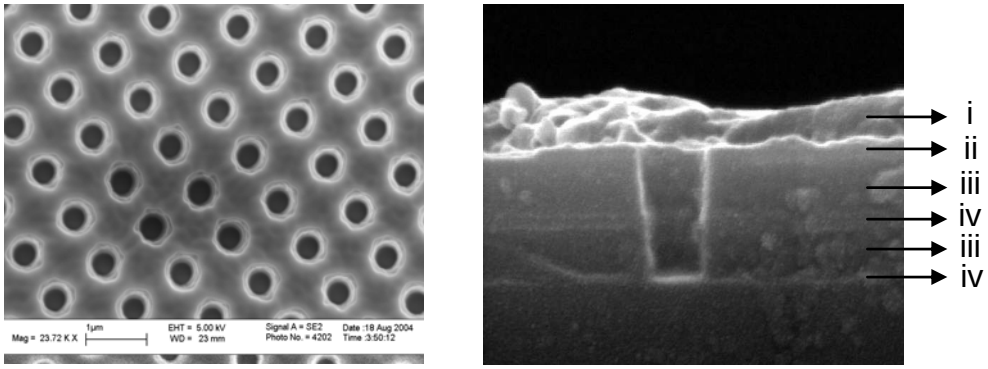

Figure 4.1. SEM images of vias on the etch residue samples used in this work: plan view (left) and cross-sectional view (right) (i) 400 nm photoresist residue and anti-reflective coating (ii) 50 nm SiO_2 capping layer (iii) 500 nm CORAL™ dielectric (iv) 50 nm SiC etch stop layer.

The type of lithography and structure of the photoresist also were not disclosed. No post etch ashing was performed and hence, the wafer has three kinds of residues: photoresist, line-of-sight, sidewall. Shown in Figure 4.1 is the plan view of an array of 250 nm vias along with the cross-sectional view of one such via. The film stack and the associated thicknesses are also indicated in the figure. The wafer was broken into small samples for cleaning studies in this work.

4.2 Etch residue sample characterization

4.2.1 X-ray photoelectron spectroscopy

XPS analysis was performed to analyze the surface bonding structure and composition of the residue sample. Shown in Table 4.1 is the atomic concentration after averaging over three different points on a sample. It should be noted that hydrogen and

helium are not detected by XPS. Since the photoelectron detection angle is 45°, some of the photoelectrons detected may have originated from the sidewalls and the bottom of the vias. No silicon was detected, which indicates that the most of the photoelectrons reaching the detector are from the top surface of the photoresist residue. The large concentrations of carbon and oxygen are from the photoresist underneath the thin fluorocarbon residue. The presence of nitrogen suggests that N_2 was one of the components in the etch chemistry. An increase in the angle between the plane of the sample and the photoelectron detector (by tilting the sample) increases the probing depth into the sample. A change of this angle from 5° to 85° decreased the fluorine concentration from 10.5% to 6% confirming that most of the fluorine is near the sample surface.

Table 4.1. XPS surface atomic composition on the etch residue samples.

Carbon%	Nitrogen%	Oxygen%	Fluorine%	Silicon%
71.3±1.5	3.8±0.3	15.1±0.4	9.8±0.9	0

As described in section 2.2.5 of this dissertation, the top of the photoresist is the most difficult to remove due to cross-linking from UV/Vis radiation, and bombardment by ions and electrons in the plasma. In order to design appropriate cleaning mixtures, it is desirable to define the bonding structure at the surface of the residue. XPS peak

deconvolution was performed on C, N, O, and F signals to delineate the bonding structure. Gaussian-Lorentzian peaks were assumed at binding energies reported in the literature for specific fluorocarbon moieties [147, 148]. Unknown peaks were identified using an XPS handbook [149]. Shown in Figure 4.2 are the deconvoluted C1s, N1s, O1s, F1s peaks along with their bond assignments. The primary peak for carbon corresponds to C-C, C-H at 284.8 eV with 55% of the atoms displaying that bonding structure (as determined from the area under the peak). Approximately 14% of the carbon atoms have binding energies around 289 eV indicating that they are bonded to one fluorine atom. However, carbon atoms with O-C=O bonding structure also appear at this energy. The high binding energy component of the N1s peak is identified as nitrogen in a quaternary ammonium salt. Thus, this peak may be a result of residue remaining on the surface from the developer (usually aqueous tetramethylammonium hydroxide solution).

4.2.2 Fourier transform infrared spectroscopy

Fourier transform infrared (FTIR) spectroscopy was used to identify bonding structures in the photoresist present on the etch residue samples. As described earlier, the bulk of the photoresist remains unmodified during plasma etching. Solvents that can dissolve photoresist may remove at least some of the etch residue on the photoresist by a lift-off mechanism. Hence, a knowledge of photoresist type (248 nm or 193 nm) and/or structure will assist in the development of chemical mixtures for etch residue removal. Because of the difference in the backbone and their acid moieties, 248 nm and 193 nm resist have different dissolution characteristics. For example, the pKa of PHOST was estimated to

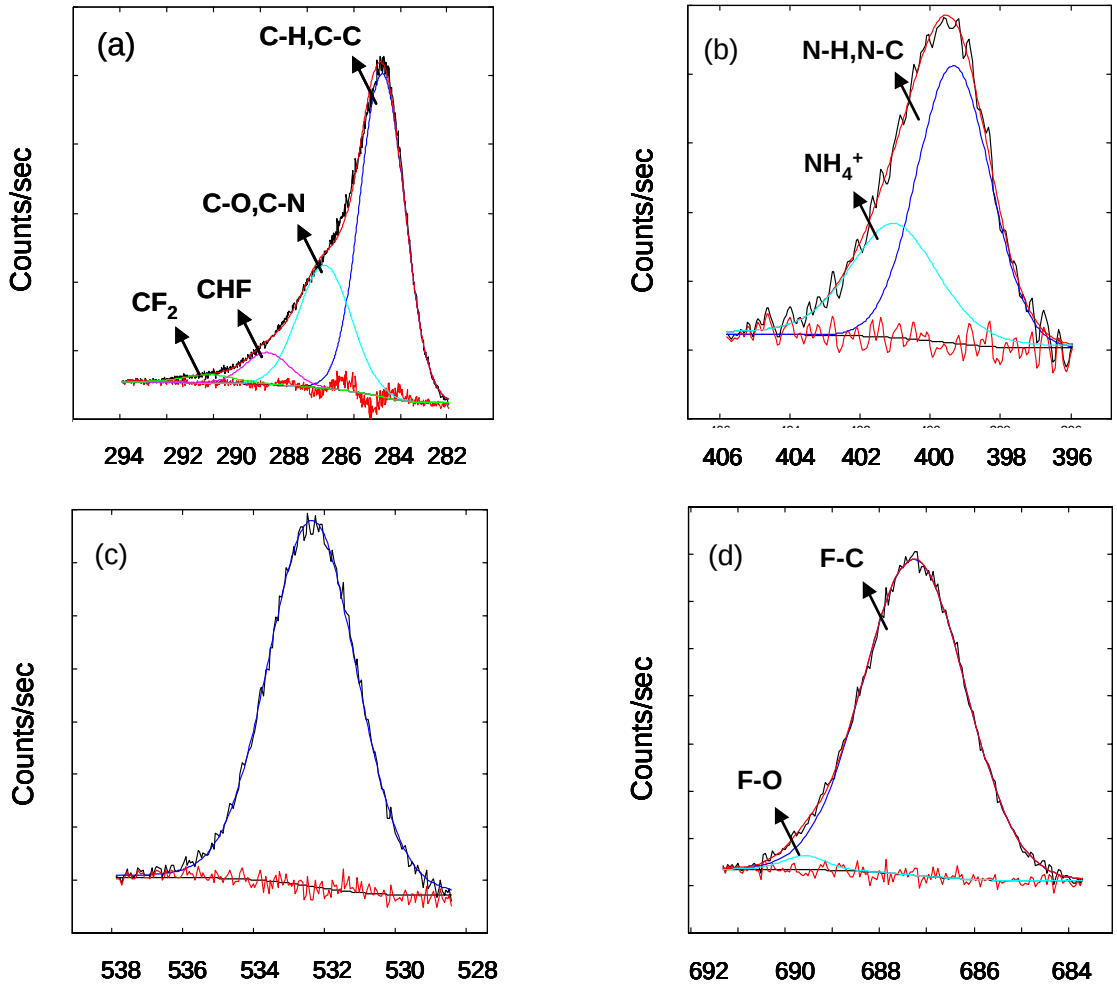

Figure 4.2. Surface bonding structure of the etch residue from XPS peak deconvolution of (a) carbon (b) nitrogen (c) oxygen and (d) fluorine atoms.

range from 9-11 depending on the extent of deprotonation [150] whereas the pKa of methacrylic acid (acidic moiety in 193 nm resist) is 5.7 [151]. Hence 193 nm resists can dissolve in weakly basic solutions as opposed to 248 nm resists. Also, ketones such as acetone and ethyl lactate are good solvents for acrylate based 193 nm resists but not for PHOST based 248 nm resists.

The attenuated total reflection - Fourier transform infrared (ATR-FTIR) spectroscopy technique was used to obtain vibrational spectra of photoresist residues. The spectra were collected with a Golden Gate ATR accessory from Graseby-Specac. Transmission FTIR spectra were difficult to interpret because of interference from various films in the stack and signal loss from the thick substrate. The spectrum from the etch residue sample was compared to a 248 nm resist and a 193 nm resist. The 248nm resist is based on poly 4-hydroxystyrene (Figure 4.3A) backbone and the specific structure is shown in Figure 4.3B. It is partially protected with a tertiary butoxy carbonyl (tBOC) group which is removed upon exposure to the 248 nm radiation causing a switch in the solubility of the resin in an aqueous base. The 193 nm resist is AZ1020P, a commercial system from Clariant. According to the vendor, AZ1020P is an acrylate based resist. An example of an acrylate based resist (AZ1010P) is shown in Figure 4.3C; this material consists of methacrylate backbone with 2-methyl-2-adamantyl and mevalonic lactone protecting groups [152].

Since the thickness of the photoresist residue (~400 nm) was less than the attenuation length of the infrared radiation, characteristic peaks from the capping layer and the CORAL™ dielectric appear in the spectrum. Broad peaks corresponding to Si-O-Si stretch (1010 cm^{-1}) and Si-C rocking vibration (~765 cm^{-1}) from Si-$(CH_3)_x$ moieties overlap peaks in the spectrum from the photoresist residue [128]. Hence, vibrational spectra in the wavenumber range between 4000 cm^{-1} and 1400 cm^{-1} were used to compare the photoresists; spectra are shown in Figure 4.4. The resists containing PHOST show characteristic absorptions of an aromatic ring such as ring C-C stretch at 1500 cm^{-1}, out-of-plane C-H deformation vibration (~820 cm^{-1}) and aromatic C-H stretching

A

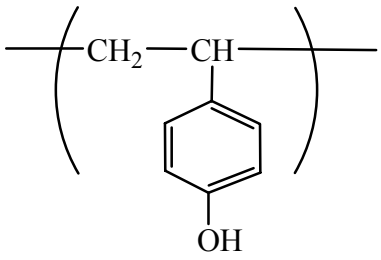

B

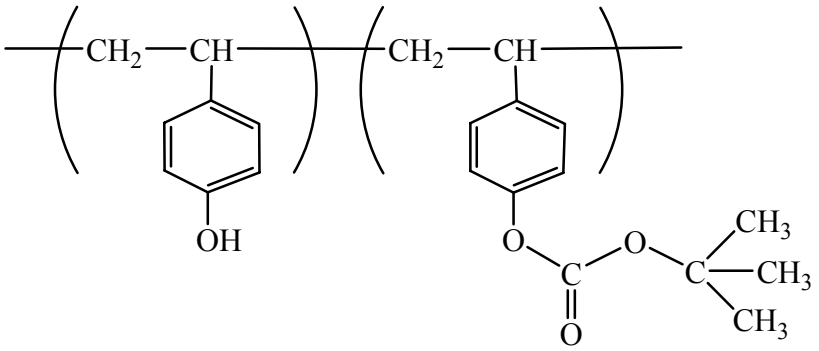

C

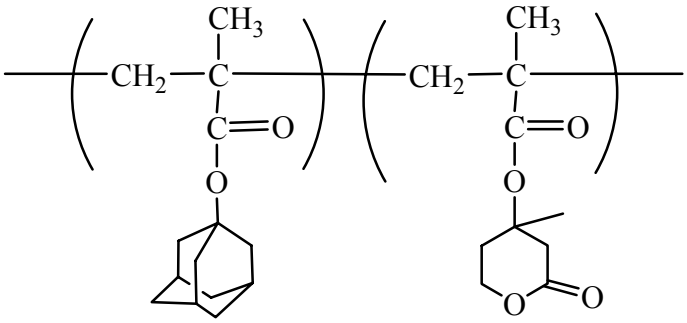

Figure 4.3. Structure of (A) poly 4-hydroxystyrene (PHOST) (B) PHOST partially protected with tert-butoxy carbonyl (C) AZ1010P, an example of a commercial 193 nm photoresist.

vibrations (~3030 cm^{-1}). These peaks are absent in spectrum 4.4(iv) from the 193 nm resist which does not contain any aromatic rings. In addition, films with protecting groups (photoresist residue, PHOST-tBOC and AZ1020P) have strong C=O stretching

vibration peaks at ~1700 cm^{-1}. PHOST also has a small C=O peak probably from the residual solvent (propylene glycol monomethyl ether acetate, PGMEA) in the films. The negative absorption at 2340 cm^{-1} (O=C=O asymmetric stretching vibration) in some of the spectra is due to interference from CO_2 in the atmosphere. In fact, the spectrum of the etch residue is very similar to the spectrum of PHOST-tBOC suggesting that the etch residue has a 248 nm resist based on a PHOST-tBOC backbone. The relative intensities of the absorption peaks corresponding to the C=O stretch and the aromatic ring stretch probably differ because of the different extent of OH group protection. The PHOST-tBOC resin used in this study was 26.4% protected (i.e., 26.4% of all the phenol groups were protected by the tBOC group). In addition, state-of-the-art commercial 248 nm resists have t-butyl acrylate groups (which contribute to C=O absorption) copolymerized with hydroxystyrene groups to provide additional stability against deprotection from small quantities of weak bases such as amines that are present in the fab environment. These resists are known as environmentally stable chemical amplification positive (or ESCAP) photoresists. The higher peak intensity from an alkyl C-H stretch (~2920 cm^{-1}) also supports the hypothesis that an ESCAP type resist has been used to generate these samples.

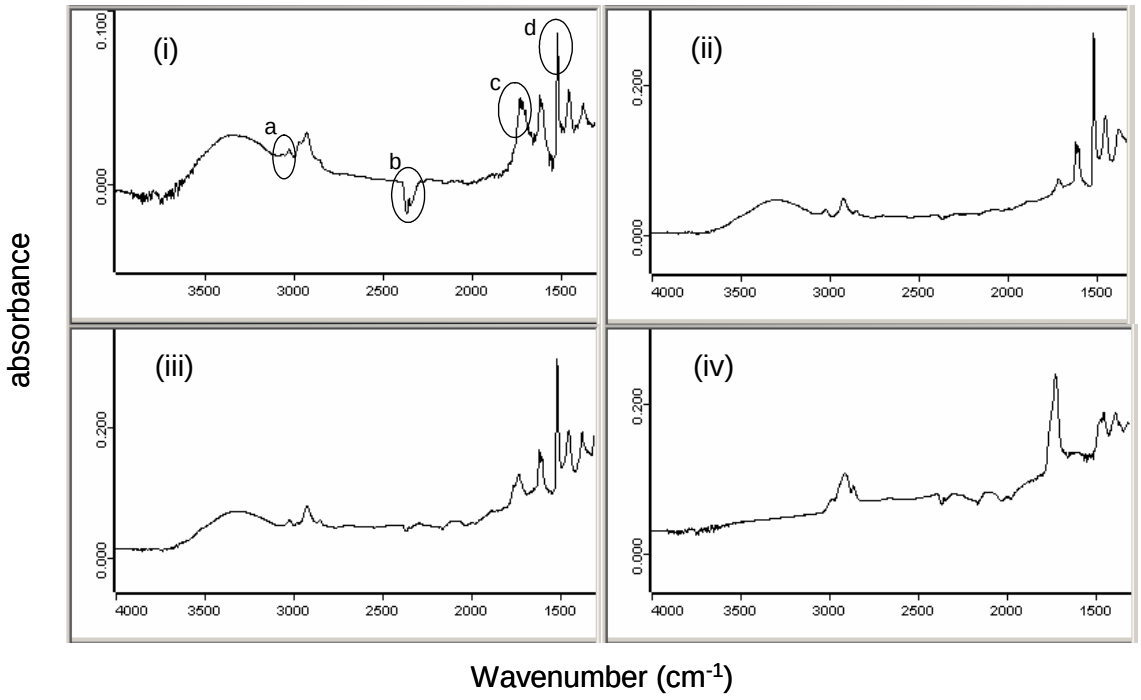

Figure 4.4. ATR-FTIR spectra of (i) photoresist residue, (ii) PHOST, (iii) PHOST-tBOC, and (iv) AZ1020P showing characteristic peaks (a) aromatic C-H stretch, (c) C=O stretch, (d) ring C-C stretch; the negative absorption in CO_2 asymmetric stretching peak (b) is an experimental artifact.

4.2.3 Estimation of the fluorocarbon residue thickness

The thickness of the fluorocarbon layer deposited on the film material being etched is generally estimated from ellipsometry and angle-resolved XPS. This thickness usually ranges between 1 and 3 nm on SiO_2 and ~5 nm on Si for a C_4F_8 based etch chemistry [49]. However, few reports have been published on the thickness of the residue formed on photoresist or of the sidewall polymer due to limitations of the above mentioned analytical techniques. Since there is no well defined transition between the fluorocarbon residue and the hydrocarbon photoresist underneath, accurately modeling the residue to analyze the ellipsometry data is difficult. Doemling et al. have measured

the fluorocarbon thickness using the XPS 'overlayer' approach [43] – the thickness of the fluorocarbon layer was estimated by comparing the intensities of oxygen at two different angles. It was assumed that oxygen was present only in the photoresist underneath the fluorocarbon residue and the oxygen signal decay was related to the thickness of the fluorocarbon overlayer. For the case of a CHF_3 plasma, the estimated thickness was <1 nm on novolak resist (used for 365 nm lithography). However, the residue may contain some oxygen released by the erosion of the photoresist in the etch atmosphere. In addition, quenching of free radicals on the photoresist surface when exposed to atmospheric conditions also contributes to oxygen on the surface. Thus, neglecting these contributions could lead to an under estimation of the overlayer (fluorocarbon) thickness. Moreover, the range of fluorine penetration into the film may be more than the thickness of the fluorocarbon film on the surface (Figure 4.5).

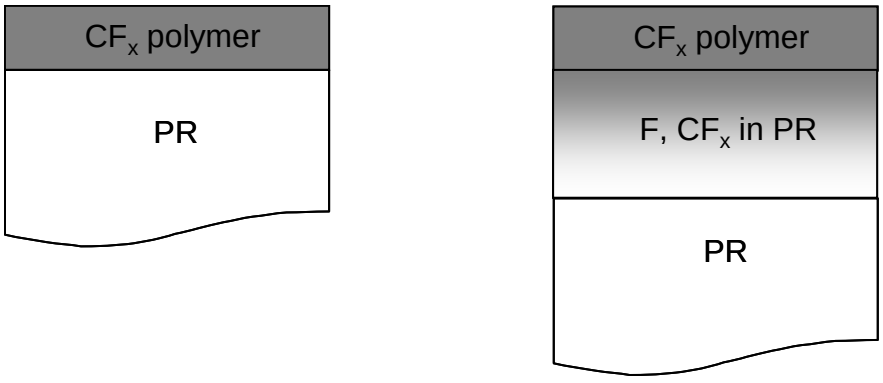

Figure 4.5. Illustration of the photoresist residue from Doemling et al. [43] (left) and from this work (right). Dimensions are not to scale.

In this work, the extent of fluorine penetration into the photoresist residue was estimated. Due to diffusion of the fluorine species by both concentration gradients and electric field across the photoresist, the fluorine containing species are found at depths below the fluorocarbon polymer on the surface. These species may or may not be covalently bonded to the photoresist polymer. However, the presence of these species affects solvent diffusion and the dissolution behavior of the unmodified resist. Hence, it is important to know the depth of fluorine incorporation.

The angle-resolved XPS technique (described in section 3.3) is unable to supply complete depth information when the thickness of the overlayer is greater than the probing depth of the instrument (2-3 times the electron attenuation length). In addition, knowledge of the bulk photoresist composition is necessary to model the residue as a simple overlayer on photoresist in order to extract the fluorocarbon thickness. Beam based techniques such as SIMS and RBS are not appropriate for such 'soft' films because of concerns of film damage or modification due to high energy ion bombardment.

In this work, a low-energy argon ion beam was used to sputter the sample while monitoring the composition by XPS. XPS sputter depth profiling has been used extensively to study interfaces and thin inorganic films [153, 154] [120]. For the following analyses, the sample was sputtered until fluorine was no longer detected; the crater formed as a result of the sputtering process was then profiled to estimate the thickness of fluorine incorporation into the photoresist. However, there are two primary concerns with this approach – 'knocking-in' of the atoms by the bombarding ions (also known as 'atom mixing') and preferential sputtering. Low ion energies were used to sputter the sample in an attempt to mitigate the knock-in effects [153]; the ion energies

used were 1 kV, 1.5 kV, 2 kV, 2.5 kV, 3 kV. A differential ion gun (Physical Electronics, model 04-303A) was used to sputter the samples inside the XPS chamber with the x-ray source isolated. The ion gun is differentially pumped from the main chamber by a turbomolecular pump to 15×10^{-3} Pa (1.1×10^{-4} Torr). The ion gun was aligned so that its focal point coincided with the point where the x-ray beam hits the sample. The emission current was maintained at 25 mA and the beam was rastered over an area of 2mm×2mm. This area is larger than the x-ray beam size (0.8 mm diameter) and thus only the center of the crater (with more sputter uniformity than the edges) was analyzed. After sputtering, a profilometer (KLA-Tencor, Alpha-Step) was used to scan over the sample to probe the surface morphology and measure the sputtered depth.

The sputter rate of the etch residue at various ion energies used in this study is shown in Figure 4.6. To calculate the approximate sputter rate, uniform sputtering was assumed at all ion energies. The sputter rate is a function of the raster size, emission current and the extent of beam focus; these parameters were kept constant during all experiments. As the energy of the ion increases above a threshold energy, the etch rate rises rapidly. The microroughness (from atomic force microscopy) in the crater changes only slightly from 1.3 nm for the original sample to 1.58 nm for a sample sputtered at 3 kV indicating little preferential sputtering. If the ion energies were increased monotonically, ion implantation would eventually occur leading to a reduction in sputter rate.

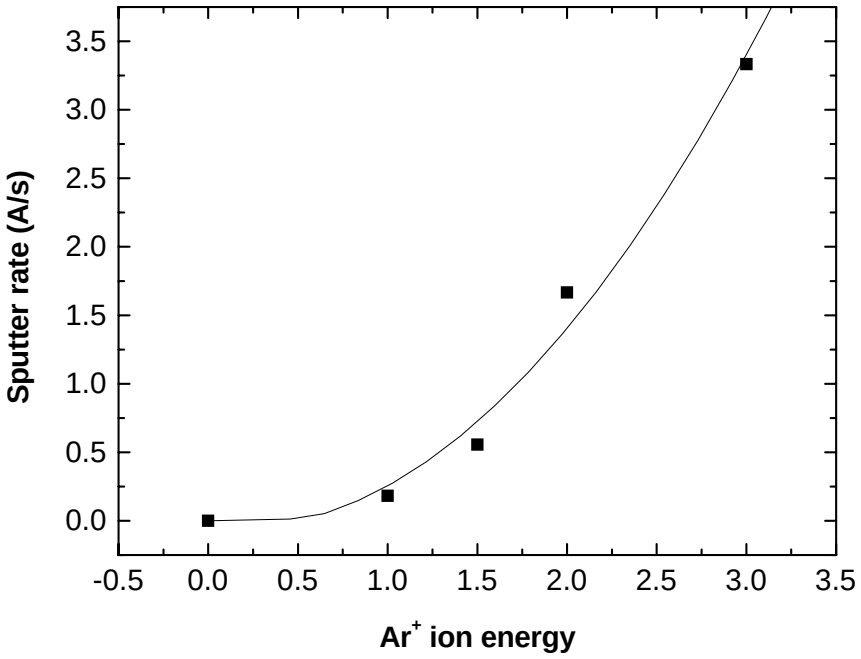

Figure 4.6. Sputter removal rate of photoresist residue as function of Ar^+ ion energy.

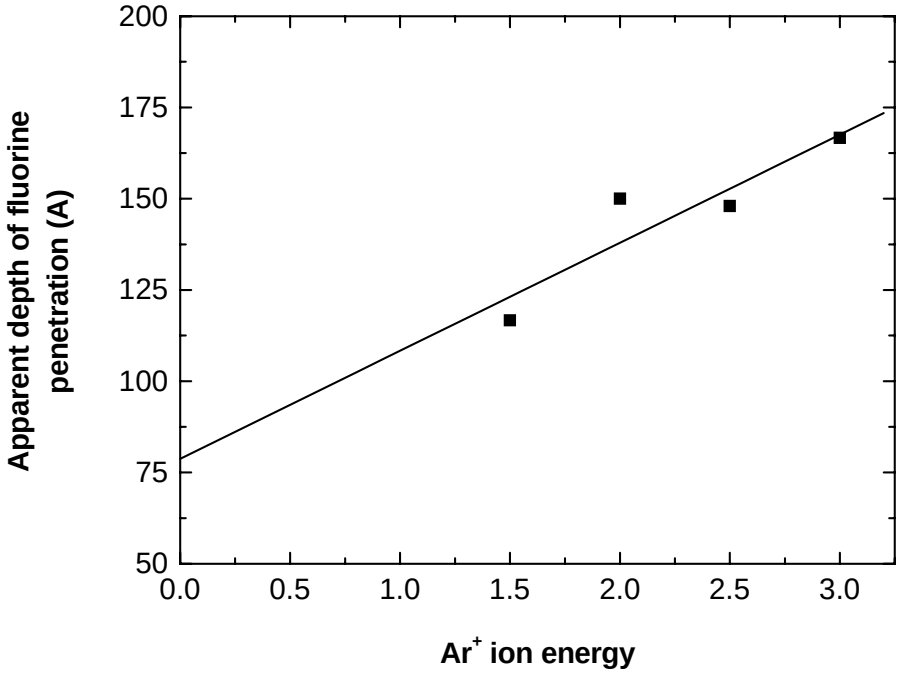

Figure 4.7. The depth of fluorine penetration in photoresist residue measured at different ion energies.

Based on these sputter rates, the depth of penetration of fluorine was measured at different ion energies. As shown in Figure 4.7, the apparent depth of penetration increases with ion energy because higher energies knock fluorine atoms (or small fluorine containing molecular species) into the film. Therefore, the measured values more closely approximate the actual depth of fluorine incorporation at low ion energies. By linear extrapolation of the apparent depth of fluorine incorporation to zero ion energy, the approximate thickness of the fluorocarbon residue on these samples was estimated to be 7.8 nm.

4.3 Deposition of model films

4.3.1 Photoresist thin films

The patterned film samples are not particularly suitable for fundamental studies directed toward an understanding of how etch residues form and how they interact with cleaning solutions. Hence, blanket model films were deposited to simulate the etch residues. In addition, blanket photoresist films were also deposited to perform mechanistic studies. Three different photoresist films were investigated in this study: a PHOST resin (the basis for 248 nm photoresists), a partially protected PHOST resin (tert-butoxy carbonyl protecting group) and a commercial 193 nm photoresist (AZ1020P, Clariant). Thin films of these resists were spin cast (Cee™ 100CB, Brewer Science) on 4″ Si wafers; the wafers were then soft baked to remove the casting solvent (PGMEA for PHOST and PHOST-tBOC, ethyl lactate for AZ1020P). The average thicknesses and the Cauchy parameters estimated from ellipsometry are shown in Table 4.2. Normally, 193

nm resist films are thinner than 248 nm resists, because they have a smaller depth of focus. These two classes of resists encompass most of the photoresists used currently as well as those expected to be used in near future (2010) [24].

Table 4.2. Thicknesses and Cauchy parameters of the resins used in this work along with soft bake conditions.

Resist	Bake condition	Cauchy parameters	Thickness (nm)
PHOST	2min @ 115^{o}C	(1.58,0.00728,0.000389)	1340
PHOST-TBOC	2min @ 115^{o}C	(1.56,0.00696,0.000342)	1050
AZ1020P	1min @ 115^{o}C	(1.508,0.00381,0.000116)	640

4.3.2 Model photoresist residues

Blanket wafers of the above photoresist films were exposed to etch plasmas to modify the surface and deposit fluorocarbon residue. These exposures were performed in both a reactive ion etcher (RIE) and an inductively coupled plasma etcher (ICP). The etch chemistry used was $Ar/C_4F_8/O_2$ which is commonly used to etch SiO_2 [32] and low-*k* dielectrics [49]. The goal was to modify the photoresist to simulate IC manufacturing etch residues without actually etching the substrate. In addition to the surface atomic

composition from XPS, the extent of cross-linking on the surface is also monitored. The cross-linking of these photoresist residues is estimated from the fraction of carbon atoms bonded to two or more carbon atoms. Thus, terminal groups such as CF_3 do not contribute to cross-linking of the residue.

Plasma parameters such as gas flow rate, treatment time, plasma power, bias power (in the case of ICP) were varied to obtain residues with appropriate properties. Shown in Table 4.3 are the results from exposure of PHOST films to fluorocarbon etch plasmas (PlasmaTherm RIE) as a function of the above plasma parameters. In all cases, 4″ wafers with spincast PHOST films were placed on the 6″ powered electrode of the RIE before reducing the system pressure to 50 mTorr. The etch gases were allowed to flow through the reactor system for 2 minutes before turning on the RF power. After exposing the wafer to the etch atmosphere for the desired time, the chamber was evacuated and purged with N_2 for 10 minutes. During the plasma exposure, the substrate temperatures and the chamber pressure remained at 40 ^{o}C and 50 mTorr respectively. The samples were then analyzed by XPS for surface atomic composition and bonding structure. Finally, the resulting films were evaluated for solvent resistance by immersing them in methanol. The patterned etch residue samples were resistant to common solvents such as methanol or N-methyl-2-pyrrolidone (NMP). All films deposited on PHOST at lower power (200 W, RIE-1 through 4) dissolved completely in methanol at room temperature. Films exposed to the etch plasmas at 360 W partly dissolved and partly lifted off the substrate when immersed in methanol. Such results indicate cross-linking of the resist and the fluorocarbon residue at higher powers, thereby forming a ‘crust’ on the

Table 4.3. Effect of plasma parameters (power, time, gas flows) on residue formation in $Ar/C_4F_8/O_2$ etch plasma.

Expt	Substrate	Power (W)	Time (min)	Gas flow rates sccm (C_4F_8,O_2,Ar)	Atomic composition %(C, O, F)	Comments
RIE-1	PHOST	200	1	(12,6,75)	(52,9,39)	No crust
RIE-2	PHOST	200	2	(12,6,75)	(52,8,40)	No crust
RIE-3	PHOST	200	5	(12,6,75)	(51,9,40)	No crust
RIE-4	PHOST	200	2	(30,6,75)	(53,7,39)	No crust
RIE-5	PHOST	360	2	(12,6,75)	(53,9,38)	Crust present
RIE-6	PHOST	360	5	(12,6,75)	(54,8,38)	Crust present
RIE-7	PHOST	360	5	(6,3,75)	(53,8,39)	Crust present
RIE-8	PHOST/ SiO_2	360	5	(12,6,75)	(59,9,32)	Crust present
RIE-9	PHOST-tBOC	360	5	(12,6,75)	(54,8,38)	Crust present
RIE-10	AZ1020P	360	2	(12,6,75)	(52,9,39)	Doesn't dissolve

surface. In RIE, higher power means higher ion energies and/or higher plasma density. Even in the presence of this crust, the solvent was able to dissolve the softer (unmodified) resist underneath the crust either by diffusing through it or undercutting it from the sample edges. AZ1020P (which is acrylate based) does not dissolve in methanol (even

without the crust on the surface). However, acetone or NMP dissolves the softer resist and lifts the crust off the sample.

It also appears that changing the gas flows had very little effect on the fluorocarbon surface composition (RIE-2 vs. RIE-4, RIE-6 vs. RIE-7) although the etch rate of the resist changes. Increasing RF power reduces the F% slightly (RIE-2 vs. RIE-5, RIE-3 vs. RIE-6) due to an increased removal of F by increased ion bombardment. Similar observations were made by Oehrlein et al. – the fluorocarbon residue deposited on Si had less fluorine (and was thinner) at higher ion bombardment energy [44]. At low ion energies, the residue was rich in CF_2 groups whereas ion-dominated deposition resulted in predominantly C-CF_x groups. However, in all cases the fluorine% (~38% with F:C ratio~0.7) was much higher than that on the plasma etch residue samples (F~10%, F:C-0.14).

Similar experiments were performed in an ICP reactor (PlasmaTherm ICP) with similar etch gas composition as in the RIE system. In ICP, the substrate bias power was used to control the ion energy independently while the plasma power was used to control the plasma density (extent of dissociation of the etch gases). These treatments were performed at 10 mTorr and 15 ^{o}C substrate temperature using 850 W plasma power and 30 W bias power. With ICP, higher bias power (150 W) was necessary to form a crust on the surface. Due to higher ion bombardment, the resulting films had slightly lower fluorine content (35% with F:C~0.6) than films from the RIE reactor but the fluorine content was still considerably more than that on the patterned etch residues. These observations may be explained by the following:

1. During generation of the patterned etch residue samples, some of the fluorine in the plasma is used to form volatile products – hence there may be a fluorine deficiency near the surface of the wafer leading to a residue with lower fluorine content. This is supported by the decrease in fluorine% on the sample from experiment RIE-8. In this experiment, a SiO_2 wafer partly covered with PHOST was exposed to the etch plasma and surface analysis was performed on the resulting residue close to the interface.

2. The power densities used in the above depositions range from 0.6 W/cm^2 to 1.1 W/cm^2 (for RIE) and are close to the limits set on the tool used in this study. However, much higher power densities may have been used on the patterned etch residue samples. For example, in a recent study on highly selective SiO_2 etching in a dual-frequency RIE system [32], the power density on the bottom electrode was ~3 W/cm^2. This coupled with lower pressures (30 mTorr) result in higher ion bombardment and films with lower F:C ratio (as low as 0.25 on a Si wafer).

3. A fluorine scavenger like H_2 or CO may have been added to the etch mixture for greater etch anisotropy. This leads to depletion of fluorine on the surface residue.

In order to more closely simulate plasma etch residues, a 1 min argon plasma post treatment after exposure to the RIE or ICP etch plasmas was invoked; this sequence produced films with almost identical composition to that of the etch residues. With this procedure, argon ions can remove fluorine through sputtering of low molecular weight fluorocarbon molecules from the surface or by direct sputtering of fluorine from the crust. The carbon 1s peaks from a fluorocarbon residue film before (RIE-5) and after Ar plasma

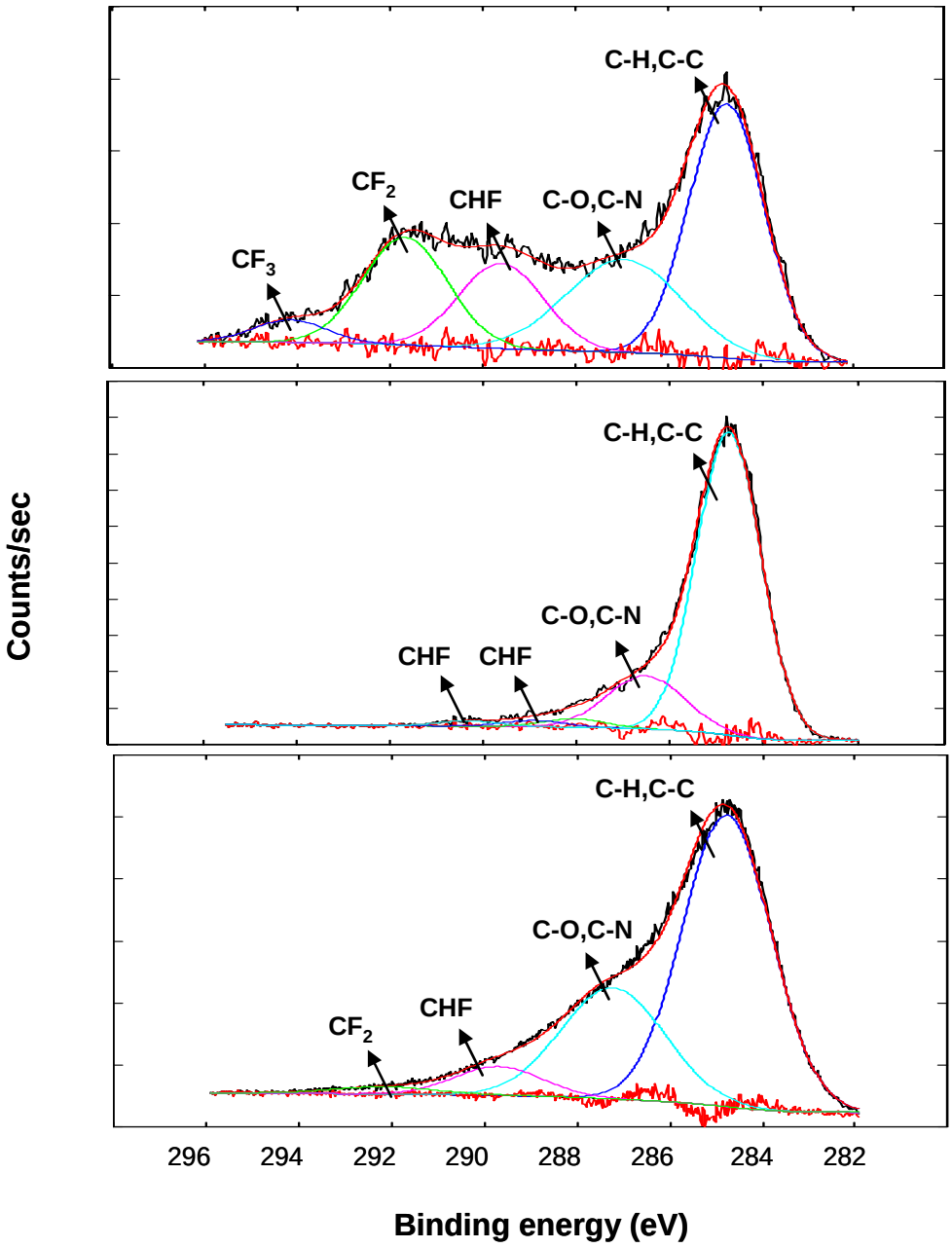

Figure 4.8. XPS C1s peak on fluorocarbon residue on PHOST before (top) and after (middle) Ar plasma post treatment. Also shown for comparison is the C1s peak on the patterned samples (bottom).

post treatment are shown in Figure 4.8 along with the deconvoluted peaks. Also shown is the C1s peak from the patterned etch residue samples showing similar bonding structure on the surface but with more carbon atoms with C-O, C-N, CHF and CF_2 bonding structures.

4.3.3 Model fluorocarbon residues

The fluorocarbon residue on the photoresist or the material being etched is so thin (<10 nm) that detailed chemical analysis or dissolution studies on these residues were impractical. Hence, thicker fluorocarbon films were deposited on Si wafers to serve as model residues. Thick fluorocarbon films have been used in applications such as intermetal dielectric [155] or barrier films. These films are deposited in a parallel plate plasma enhanced chemical vapor deposition (PECVD) system which is functionally different from an RIE system:

1. Higher flow rates and higher pressures are used to increase the deposition rate (versus etch rate). Higher pressures means greater scattering of ions – hence, fewer and lower energy ions strike the growing film surface.

2. The wafer is placed on the grounded electrode (as opposed to powered electrode for RIE mode) – hence, the wafer experiences low energy ion bombardment.

However, high power (1.97 W/cm^2) and substrate temperature (120 ^{o}C) were used to reduce deposition of low molecular fragments and promote cross-linking of the deposited films. Typical deposition conditions were: C_4F_8-30 sccm, O_2-6 sccm, Ar-120

sccm, substrate temperature-120 ^{o}C, power-300 W, pressure-0.79 Torr. Under these conditions, the deposition rate of the fluorocarbon film was 2.1±0.5 nm/s. From XPS analysis, the surface atomic composition of the film was C-48±1%, O-1%, F-51±1%. The Cls peak from this film is compared to that from patterned etch residue sample in Figure 4.9.

The model residue on PHOST (e.g. RIE-5) shows higher % carbon and oxygen compared to these films because the carbon and oxygen atoms from the PHOST also contribute to the photoelectron signal. These fluorocarbon films were chemically resistant to methanol or NMP even at elevated temperatures. These model films (photoresist residues and blanket fluorocarbon films) were then exposed to cleaning mixtures to investigate the diffusion of chemical species and the ensuing chemical modification.

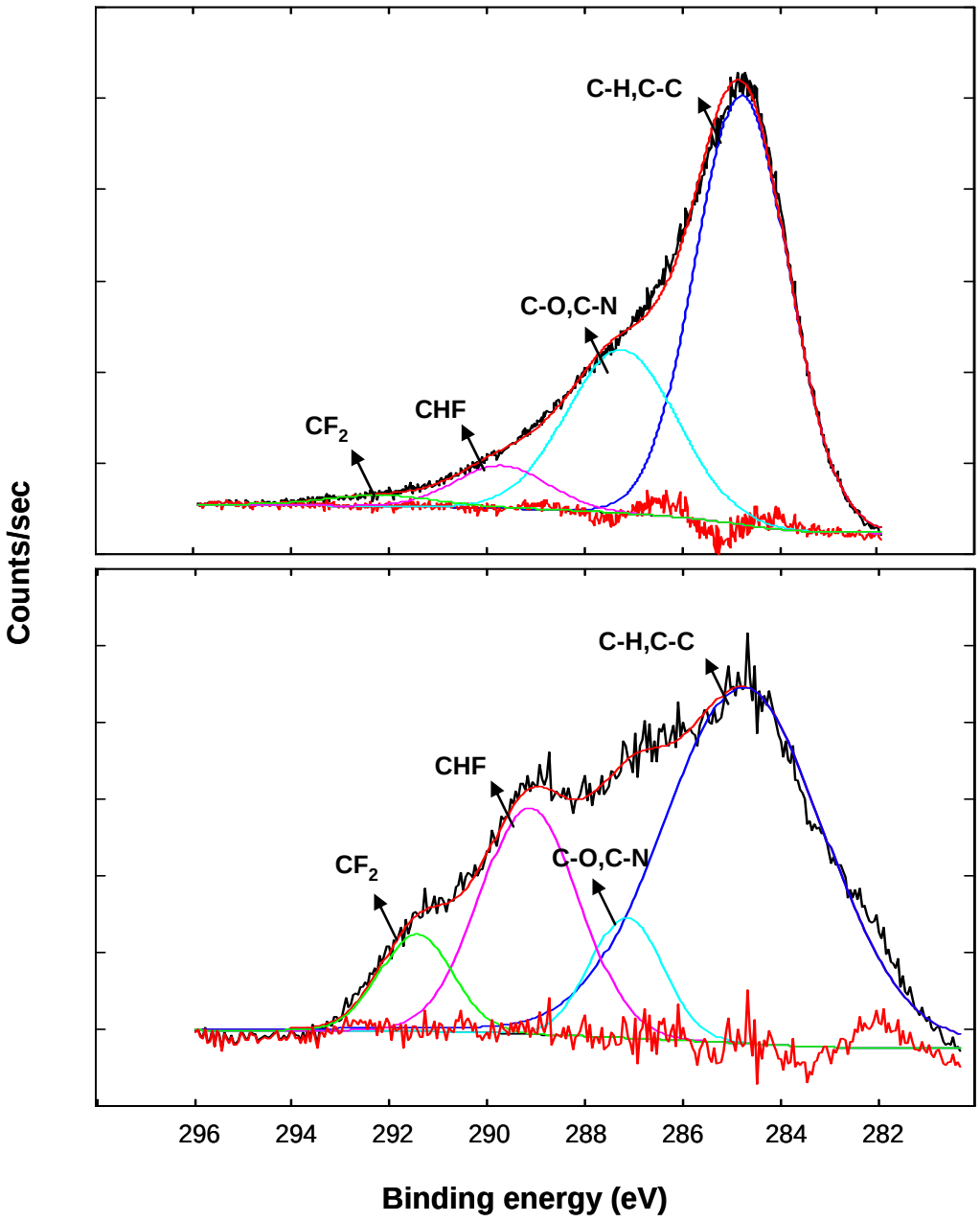

Figure 4.9. XPS C1s peak on patterned etch residue sample (top) and model PECVD fluorocarbon film (bottom).

CHAPTER 5

FORMULATION OF CO_2 BASED CLEANING MIXTURES FOR RESIDUE REMOVAL

5.1 Introduction

In this chapter, appropriate additives to CO_2 are identified that can remove post plasma etch residues. Solvents that can remove the residues in the liquid phase (beaker) can potentially be used as additives to CO_2. Hence, various classes of additives were tested for their ability to remove the residues in the liquid phase: organic solvents, aqueous salt solutions, acids and bases. Based on these beaker studies, high pressure CO_2 based mixtures were developed for post plasma etch residue removal. The chemical interactions between CO_2 and the additives and their effect on residue removal were also investigated.

5.2 Initial beaker studies

5.2.1 Correlation between XPS and SEM

The test samples were first treated in liquid solvents in a beaker to identify potential additives to CO_2. Solvents were chosen based on similar studies in the literature and the chemical nature of the photoresist present in the residue. Unless mentioned otherwise, all solvents were purchased from Sigma-Aldrich. The treatments were

performed in an Erlenmeyer flask at elevated temperatures to improve residue solubility. Treatment times ranged from 30-60 min. Following treatment, the extent of residue removal was evaluated from x-ray photoelectron spectroscopic (XPS) studies of the surfaces. Cross sectional scanning electron micrographs (SEM) of the samples were also taken to evaluate the sidewall residue removal and to ensure that the underlying dielectric was not attacked. XPS may not detect changes in bonding structure of the dielectric because of the presence of the capping layer (SiO_2) on top of the dielectric stack. An alternative way to evaluate the compatibility is to expose a blanket dielectric layer to the cleaning solution and monitor the surface composition. Cross-sectional SEM was also used to obtain a correlation between the XPS atomic% and the extent of residue removal. Shown in Figure 5.1 is a comparison of XPS surface composition and the amount of residue present on the sample as observed by SEM. The samples were partially clean after treating them in an ammonium hydroxide and hydrogen peroxide (APM) mixture at 60 ^{o}C for 2 min. APM is commonly used in front-end-of-line (FEOL) integrated circuit (IC) processing to remove organic residues [156]. For an untreated sample, the carbon and fluorine atomic concentrations are around 71% and 10% respectively. No silicon is detected from the capping layer since the thickness of the residue is greater than the probing depth of the XPS instrument (<10 nm). Since the x-ray beam diameter is 0.8 mm, the composition obtained from XPS is an average over this area. Hence, in areas that are partially clean (middle figures in Figure 5.1), the carbon atomic% is higher than when the sample is completely clean and the silicon% is lower. A completely clean sample has carbon<5% and silicon>25%. However, due to differences in handling

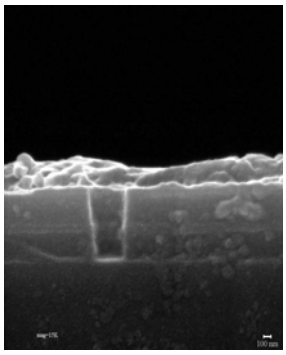

Untreated:

C1s	N1s	O1s	F1s	Si2p
71.3	3.8	15.1	9.8	0

Partially clean:

C1s	N1s	O1s	F1s	Si2p
58.6	3.8	21.8	12.7	3.2

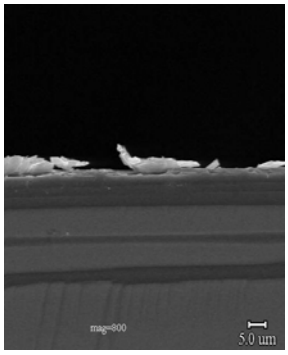

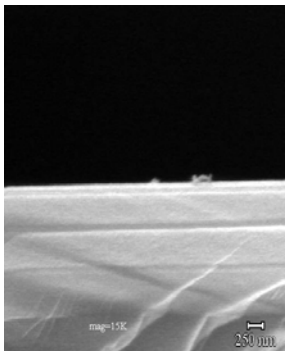

Partially clean:

C1s	N1s	O1s	F1s	Si2p
33.5	2.6	38.3	10.1	15.5

Clean:

C1s	N1s	O1s	F1s	Si2p
5	0	69	0	26

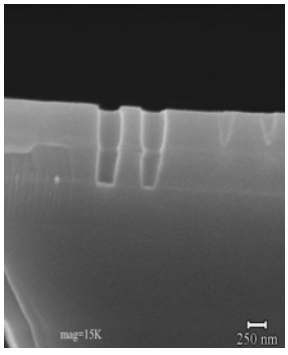

Figure 5.1. Correlation between XPS surface atomic composition and the amount of residue present on the sample.

(residues from rinsing solvents, exposure to atmosphere), the silicon% ranged from 22-26% for samples with no bulk residues observed by SEM. Hence, a sample is considered completely clean if Si>22%.

5.2.2 Photoresist dissolution mechanism

One way of photoresist residue removal is dissolution of the unmodified photoresist underneath thus lifting the fluorocarbon residue off the surface. The photoresist in the etch residue sample has a poly 4-hydroxystyrene (PHOST) based backbone with acrylate groups for enhanced stability against deprotection from exposure to atmosphere [157]. The photoresist can dissolve by simple chain disentanglement in a polar solvent or by a chemical mechanism [158]. During simple dissolution, solvent molecules with an affinity for the polymer diffuse into the polymer, causing it to swell, form a gel layer and dissolve it. If the polymer molecular weight is larger than the disentanglement molecular weight, then the chains have to disentangle before they can dissolve in the solvent [159]. A chemical mechanism (Figure 5.2) is responsible for dissolution of the photoresist during the development step in photolithography. During this process, the phenolic resins are deprotonated by the OH^- ions in the aqueous developer (tetramethylammonium hydroxide, TMAH) [160, 161]. According to the dissolution mechanism proposed by Willson's group, the polymer becomes soluble after a critical fraction of the phenolic groups are deprotonated. When the phenolic group is protected, it does not undergo deprotonation – hence, the solubility of even partially protected PHOST resin is lower than that of the unprotected resin. A third mechanism is possible when the polymer is highly cross-linked or the glass transition temperature T_g is

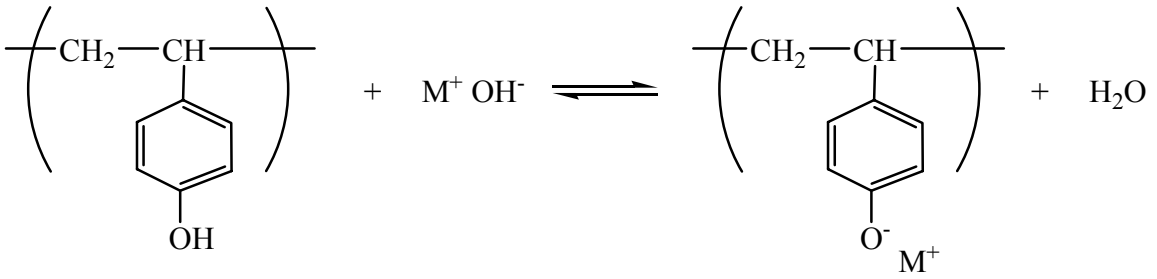

Figure 5.2. Dissolution mechanism of PHOST resin in a base.

much higher than the temperature at which dissolution is performed. In that case, diffusion of the solvent into the polymer causes it to crack due to swelling-induced stress, thereby leading to loss of adhesion to the substrate. This mechanism is possible in these highly cross-linked etch residues.

5.2.3 Organic solvents

Several solvents were tested for their ability to remove the etch residues primarily by dissolving the photoresist underneath. Some of these solvents have been chosen based on previous studies or similar applications where they were used. For example, N-methyl-2-pyrrolidone (NMP) is a component in photoresist removers (or strippers) developed by EKC technology. Propylene carbonate and dimethyl sulfoxide (DMSO) have been used as co-solvents to supercritical CO_2 ($scCO_2$) for photoresist removal [105-107]. Ethyl lactate is a solvent for acrylate based 193 nm photoresists. Glacial acetic acid has been used for the removal of positive photoresists such as poly(methyl

methacrylate) (PMMA) and PHOST [162]. Propylene glycol monomethyl ether acetate (PGMEA) and Methyl isobutyl ketone (MIBK) are commonly used solvents for PHOST and PMMA respectively. Peracetic acid is used as a benign alternative to formaldehyde for disinfecting medical instruments and cleanrooms [163]. Shown in Table 5.1 are the average Si and F atomic percentages from XPS surface analysis. The samples were treated in a beaker for at least 45 minutes at elevated temperatures. The temperatures were lower for volatile solvents (acetone, methanol) and for solvents with explosion hazard when heated (peracetic acid). After treatment, the solvents were rinsed in de-ionized water (DIW) and blown-dry under N_2. The XPS composition reported is an average taken over at least 3 different points on patterned regions of the samples.

From the table, it is clear that none of the solvents were effective in removing the residues completely. Solvents such as acetonitrile and NMP removed the residues in small regions of the sample – hence, the samples showed non-zero Si concentration and F concentrations lower than that of an untreated sample (9.8%). Deviations in F concentration may also be a result of local non uniformities in the untreated etch residue sample, or due to solvent treatment-induced modifications such as cracking of the residue, surface roughening or non uniform residue removal.

The solvents may have had difficulty penetrating the hard crust on the surface of the sample. Hence, some of the promising solvents were evaluated as co-solvents with CO_2 to investigate if enhanced diffusion (with assistance from CO_2 swelling) promotes residue removal. These experiments were performed in the tabletop view cell system described in Chapter 3. The conditions used were: 3000 psi, 70 ^oC, CO_2 flow rate 200 ml/hr, co-solvent flow rate 24 ml/hr, treatment time 45 min. Based on the solubilities

Table 5.1. Etch residue removal using solvents at atmospheric pressure.

Solvent(s)	Time (min)	Temperature (^{o}C)	Avg. Si%	Avg. F%
DI water	45	70	0	7.7
Methanol	45	55	0	8.4
Acetone	60	20	0	11
Propylene carbonate	45	70	0	9
Dimethylsulfoxide (DMSO)	45	70	0	7.4
N-methyl-2-pyrrolidone (NMP)	45	70	0.5	3.9
Acetonitrile	60	55	5.7	3.5
Ethyl lactate	40	70	0	25.5
Glacial acetic acid	60	70	0	7.4
N,N-dimethyl formamide (DMF)	45	70	0	4.8
Tetrahydrofuran (THF)	45	40	0.3	8.3
Peracetic acid (30% in acetic acid)	45	20	0.2	11.5
PGMEA	45	70	0.3	0.5
Methyl isobutyl ketone (MIBK)	60	70	0	1.6

of the solvents in CO_2, there were either two phases (water, propylene carbonate) or a supercritical phase (methanol, acetonitrile, NMP, and glacial acetic acid) during these treatments. After the treatment, samples were rinsed in DIW, blown-dry under N_2 and analyzed by XPS.

Table 5.2. Etch residue removal using high pressure CO_2-solvent mixtures.

Co-solvent	Phase state	Avg. Si%	Avg. F%
DI water	vapor+liquid [164]	0.3	12.5
Methanol	Fluid [165]	0	1.5
Acetone	Fluid	4.5	4.3
Propylene carbonate	Vapor+liquid [166]	3.1	1.3
N-methyl-2-pyrrolidone (NMP)	Fluid	0.2	2.1
Acetonitrile	Fluid [167]	0	4.3
Glacial acetic acid	Fluid [168]	0	7.4

None of the mixtures removed the residue completely even though considerable reduction in surface fluorine concentration was observed. Some of the loosely held fluorinated species on the surface may have dissolved during the high pressure treatment. Samples treated under high pressures also have shown significant cracking on the surface which causes alteration of the surface bonding structure.

5.2.4 Residue removal using bases

From the experiments in section 5.2.3 , it appears that the residue may not be removed simply by dissolution. Thus it is likely that the photoresist might have undergone modification during either pre-etch baking or plasma etching to yield a material that it is no longer soluble in solvents that dissolved the unmodified resist. Hence, an alternative approach to removal was undertaken. Since the photoresist

contains acidic phenol groups, basic solutions should dissolve this material while lifting the fluorocarbon residue from the surface. This expectation was confirmed by treating the samples in solutions of tetrabutylammonium salts with different anions. For example, 0.3 N solutions of chloride, bromide, nitrate, fluoride, and sulfate salts of tetrabutylammonium cation were prepared in acetonitrile; tetrabutylammonium hydroxide was prepared in methanol. Patterned etch residue samples were treated in these solutions for 45 min at 50 ^{o}C and rinsed in acetonitrile solvent. Only the hydroxide and the fluoride salts were effective in removing the residue. The hydroxide may have removed the photoresist by a chemical mechanism while lifting-off the hardened crust. In fact, fragments of crust were removed from the wafer during this treatment. The hydroxide may also enhance residue removal by attacking the interface between the photoresist and the substrate; that is, OH^- ions can attack Si-O bonds between the SiO_2 capping layer and the anti-reflecting coating or PHOST. This mechanism has been demonstrated previously to remove an adhesion promoter (hexamethyldisilazane, HMDS) that was left behind after photoresist was dissolved in alcohols – small amounts of NH_4OH was added to low molecular weight alcohols to enable interfacial attack and residue lift-off [169]. The fluoride salt may be acting in a similar manner through attack of the Si-O interface. In fact, fluorides (HF, NH_4F) are used as SiO_2 etchants in the semiconductor device manufacture [170]. The drawback with this interfacial attack approach (or delamination) is the possibility of damaging dielectrics based on an Si-O backbone (e.g. C-doped SiO_2) unless the procedure is carefully controlled. No damage was observed in samples treated with tetrabutylammonium fluoride ($TBAF.H_2O$) in dry

acetonitrile – however, in the presence of adsorbed moisture in the solvent, the dielectric was significantly damaged at the vias.

The role of pH (OH^- concentration) on residue removal is illustrated in Figure 5.3. Shown in the plot is the average Si concentration on samples treated in solutions with five different pH values (4, 7, 8, 10, 12) at three different temperatures (20 ^oC, 50 ^oC, 70 ^oC). The solutions were aqueous pH standards from Sigma and the pH changes only slightly with temperature (<0.02 per 10 ^oC rise in temperature). Clearly, only the basic solutions (pH>7) removed the residue completely. As the temperature increased, the extent of removal increased indicating that the cleaning mechanism was kinetically

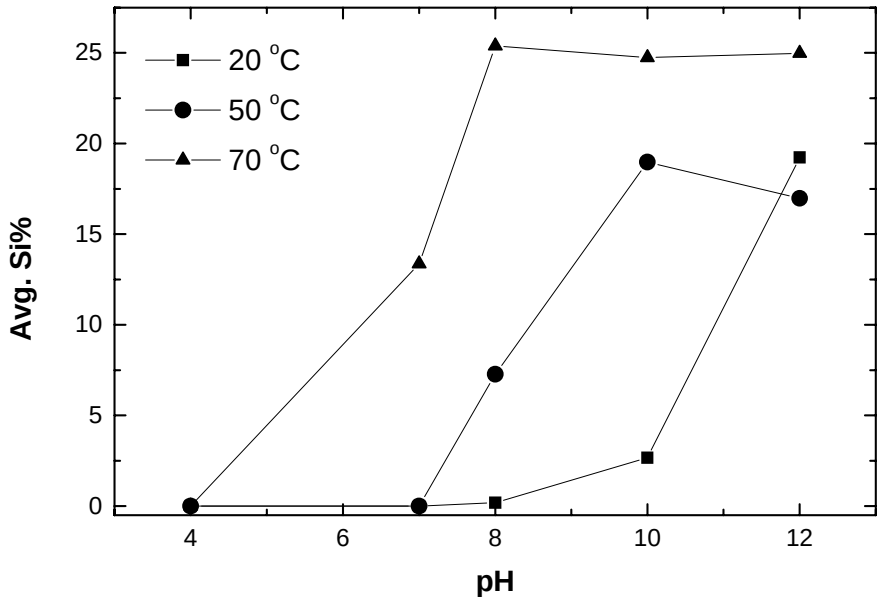

Figure 5.3. Effect of [OH^-] on etch residue removal ability of aqueous solutions.

limited. Even a solution with pH 7 partially removed the residues at 70 ^{o}C. Determination of the factors that kinetically limit residue removal will be discussed in Chapter 7 of this dissertation. Several bases were subsequently explored as possible co-solvents to CO_2 to enable residue removal. Since water has limited solubility in CO_2, bases in non-aqueous solvents were explored. Shown in Table 5.3 are results from beaker experiments using bases for residue removal. Isopropanol (IPA), NH_4OH, DIW mixtures were previously reported to remove ion implanted residues – in those studies, DIW was added to increase the dielectric constant of the medium for greater dissociation of the base [169]. Commercial residue removers and photoresist strippers are based on amines such as 2-(2 amino ethoxy) ethanol, diethylamine, and hydroxylamine. None of these amines were able to remove the residue completely – upon addition of water, however, complete cleaning resulted. In the presence of water, amines dissociate to form OH^- ions (Equation 5.1) which are the primary species responsible for cleaning. This was

$$RNH_2 + H_2O \Leftrightarrow RNH_3^+ + OH^- \tag{5.1}$$

confirmed upon addition of NMP to the amine instead of water – no cleaning was obtained. Temperatures above 45 ^{o}C were necessary for complete residue removal using this amine/water mixture.

Posistrip® EKC830™ is a commercial photoresist remover from EKC technology that consists primarily of 2-(2 amino ethoxy) ethanol and NMP. Unlike a 1:1 mixture of 2-(2 amino ethoxy) ethanol and NMP, this solution was effective in removing the residues even though it has very little water (0.15 wt% as determined by Karl-Fischer

titration [119]). However, commercial photoresist removers such as EKC830™ apparently utilize surfactants that provide enhanced cleaning ability.

Tetramethylammonium hydroxide (TMAH) is widely used as a developer for positive photoresist and an anisotropic etchant for silicon in integrated circuit (IC) and microelectromechanical systems' (MEMS) fabrication [171]. It has replaced KOH for etching of silicon, since potassium ions are detrimental to devices. In addition, TMAH has been used for post CMP cleaning of Si wafers [172]. Most recently, TMAH based mixtures have been investigated as post etch and photoresist residue removers [108]. TMAH is available as a solution in methanol (Aldrich, 334901) and can potentially be

Table 5.3. Etch residue removal using bases.

Solution	Time (min)	Temp (^{o}C)	Avg. Si%	Avg. F%
80:10:10 IPA,NH_4OH,DIW	30	60	25	0.7
2-(2 amino ethoxy) ethanol	45	70	0	0.5
2-(2 amino ethoxy) ethanol+DIW (1:1)	45	70	23	0
2-(2 amino ethoxy) ethanol+NMP (1:1)	45	70	6.2	1
2-(2 amino ethoxy) ethanol+DIW (1:1)	45	45	0	3.3
EKC830™	45	70	24.1	0.4
25% TMAH in methanol	45	55	22.3	2
TMAH in methanol+DIW (4:1)	45	55	25	0

used as a co-solvent to CO_2. When the etch residue sample was treated in TMAH-methanol solution at 55 ^oC, most of the residue was removed (Si~22% and F<2%). Upon addition of water (1 part per 4 parts of solution), complete removal was obtained because of the higher dielectric constant of water relative to methanol. Hence, these mixtures were further investigated in high pressure cleaning studies.

5.3 Reactions between CO_2 and TMAH

Since TMAH is a strong base, it can participate in acid-base reactions with an acidic gas such as CO_2 [173]. These reactions must be considered in order to gain insight into the solubility and cleaning ability of such basic mixtures in CO_2. Although TMAH is used extensively in microelectronics processing, no information is available regarding its interactions with CO_2, the resulting reaction products and the solubilities of these products in common solvents such as water and alcohols. This could be of particular significance in lithography, where atmospheric CO_2 can react with TMAH developer altering its ability to develop photoresist patterns. Analogous reactions have been reported between CO_2 and alkali bases. In an investigation of epoxidation reactions, the addition of aqueous NaOH to a reactor pressurized with CO_2 (40 ^oC, 92 bar) resulted in the formation of $NaHCO_3$ or Na_2CO_3 [174]. In order to formulate cleaning mixtures, the resulting carbonate/bicarbonate salts of TMAH should be soluble in methanol, thereby facilitating addition to CO_2. The solubility of alkaline metal salts in methanol or methanol-water mixtures has also been reported. Specifically, solubility data for $Na_2CO_3/NaHCO_3$ in methanol-water mixtures indicate that only 0.19 wt% Na_2CO_3 is soluble in a methanol-water mixture with a water content of 9.97 wt% [175]. Also, 1.61

g K_2CO_3 is soluble in 100 g of anhydrous methanol at 25 ^oC [176]. In the following paragraphs, the reaction products and the overall reaction mechanism between TMAH and CO_2 are described. The effect of acid-base reactions between TMAH and CO_2 on the cleaning efficiency of post plasma etch photoresist residues is also presented.

The reaction between TMAH and CO_2 was initiated by bubbling CO_2 gas through TMAH in methanol (25 wt%) solution in an Erlenmeyer flask. The concentrations of TMAH, tetramethylammonium carbonate (TMA_2CO_3), and tetramethylammonium bicarbonate ($TMAHCO_3$) were determined by HCl titration. Titrimetric analysis was also performed on carbonate/hydroxide mixtures to determine the individual concentrations and the procedure is described in Chapter 3 [119]. The equivalence point was determined by a graphical method using pH measured using a Corning glass electrode. pH indicators were also used to visually determine the equivalence points – Phenolphthalein (pKa 9.2) for carbonate/hydroxide mixture and Bromocresol green (pKa 4.7) for bicarbonate solution. Stripping of photoresist and plasma etch residues at atmospheric pressure was performed in a closed beaker. The cleaning efficiency of these treatments was determined by XPS analysis.

TMAH is a strong base that readily absorbs CO_2 from air. This CO_2 absorption changes the concentration of base with time – hence, fresh TMAH solution was used when performing these comparison studies. In fact, titration of a week old as-purchased solution of 25 wt% TMAH in methanol revealed that only 86.55 ± 0.66 mole% of TMA^+ existed as hydroxide and 13.45 ± 2.29 mole% as the carbonate salt. The initial product of the TMAH reaction with CO_2 is $TMAHCO_3$ (Equation 5.2). However, in the presence of

excess hydroxide, this intermediate product further reacts with hydroxide and shifts the equilibrium toward formation of TMA_2CO_3 (Equation 5.3). No more than two of these three components co-exist in appreciable amount in any solution because an acid-base reaction eliminates the third.

$$(CH_3)_4NOH + CO_2 \Leftrightarrow (CH_3)_4HCO_3 \tag{5.2}$$

$$(CH_3)_4HCO_3 + (CH_3)_4NOH \Leftrightarrow \left[(CH_3)_4N\right]_2CO_3 + H_2O \tag{5.3}$$

During bubbling, the temperature of the solution (10 ml in volume) increased by ~9 ^oC due to the exothermic nature of the acid-base reaction. Titration of this solution revealed that the concentration of TMA^+ existing as a carbonate increased to 80.41 ± 0.4 mole%. Formation of a white precipitate during bubbling indicated that $(TMA)_2CO_3$ has limited solubility in methanol. After the precipitate settled to the bottom of the beaker, a few ml of the solution above the precipitate was sampled - titration of this filtrate revealed that 24.64 ± 2.41 mole% $(TMA)_2CO_3$ was soluble in methanol. The higher solubility of $(TMA)_2CO_3$ relative to the carbonates of alkaline metals in methanol is probably due to the presence of alkyl groups.

Continued bubbling of CO_2 into the carbonate/hydroxide mixture resulted in complete dissolution of the precipitate and formation of a homogeneous, clear solution. These observations are consistent with the procedure described for regeneration of TMAH in a US patent [173]. According to the patent, when excessive CO_2 is bubbled through aqueous TMAH solutions, formation of $TMAHCO_3$ and precipitation of impurities result – TMAH can then be electrochemically regenerated from $TMAHCO_3$.

Indeed, titration of the above clear solution confirmed that all TMA^+ ions exist as $TMAHCO_3$. The overall reaction can thus be simplified as:

$$(CH_3)_4NOH + CO_2 \rightarrow (CH_3)_4HCO_3 \quad (5.4)$$

The absence of a precipitate indicates higher solubility of $TMAHCO_3$ in methanol relative to $(TMA)_2CO_3$. These observations differ substantially from the results reported previously where analogous bicarbonate salts of alkaline metals had little solubility in methanol [175, 176]. However, addition of water to the $(TMA)_2CO_3$/TMAH mixture resulted in complete dissolution of the precipitate. In these experiments, the original solution of TMAH had ~5 wt% water; the water content was determined by Karl-Fisher titration using Aquamicron AX and Aquamicron CXU reagents (Mitsubishi) [119].

In order to probe the effect of acid-base reactions between TMAH and CO_2 on photoresist residue removal efficiency at atmospheric pressure, 10 mL of the original TMAH solution was bubbled with CO_2 gas for different times. Shown in Table 5.4 is the composition and the comparative cleaning ability of these mixtures. The original TMAH solution (without CO_2 bubbling) has ~86.55 mol% TMA^+ ions in the form of TMAH. The average Si and F content determined by XPS indicates that $(TMA)_2CO_3$ and $TMAHCO_3$ also removed the residues completely. While the TMAH/$(TMA)_2CO_2$ mixtures removed the residues in less than 30 min, the $TMAHCO_3$ needed at least 30 min for complete residue removal. The pH of $TMAHCO_3$ (diluted in DIW) at 20 ^oC is 8.38 while the pH of TMAH/$(TMA)_2CO_3$ mixtures was greater than 12. Longer times were necessary to remove the residues using $TMAHCO_3$ because of the lower concentration of the OH^- ions which are responsible for the residue removal.

Table 5.4. Residue removal in carbonate and bicarbonate salts of TMAH in methanol.

Cleaning solution	Avg. F%	Avg. Si%
TMAH (86.55 mol%) + TMA_2CO_3	0	25.7
TMAH (41.75 mol%) + TMA_2CO_3	0	26.9
TMAH (19.59 mol%) + TMA_2CO_3	0	26.3
$TMAHCO_3$	0	26.5

5.4 High pressure cleaning experiments

After $TMAHCO_3$ in methanol was identified as a potential co-solvent to CO_2, high pressure cleaning experiments were performed. $TMAHCO_3$ was formed by bubbling CO_2 until the TMAH solution was clear; achievement of complete conversion to $TMAHCO_3$ was confirmed by titration. Complete residue removal was obtained under the following conditions: 3000 psi, 70 ^oC, 45 min, CO_2 flow rate 200 ml/hr, co-solvent (2.37 M $TMAHCO_3$ in methanol) 24 ml/hr, followed by a sample wash step in methanol. After treatment, the reactor system was purged with CO_2 for 30 min to remove residual chemicals. The samples were rinsed in DIW, blown-dry under N_2 and the surface atomic composition analyzed.

Next, a matrix of experiments was performed using various mixtures of TMAH, $TMAHCO_3$, methanol and water as co-solvents to CO_2. These experiments were performed while the cell was equipped with a sapphire window to allow *in-situ*

observation of the cleaning process and the phase state of the mixtures. The volume flow rates, temperature and pressure were kept constant. TMAH was also investigated to observe if *in-situ* formation of $TMAHCO_3$ can be employed. The phase behavior and solubility of some of these mixtures (involving TMA^+ salts) in CO_2 was unknown at that point. However, the phase state of these mixtures as observed with a borescope was noted. The average Si% from XPS is summarized in Table 5.5. As expected, complete residue removal was obtained only when the sample was exposed to $TMAHCO_3$. However, no cleaning occurred when TMAH in methanol was added to CO_2 instead of $TMAHCO_3$ in methanol. This can be explained based on the observations described in the previous section when CO_2 was bubbled through TMAH-methanol solution. When TMAH is exposed to CO_2, it reacts to form TMA_2CO_3; since TMA_2CO_3 is not soluble in

Table 5.5. Residue removal in high pressure with CO_2 as the primary solvent.

Co-solvent	Phase state	Avg. Si%
None	Fluid	0
Methanol	Fluid	0
DI water	vapor+liquid [164]	0
Methanol + DI water	vapor+liquid [177]	0
25 wt% TMAH in methanol	vapor+liquid+solid?	0
4:1 vol. mixture of 25 wt% TMAH in Methanol and DI water	vapor+liquid?	26.5
$TMAHCO_3$	vapor+liquid?	25.5

methanol, the carbonate precipitates out of the solution. In fact, a significant amount of salt coated the walls of the cell and the tubing after this experiment. Upon addition of water, however, TMA_2CO_3 dissolves in methanol-water mixture and some of it is carried by CO_2 into the sample cell. Hence, complete residue removal was obtained. When $TMAHCO_3$ (formed *ex-situ*) was added to CO_2, complete residue removal was obtained. No additional water was necessary which is beneficial for water conservation; it is also advantageous to avoid water, since $scCO_2$ can be used to dry the sample after the cleaning and rinsing steps, all in the same chamber.

5.5 Conclusions

Due to the acidic nature of the photoresist, basic solutions were used to dissolve unmodified photoresist while lifting the hardened crust from the surface. Bases also attack the Si-O interface underneath the photoresist promoting a lift-off mechanism. Organic solvents were not effective in residue removal probably because of the highly cross-linked nature of the photoresist residue. Tetraalkylammonium fluoride salts were also effective – however, there is a possibility of damage to the SiO_2-based low-*k* dielectrics in such approaches. $TMAHCO_3$-methanol solution was found to be an effective co-solvent to CO_2 for removing the etch residues without damaging the dielectric. High pressure cleaning studies indicate that the solubility of additives in CO_2 greatly influences the cleaning ability of CO_2 based mixtures.

CHAPTER 6

ETCH RESIDUE REMOVAL USING CO_2-$TMAHCO_3$-METHANOL MIXTURES

6.1 Introduction

Knowledge of phase behavior or solubility of co-solvents in CO_2 is necessary to establish the process conditions for improved cleaning performance with the lowest concentration of additives. Conditions under which a single phase exists in the mixture facilitates uniform residue removal across the wafer surface. With a single phase mixture, no local non uniformities in the active species' ($TMAHCO_3$) concentration should exist other than those governed by mass transport, which can be enhanced by optimizing the flow profile of the mixture across the wafer surface. Such issues would be of more concern in an integrated circuit (IC) manufacturing environment, where 300 mm wafers are used as substrates. In this dissertation, across wafer uniformity is not an issue since 1cm×1cm substrates are used. It is also beneficial to use single phase mixtures from a process control point of view – cleaning performance would be more predictable and repeatable than two phase mixtures because of uniform distribution of the additives. However, it is possible to remove etch residues using two phase mixtures. In two phase mixtures (with vapor+liquid) under flow conditions, liquid droplets (co-solvent rich) are entrained in the vapor phase (CO_2 rich). These droplets have higher concentration of the additives than the vapor phase; thus, they condense on the sample surface and promote cleaning.

Due to its ionic nature, the solubility of $TMAHCO_3$ in supercritical CO_2 is expected to be very small even in the presence of methanol as a co-solvent. The solubility of quaternary ammonium salts which are commonly used as phase transfer catalysts (PTC) for heterogeneous reactions in CO_2, has been reported previously [178]. For example, the solubility of tetraheptylammonium bromide in CO_2/5% acetone mixture at 75 ^oC and 3000 psi was reported to be only 1.1×10^{-5} mole fraction. The solubility increased with increasing pressure and decreasing temperature (increasing CO_2 density). Indeed, high temperatures/pressures may be necessary to achieve a supercritical state in CO_2 with ionic salts. In such cases, a single liquid phase may be obtained at moderately high pressures by tailoring the composition of the mixture. The resulting liquid mixtures may possess a desirable combination of superior transport properties and high solvent strength (higher density than supercritical fluids).

In this chapter, the phase behavior of CO_2-$TMAHCO_3$-methanol mixtures is reported in the form of bubble point curves. Based on the phase behavior, the composition of the mixture is altered to achieve a single liquid phase at moderate pressures. The influence of phase state on the cleaning ability of CO_2 based fluids is also reported. No such attempt has been made previously although the phase behavior in CO_2 of some of the additives used for photoresist removal is known (e.g. propylene carbonate [166]).

6.2 Phase behavior of CO_2-$TMAHCO_3$-methanol mixtures

The phase behavior of the mixtures developed for etch residue removal has been determined by G. Levitin et al. using a variable volume high pressure cell; the experimental set-up and the results are described in detail elsewhere [179]. The phase behavior of CO_2-$TMAHCO_3$-methanol mixtures was explored at two different temperatures (25 ^oC and 70 ^oC) with and without addition of water. The phase behavior of the $TMAHCO_3$ solution (prepared from 25 wt% TMAH in methanol corresponding to a $TMAHCO_3/CH_3OH$ molar ratio of 0.127, filled squares) at 70 ^oC is shown in Figure 6.1(top). At 25 ^oC, addition of CO_2 resulted in solid phase ($TMAHCO_3$) formation at all pressures. Also shown in the figure is the phase behavior of the mixture in which TMAH was formed *in-situ* (open squares). In that case, the composition of the mixture was calculated by taking into account the reaction between TMAH and CO_2 (one mole of CO_2 is consumed per mole of TMAH). Shown in Figure 6.1(bottom) are the bubble point plots when water (1 volume per 4 volumes of TMAH solution) was added to the co-solvent. As discussed in Chapter 5, addition of water was necessary to achieve complete residue removal using CO_2-TMAH-methanol.

In the presence of water, higher pressures were required to obtain a single liquid phase because of its limited miscibility with CO_2. In cases when TMAH in methanol was used initially, a sharp increase in the mixture temperature was observed upon first addition of CO_2 to the original solution of TMAH at elevated pressure due to the exothermic nature of reactions (5.2) and (5.3). From the plots, it is clear that both final mixtures display similar phase transition pressures confirming that $TMAHCO_3$ was the

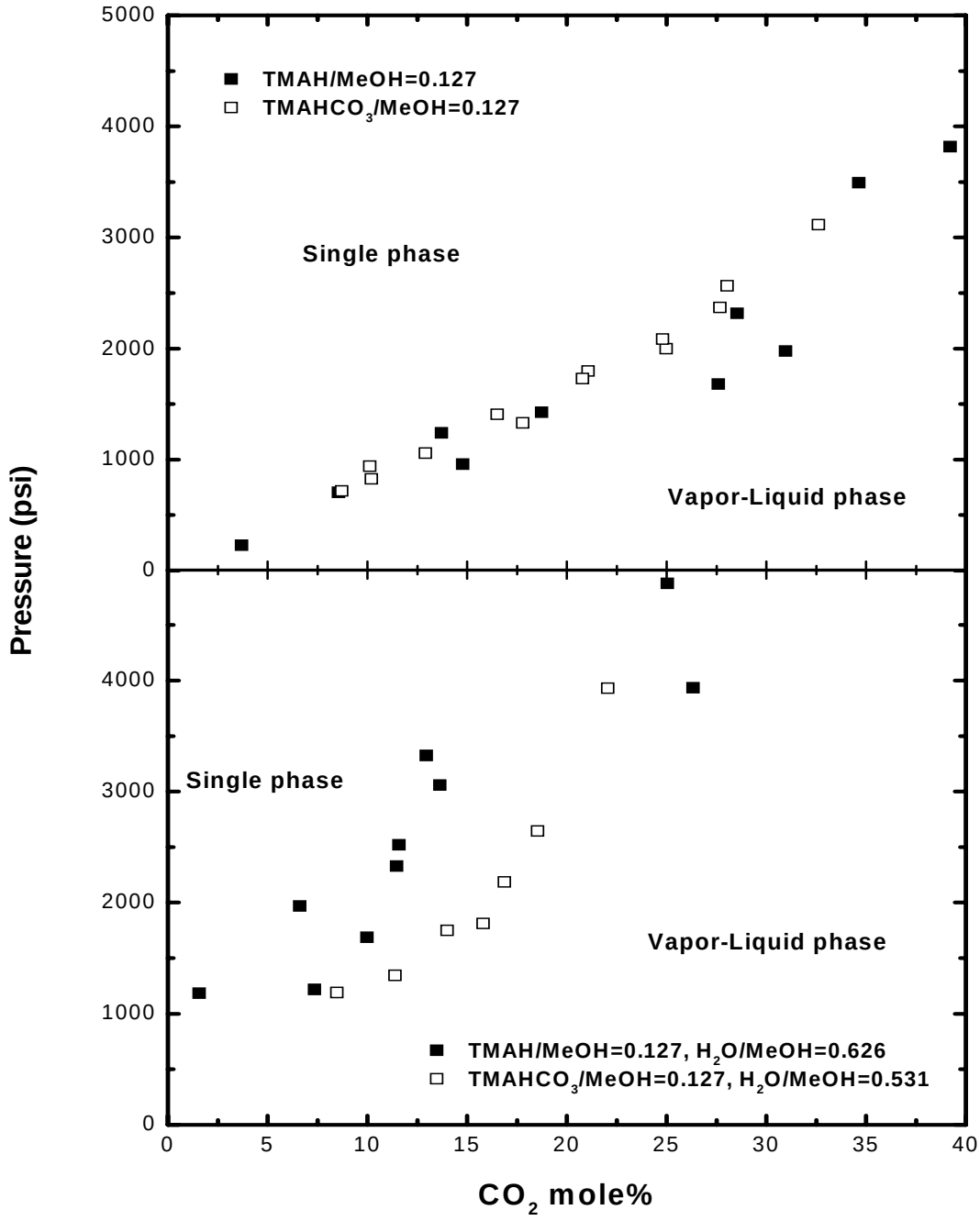

Figure 6.1. Experimental bubble point curves (at 70 ^{o}C) for CO_2-$TMAHCO_3$-methanol (top) and CO_2-$TMAHCO_3$-methanol-H_2O (bottom) [179]. The molar ratios of the individual components are also shown. The solid symbols represent the cases when TMAH was used to start with, while the hollow symbols are used when $TMAHCO_3$ was formed *apriori*.

product when equilibrium was attained. The scatter in the data is more extensive with TMAH (Figure 6.1(top)) probably due to small fluctuations in temperature and pressure that occur upon CO_2 addition resulting from the fact that an acid-base reaction is occurring during the phase measurement.

With increasing concentrations of bicarbonate, the bubble point pressures increase due to the larger concentrations of ionic species. At 40 mole% CO_2, the pressure necessary to move from the dual phase region to a single phase is about 3600 psi. In order to reduce co-solvent consumption, it is desirable to increase the mole% CO_2 soluble

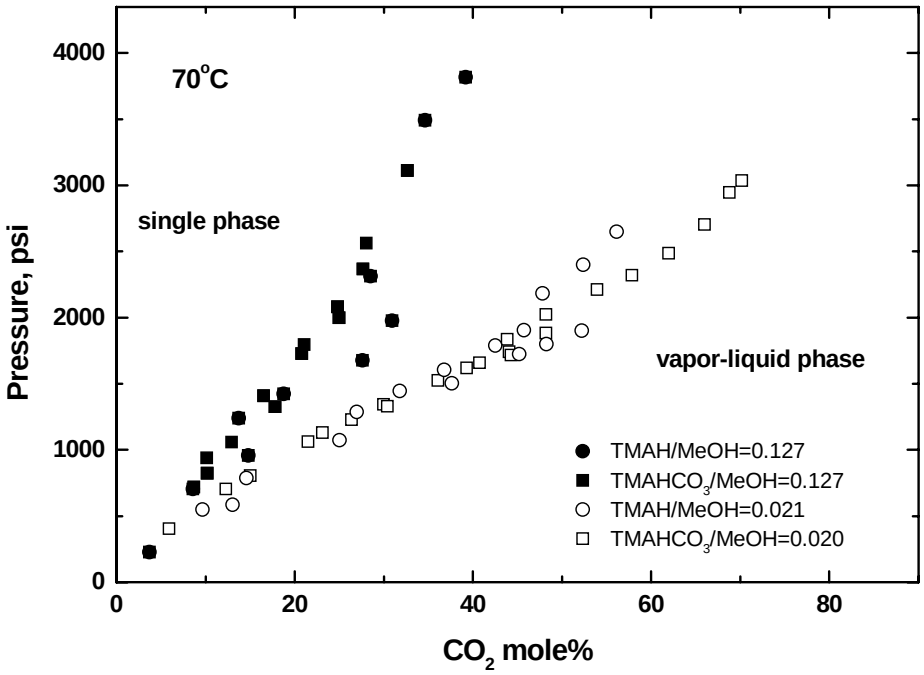

Figure 6.2. Bubble point curves for CO_2-$TMAHCO_3$-methanol mixtures under two different molar ratios of $TMAHCO_3$ and methanol in the co-solvent [179].

in the liquid mixture. Since TMAH is commercially available only in methanol (or water), the co-solvent solution was diluted to enhance the CO_2 solubility. As shown in Figure 6.2, the bubble point pressures are much lower when the molar ratio of $TMAHCO_3$ to methanol was decreased from 0.127 to 0.021. At this molar ratio, up to 71 mole% CO_2 can be added to the solution and still be in a single phase at 70 ^oC and 3050 psi. Interestingly, at room temperature, the phase behavior observed was similar to that of CO_2-methanol and CO_2-methanol-water systems [177, 180] and has an inflection point around 900 psi. Such observations suggest that the effect of bicarbonate on the phase

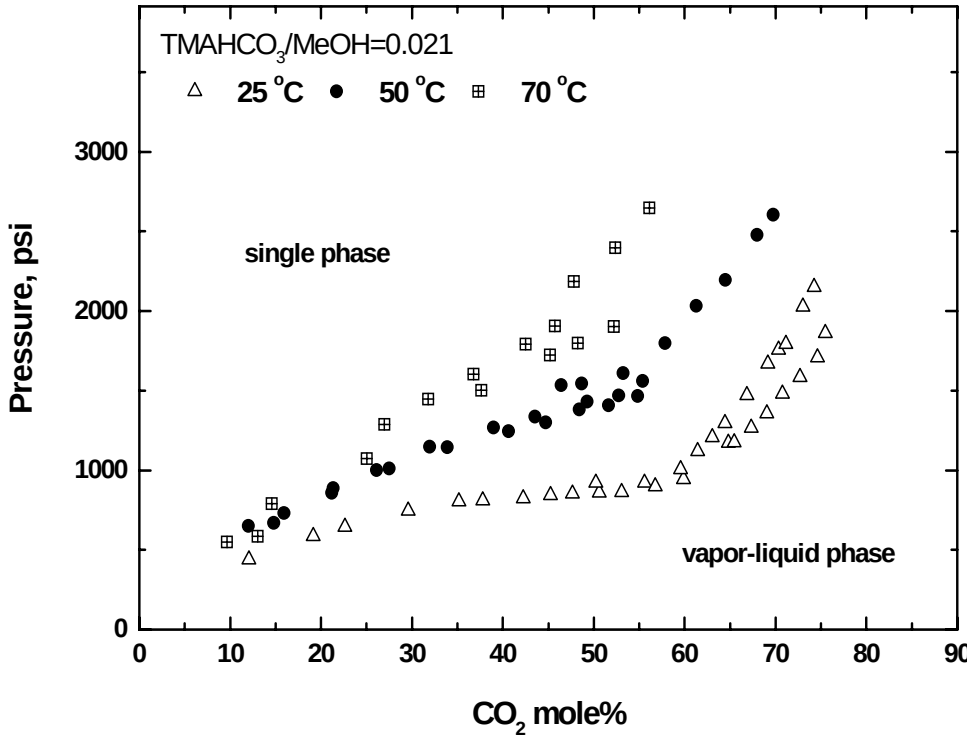

Figure 6.3. Bubble point curves for CO_2-$TMAHCO_3$-methanol mixtures at three different temperatures [179].

behavior of the mixture becomes prominent only upon addition of higher mole fractions of CO_2. As the temperature increases, the bubble curves shift to higher pressures due to the higher vapor pressure of CO_2 (Figure 6.3). Thus diluted $TMAHCO_3$ in methanol was used to formulate single liquid phase mixtures at pressures close to 3000 psi. The phase behavior of these mixtures has also been successfully modeled using the Peng-Robinson equation of state [179].

6.3 High pressure cleaning studies

6.3.1 Determination of minimum co-solvent flow rate

The flow rate of the co-solvent was varied to determine the minimum concentration of bicarbonate required for complete residue removal in CO_2-$TMAHCO_3$-methanol mixtures. The conditions used were : 3000 psi, CO_2 flow rate 200 ml/hr, 70 ^oC; the samples were treated for 45 min and rinsed in methanol before XPS analysis. The volumetric flow rate of the co-solvent (concentrated $TMAHCO_3$-methanol) was increased from 0 to 24 ml/hr (0 to 0.057 mole/hr of $TMAHCO_3$). These mixtures yielded two phases at all flow rates investigated. Figure 6.4 shows the extent of residue removal with varying co-solvent flow rates. At least 12 ml/hr (which corresponds to 0.0262 mole/hr of $TMAHCO_3$) was required to yield a completely clean sample under the above conditions. Similar experiments were not performed with diluted bicarbonate mixtures because reducing the co-solvent flow rate at the same temperature and pressure resulted in phase separation. Pressures higher than 3000 psi are required to maintain a single phase for CO_2>80 mole%. The dotted line in Figure 6.4 represents a clean sample with Si>22%.

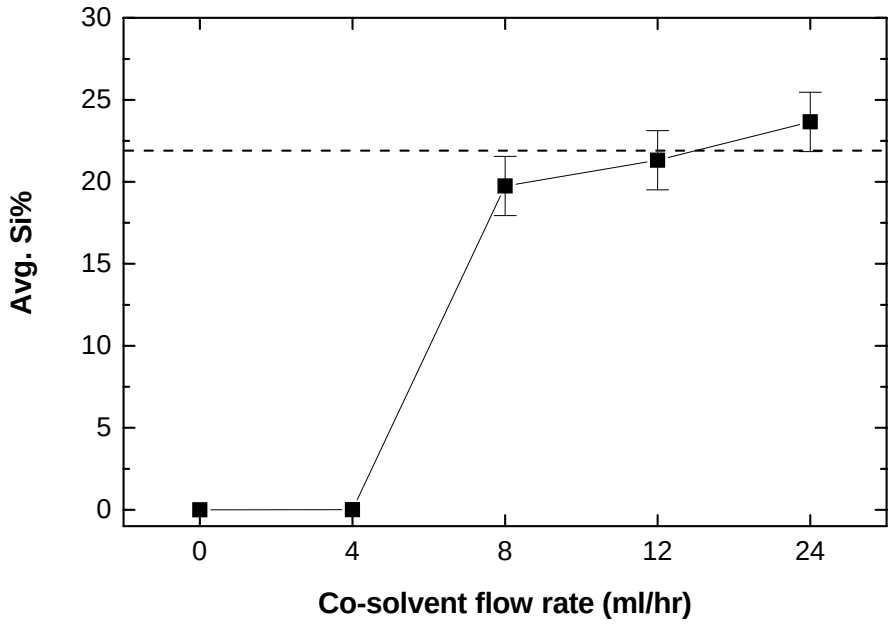

Figure 6.4. The effect of co-solvent ($TMAHCO_3$-methanol mixture) flow rate on the cleaning efficiency of two phase mixture. XPS Si>22% (dotted line) represents a clean sample.

6.3.2 Effect of temperature

Experiments in liquid $TMAHCO_3$ in methanol (at atmospheric pressure) indicated that elevated temperatures are necessary for effective residue removal. Complete removal was obtained only in ~30 minutes even at 50 ^oC. Hence, the effect of temperature was investigated on residue removal using CO_2- $TMAHCO_3$-methanol mixtures. In these mixtures, temperature comes into play in two different ways: higher temperature promotes faster residue removal by enhancing reaction (e.g. deprotonation of the photoresist) or diffusion rates. However, CO_2 density and hence, solubility of the

additives decreases with higher temperature. Hence, higher pressures are required to maintain similar phase state and composition with increasing temperatures.

In this study, the pressure, volumetric flow rates of CO_2 and co-solvent (diluted $TMAHCO_3$ in methanol) were fixed and the temperature varied from 25 ^oC to 70 ^oC. The volumetric flow rate of the co-solvent was fixed at 55 ml/hr so that the molar flow rate of $TMAHCO_3$ was 0.0262 mole/hr (which is the minimum required for cleaning under two phase conditions). Due to the change in density of CO_2, the molar composition of the mixture varies with temperature and is reported in Table 6.1. The results are plotted in Figure 6.5 in the form of average Si% on the surface (from XPS) versus temperature. As indicated by detection of silicon in the SiO_2 layer beneath the residue, complete removal occurred only at temperatures above 50 ^oC. These results are consistent with atmospheric pressure experiments (without CO_2) and suggest that the residue removal is limited by kinetics. In order to provide insight into the rate limiting step, mechanistic studies were performed; these are discussed in Chapter 7.

6.3.3 Comparison of single phase and two phase mixtures

Experiments in section 6.3.1 showed that it is possible to remove the etch residues in two phase mixtures provided that the sample is exposed to sufficient quantities of $TMAHCO_3$. In these mixtures, co-solvent droplets sprayed onto the sample surface cause removal. Although the experimental set-up was designed to minimize droplet entrainment and condensation on the sample, droplets were not completely eliminated (as observed through the optical window). The two phase mixtures also have

Table 6.1. Composition (mole%) of the mixtures used in cleaning experiments at various temperatures. The mole flow rate of $TMAHCO_3$ was constant at all temperatures and was equal to 0.0262 mole/hr.

Temperature	CO_2 mole%	$TMAHCO_3$ mole%	Methanol mole%
25 ^oC	75.93	0.47	23.59
50 ^oC	73.31	0.52	26.17
70 ^oC	70.32	0.58	29.1

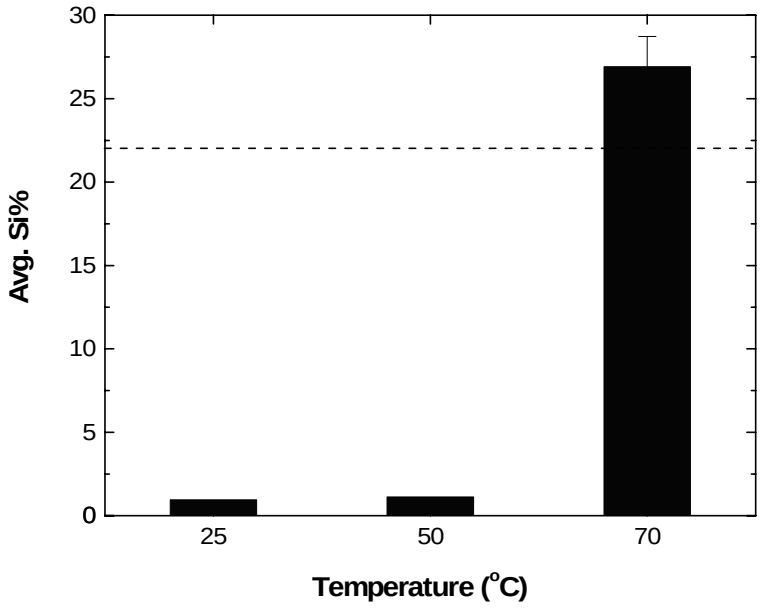

Figure 6.5. Comparison of cleaning efficiency of single phase CO_2-$TMAHCO_3$-methanol mixtures at different temperatures. XPS Si>22% (dotted line) represents a clean sample.

the advantage of lower operating pressures compared to the single phase mixtures. Multi-phase mixtures involving CO_2 have been used recently for photoresist (CO_2+organic solvents at pressures below the bubble point) [107] and molecular contaminant (CO_2 jet spray) [90] removal. However, the benefits associated with CO_2 such as enhanced transport and wetting properties may be lost when more than one phase exists. Thus, in this study, the comparative ability of single and two phase mixtures in removing the post plasma etch residues was studied.

Diluted bicarbonate solution was used as a co-solvent to obtain single phase mixtures while the (as formed) bicarbonate solution was used to obtain two phase mixtures. In both single and two phase experiments, the mole flow rate of $TMAHCO_3$ was fixed at 0.0262 mole/hr. As illustrated in Figure 6.6, the conditions used for residue treatment 'A' were: 3000 psi, 11 ml/hr $TMAHCO_3$ solution at 70 ^oC (corresponds to 92.5 mole% CO_2 and 0.8 mole% $TMAHCO_3$ with $TMAHCO_3/CH_3OH$=0.127). The point A in the phase plot lies in the two phase region. Conditions used for residue treatment 'B' were: 3200 psi, 55 ml/hr diluted bicarbonate solution at 70 ^oC (corresponds to 70 mole% CO_2 and 0.58 mole% $TMAHCO_3$ with $TMAHCO_3/CH_3OH$=0.02); this set of conditions results in a single phase mixture. Although the composition of these mixtures changes as a function of temperature, the mole flow rate of bicarbonate was constant. Both mixtures removed the residues completely when treated for 45 min. No difference was observed in the surface composition from angle-resolved XPS (ARXPS). However, this does not imply that both mixtures removed the sidewall residues to the same extent. Due to the small size and high aspect ratio of the vias, few photoelectrons from the sidewall may reach the detector. Indeed, the absence of silicon in the ARXPS spectrum of an untreated

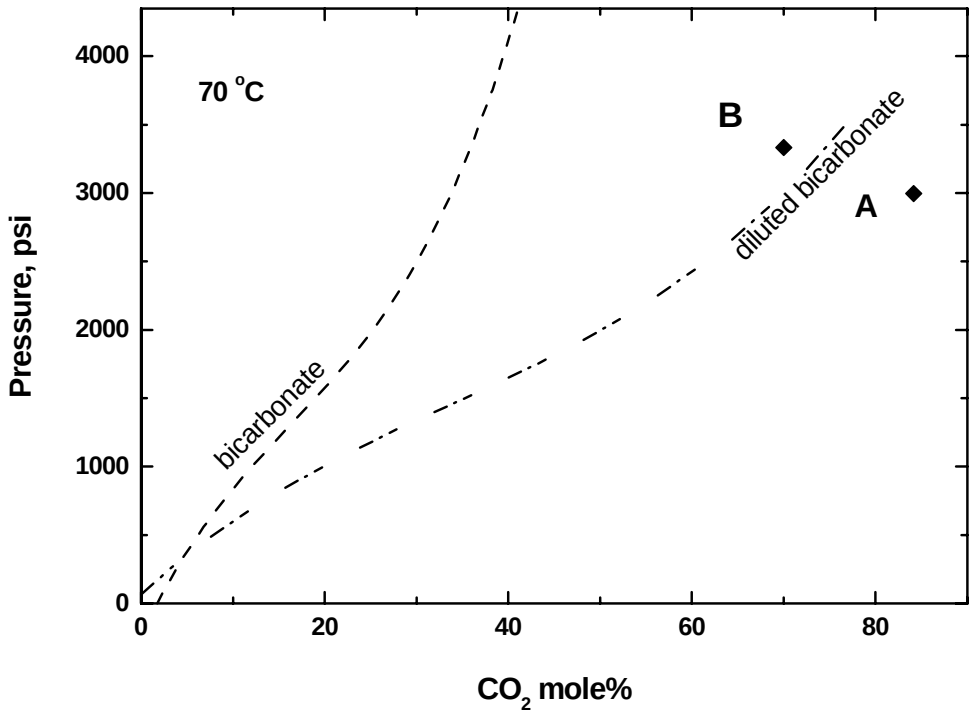

Figure 6.6. Illustration of the phase state of CO_2-$TMAHCO_3$-methanol mixtures used for comparing single and two phase mixtures.

sample is consistent with this argument.

The etch residue samples were treated for different times (5, 10, 15, 20, 30 and 45 minutes), washed in methanol and the surface composition analyzed. For both mixtures, a minimum time of exposure was required (Figure 6.7) for complete residue removal (15 min for single phase mixture and 30 min for two phase mixture) confirming that the amount of bicarbonate that contacts the sample surface is crucial. It is also evident that cleaning with a single phase mixture was more efficient; that is, a shorter time relative to a two phase mixture was required for complete residue removal. The extent of residue

removal obtained (at any time) was also improved with single phase mixtures. The system was designed to prevent liquid droplets from contacting the sample; hence, a significant amount of additives in the two phase mixtures do not contribute to surface cleaning. Since the single phase mixtures use the additives to a greater extent, the $TMAHCO_3$ flow rate can be reduced below 0.0262 mole/hr.

The minimum mole flow rate required for complete residue removal (0.026 mole/hr) also depends on the geometry of the system, and other parameters such as CO_2 flow rate, temperature etc. The additive consumption can be reduced by minimizing the dead space volume in the system, improving the CO_2-co-solvent mixing, delivering the

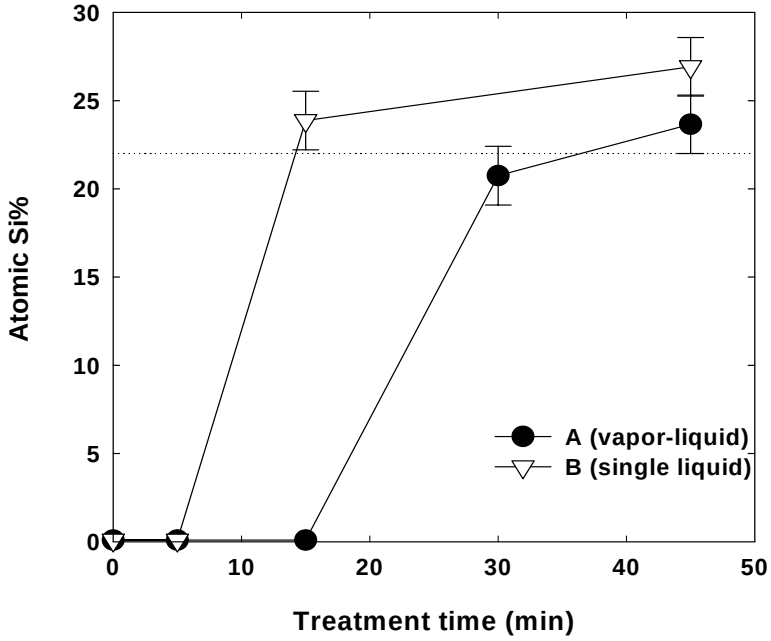

Figure 6.7. The effect of treatment time on the cleaning efficiency of CO_2-$TMAHCO_3$-methanol mixtures at different phase states. XPS Si>22% (dotted line) represents a clean sample.

mixture to the sample surface (e.g. by a nozzle) and/or by increasing the temperature. The objective of this exercise was not to optimize removal conditions but to highlight the factors that can limit the residue removal.

6.4 Post treatment rinsing

After all high pressure treatments, a rinse step was necessary to remove residue remaining on the sample surface. A rinse step was also necessary after a beaker treatment in $TMAHCO_3$-methanol solution but not after TMAH-methanol treatment. During both of these treatments, parts of the residue lifted off the sample surface. The part of the residue that does not dissolve but lifts-off the surface is the most cross-linked portion of the photoresist and is referred to as 'crust'. In the case of TMAH, the crust disintegrates into small fragments whereas it begins to lift off from the edges (in one piece) in $TMAHCO_3$ solution. Application of a small lateral force during the rinse assists this process. This suggests that the crust may consist of moieties that may dissolve in a base but are in close association (entangled?) with the cross-linked moieties. Because it is a stronger base than $TMAHCO_3$, TMAH solution can dissolve some of these fragments causing the crust to disintegrate. A rinse step has been employed in CO_2 based etch residue removal methods reported previously [181]. Alternatively, pressure pulsing [105] or ultrasonic energy [182] has been used to physically remove the residue from the wafer surface.

In the present study, a simple immersion in DIW was sufficient to lift-off the crust. Sometimes, a small shear force (rinse under flowing stream of water) was

necessary to remove the crust from densely patterned regions of the sample. For this process to be integrated into IC processing, a DI water rinse must be followed by another solvent rinse and drying step. It is, therefore, not compatible with single wafer, dry in-dry out processing that the industry favors [82]. Hence, alternative rinsing agents were explored. Organic solvents with a wide variety of properties (dielectric permittivity, density, dipole moment, viscosity) were investigated – after CO_2-$TMAHCO_3$-methanol (single phase) treatment, samples were rinsed in these solvents under similar conditions (time, shear force and solvent dispensed). The samples were blown-dry and analyzed by XPS. The purpose of these experiments was twofold: to identify what properties of the solvent are responsible for its ability to remove the crust; and to identify an alternative rinsing agent. The rinsing ability (average Si%) and properties of the solvents investigated are shown in Table 6.2. The percentage of area from which the crust was rinsed away (from an optical microscope) and the area averaged Si% are listed in the last two rows of the table. There is a direct relation between the dielectric constant and the ability of the solvent in removing the crust. Solvents with high dielectric constant (>25) and surface tension (>20 N/m) were found to be most efficient in removing the crust. High surface tension fluids may not wet the fluorinated crust, but may lift off the crust (absence of capillary forces). During the rinsing process, the bicarbonate salt may also dissolve acidic moieties enhancing the residue removal; solvents with high dielectric permittivity would encourage this mechanism. Because of desirable properties such as low boiling point, high solubility in CO_2, and adequate rinsing ability, methanol was chosen as the rinsing solvent.

Table 6.2. Performance of various rinsing solvents and their properties [87].

Solvent→	DIW	Methanol	Ethanol	Isopropanol	Chloroform	DMSO	Acetone	Acetonitrile
Surface Tension (25^oC, N/m)	71.99	22.07	21.97	20.93	26.67	42.92	23.46	28.66
Dielectric constant (20^oC)	80.1	33.0	25.30	20.18	4.807	47.24	21.01	36.64
Density (g/cc)	0.997	0.7914	0.785	0.7855	1.474	1.092	0.79	0.7857
Dipole moment (gas phase, D)	1.854	1.70	1.68	1.58	1.04	3.96	2.88	3.924
Viscosity (25^oC, mPas)	0.89	0.544	1.074	2.038	0.537	1.74	0.306	0.369
Boiling point (^oC)	100	64.70	78	81-83	60.5-61.5	190-191	56.5	81-82
Avg. Si%	25.8	24.6	24.4	18.5	19.4	25	0.9	20.9
%area removed	100	100	95	65	75	100	0	100

It is desirable to remove the residue, rinse, and dry the sample in the same chamber. This would improve the throughput (time required to transfer the sample from chamber to chamber is reduced) and no additional equipment would be necessary for post clean processing. Such integrated processing is being actively pursued in the IC industry to reduce costs and cross-contamination [10]. Hence, an attempt was made to remove the crust inside the cell following the cleaning treatment. Methanol was flowed through the system for 15 min to remove the crust; from the optical window, it appeared that parts of the crust came off the sample and were carried away by the fluid. However, in the absence of sufficient force, complete removal was not achieved. The system has to be modified to include a mechanism (e.g. a nozzle) by which necessary force can be imparted during the rinse. Following the rinse, methanol can be purged and the sample dried in supercritical CO_2. Such an *in-situ* methanol wash also serves as a cleaning step for the chamber and the delivery lines.

6.5 Conclusions

In this chapter, post plasma etch residue removal efficiency of CO_2-$TMAHCO_3$-methanol mixtures was investigated as a function of elevated pressure cleaning mixture phase state. The phase behavior of the CO_2-$TMAHCO_3$-methanol system was used as a guide to develop the process conditions and composition of the co-solvent. At a fixed mole flow rate of additive, the single phase cleaning mixtures demonstrated higher removal efficiency than do the two phase mixtures. To achieve complete residue removal with the two phase mixtures, longer treatment times and higher flow rates were required.

The difference in removal efficiency between these mixtures can be attributed to the different amounts of active ingredient ($TMAHCO_3$) that contacts the residues. Use of single phase mixtures facilitates easier transport of active species to the surface. In both cases, no cleaning occurs at temperatures below 50 ^oC.

Removal seems to occur primarily by interfacial delamination of the residue and an appropriate rinsing solvent must be chosen to promote this mechanism. Incorporating *in-situ* rinsing and drying steps after the cleaning step would allow a dry wafer in-dry wafer out approach.

CHAPTER 7

MECHANISTIC STUDIES

7.1 Introduction

In the previous chapters, CO_2-$TMAHCO_3$-methanol mixtures were shown to be effective for post plasma etch residue removal. It appears that the cleaning process is temperature limited and a rinse step is necessary to remove the 'crust' from the surface. In this chapter, mechanistic studies are reported that provide better understanding of the cleaning process, the limiting factors, and the role of each component in the cleaning process. The advantages of CO_2 based mixtures over liquid solutions for etch residue removal are also demonstrated.

Understanding the mechanism of etch residue removal is important for several reasons: to improve the process by using alternative chemistries or solvents to overcome limiting factors, to be able to achieve better process control, and to extend this process to other materials or residues. Very few publications exist that deal with the removal mechanism of post plasma etch photoresist residues. This is probably due to the fact that the photoresist residues do not have a well defined chemical structure – the composition or chemical bonding depends on the material being etched, the specific photoresist (or mask) used and the etch chemistry employed. In addition, etch process variables such as temperature, gas flow rate, time or post etch processing can alter the thickness or composition of these residues. Also, the etch residues are not homogenous or isotropic

and usually are very thin. On the other hand, the chemical mechanism of fluorocarbon residue removal is better understood. Fluorocarbon residue removal involves either plasma oxidation (in O_2, H_2O plasmas) or reduction (in NH_3, N_2/H_2, NF_3 plasmas) of the CF_x residues or undercut of the residues at the Si-O interface using HF based solutions. Some of the residues removed and the reported mechanisms are shown in Table 7.1. Since the residues contain fluorocarbons, aggressive chemistries are required to chemically attack the C-F bonds. Due to the existence of radicals, ion bombardment and radiation, plasmas can provide the activation energy to attack these residues; hence, plasma 'ashing' is a common approach to remove these residues. For fluorocarbon residue removal using liquids, undercut (or attack at the interface of the residue and the substrate) is a common mechanism rather than chemical attack. During the etch residue removal, one or more of the processes occurs:

1. Dissolution of the soft (pristine) photoresist

2. Chemical attack of the residue by the cleaning mixture

3. Undercut of the residue resulting in lift-off

In the following sections, each of these possible mechanisms is investigated. Model etch residue films and fluorocarbon films are used to gain insight into the removal mechanism. Analytical techniques such as angle-resolved XPS and ATR-FTIR are used to probe the surface processes that occur during high pressure cleaning treatments.

Table 7.1. Mechanism of photoresist and etch residue removal by various cleaning techniques.

Reference	Residue	Cleaning method	Reported mechanism
X. Zhang et al. [118]	Post ash residue after etching MSSQ	CO_2 + water + surfactant	Partial Dissolution of particles in the microemulsion
D. Beery et al. [52]	Post ash residue	Densified NH_3 + megasonic	NH_3 extraction of organometallics; stress induced detachment of the sidewall residues
S. Ma et al. [78]	Photoresist residue	O_3/DIW	Oxidation of the residue to CO_2, O_2
J. R. Hu et al. [65]	Photoresist residue	NH_3 plasma	Photoresist breakdown to HCN, H_2O
M. A. Hartney et al. [11]	Photoresist residue	O_2 plasma	Photoresist breakdown to CO_2, CO, H_2O
Y. Lee et al. [72]	Post via etch residue	Pulsed excimer laser irradiation	Photothermal ablation of the residues
Y. Kim et al. [183]	Post Si etch residue	O_2 plasma followed by NH_4OH/H_2O_2 treatment	Undercut of the residues by SiO_2 etching
R. J. Carter [184]	Post SiO_2 etch residue	Remote H_2 plasma	Residue breakdown by the H radicals
K. Ueno et al. [73]	Post SiO_2/Cu etch residue	Dilute HF	Dissolution of CuO
F. Lanckmans et al. [185]	Post metal etch residue	Hydroxylamine based solvents	Dissolution of metal oxides
K. L. Chavez [162]	Photoresist	Acetic acid	Dissolution
T. Kamal [169]	Photoresist with adhesion promoter	$IPA/NH_4OH/H_2O$	Photoresist dissolution + undercut of the adhesion promoter
M. Jolley [186]	Post tungsten CMP particles	0.1 N TMAH	Undercut of the particles by TMAH etching the metal oxide

7.2 Dissolution of the soft photoresist

When the etch residue sample is exposed to CO_2-$TMAHCO_3$-methanol mixtures, the underlying pristine photoresist may dissolve, leaving behind the fluorinated crust that may be removed by rinsing. However, since the fluorocarbon residue is deposited in all areas exposed to the plasma, a continuous layer of residue is deposited that connects the photoresist surface to the etched sidewall. Hence, the solvent has to penetrate this fluorocarbon residue to reach the photoresist. This particular mechanism was investigated by treating blank films of photoresist resin (tert-butoxy carbonyl protected poly 4-hydroxystyrene, PHOST-tBOC) and model etch residue (PHOST-tBOC film exposed to a fluorocarbon etch plasma to form uniform, unpatterned residue; sample RIE-9 in section 4.3.2) in the cleaning mixtures. The composition and deposition procedure for these films was described in Chapter 4. The samples were exposed to CO_2 (3000 psi, 70 ^{o}C, 45 min, 200 ml/hr), CO_2-methanol (55 ml/hr; single phase mixture) and CO_2-$TMAHCO_3$-methanol (3200 psi, 55 ml/hr; single phase mixture). Digital images of the samples were taken before and after the treatments to evaluate the surface morphology. The extent of dissolution was also monitored by VASE scans before and after fluid exposures to measure the thickness.

Shown in Figure 7.1 are the optical images of the samples after exposure to CO_2 (column a), CO_2-methanol (column b), and CO_2-$TMAHCO_3$-methanol (column c) for the patterned etch residue sample (row 1), PHOST-tBOC (row 2) and model etch residue (row 3). All samples are shown without any post treatment rinsing. CO_2 alone did not cause a change in the surface morphology of the residues (1a, 3a) or the photoresist films

(2a). Ellipsometry measurements immediately after the treatment revealed swelling of the PHOST-tBOC film (~1.5%) and to a lesser extent (~0.7%) the model etch residue film. However, when methanol was added as co-solvent, a significant amount of cracking was observed on the patterned residue (1b) and the model etch residue film (3b). These observations can be attributed to the stress induced by methanol that diffused into the film; the stress was further enhanced by CO_2 induced swelling. Since the patterned residue and the model residue film have highly cross-linked crusts on the surface that prevent expansion of the soft photoresist underneath, cracks result. No such cracks were observed on PHOST-tBOC; in fact, the film dissolved in most of the areas. Removal was not uniform, probably because of mass transport related issues; the flow of CO_2-methanol across the sample surface might have been non uniform and insufficient to supply fresh solvent to dissolve and transport solvated molecules. This possibility was evaluated by increasing the flow rates of CO_2 (from 200 ml/hr to 400 ml/hr) and methanol while keeping all other parameters fixed; a greater amount of the photoresist dissolved at higher flow rates suggesting that mass transport limits removal of the unmodified photoresist. The flow rate has no effect on the removal of the etch residue samples. This fact confirms that presence of the crust on the surface inhibits dissolution of soft resist on the patterned and model etch residue samples.

In the presence of $TMAHCO_3$ (1c, 2c, 3c), the samples appeared similar to those after CO_2-methanol treatments but with greater irregularity on the surface. No removal was observed on the patterned etch residue samples without a rinse step. With $TMAHCO_3$ addition, more PHOST-tBOC dissolved perhaps due to a very thin layer of liquid ($TMAHCO_3$ rich) that remained on the sample after treatment. Unlike the

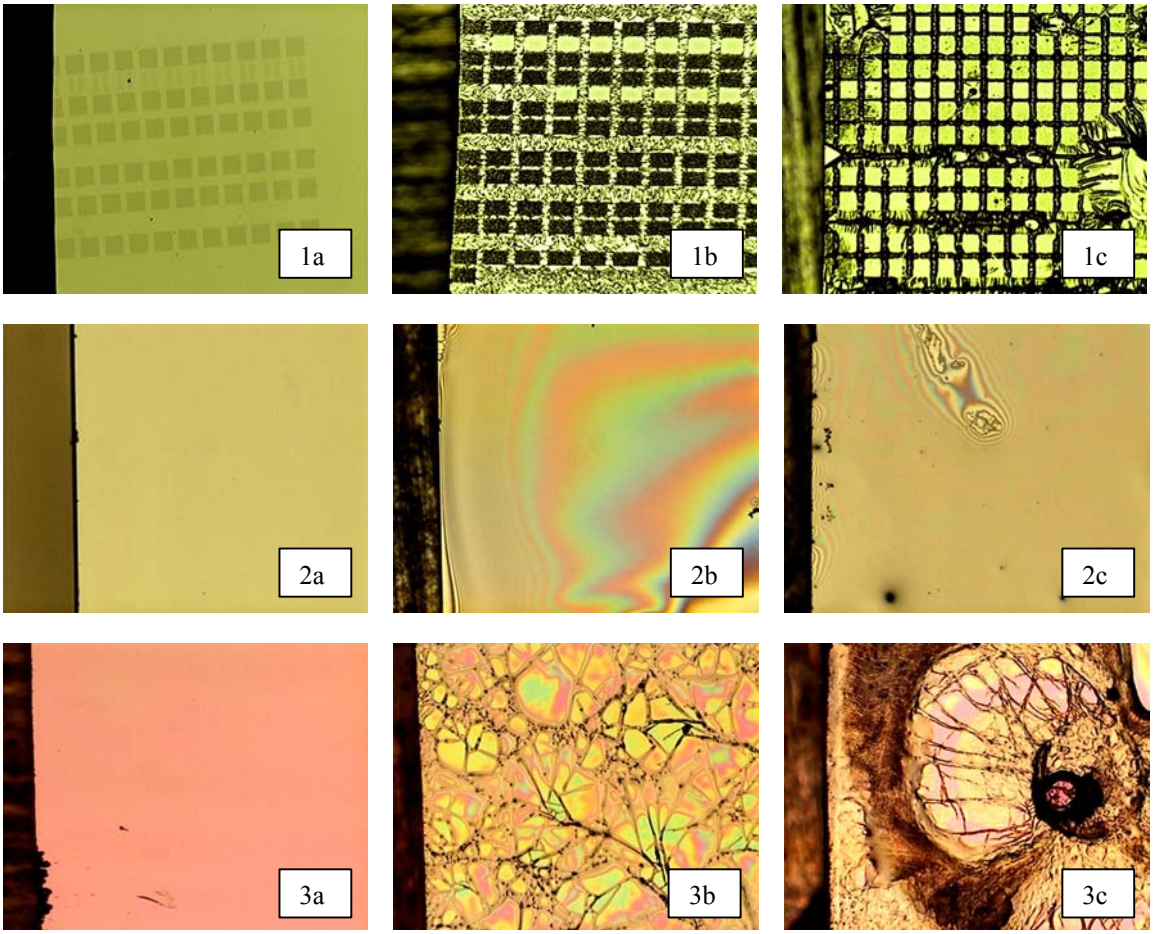

Figure 7.1. Optical images after exposure to CO_2 (column a), CO_2-methanol (column b), and CO_2-$TMAHCO_3$-methanol (column c) for the patterned etch residue sample (row 1), PHOST-tBOC (row 2) and model etch residue (row 3).

patterned etch residues, the model etch residues were removed to some extent. In the patterned etch residue sample, the top crust is held to the substrate through the via sidewall polymer. Thus, it is more difficult to remove the patterned residues. This observation is consistent with the fact that residue in the densely patterned areas was the most difficult to remove using CO_2-$TMAHCO_3$-methanol mixtures followed by a methanol rinse.

7.3 Chemical attack of the fluorocarbon residue

If the cleaning mixtures chemically attack the fluorocarbon crust, the kinetics of this attack may be limiting the residue removal. This mechanism was verified by exposing blanket fluorocarbon films to the $TMAHCO_3$-methanol mixture which is the active ingredient in the cleaning mixtures. Since the fluorocarbon residues deposited during the etching process are very thin (<10 nm), the deposition conditions were altered (discussed in Chapter 4) to deposit thicker films for these studies. The resulting films had similar carbon bonding structure to the patterned etch residue samples. The fluorocarbon films were exposed to $TMAHCO_3$-methanol solutions (in a beaker) and the surface composition analyzed by XPS. Surface atomic concentrations on these samples are shown in Table 7.2.

Table 7.2. XPS surface atomic composition of model fluorocarbon films treated in $TMAHCO_3$-methanol solution.

Sample treatment	Carbon%	Oxygen%	Fluorine%	Silicon%
Untreated	47.8	3.4	48.8	0
$TMAHCO_3$-methanol at 20 ^oC for 15 min	48.5	5.6	45.9	0
$TMAHCO_3$-methanol at 50 ^oC for 15 min	52.0	8.0	40.0	0

No silicon was detected after treatment for 15 min implying that the films were not removed. In fact, ellipsometric thickness measurements revealed a negligible decrease in thickness after treatment. When treated for 30 min, however, the films lift-off from the edges of the samples. This indicates that these samples are vulnerable to attack at the interface between the film and the Si substrate. Also, it is evident from the table that there is a small reduction in fluorine concentration and a corresponding increase in oxygen and carbon concentration. Apparently, these basic alcohol solutions cause dehydrofluorination of the residue at elevated temperatures [187]. A possible mechanism for this process is shown in Equation 7.1. It is also plausible that the $TMAHCO_3$-methanol mixture extracted some uncross-linked, small fluorocarbon molecules from the film.

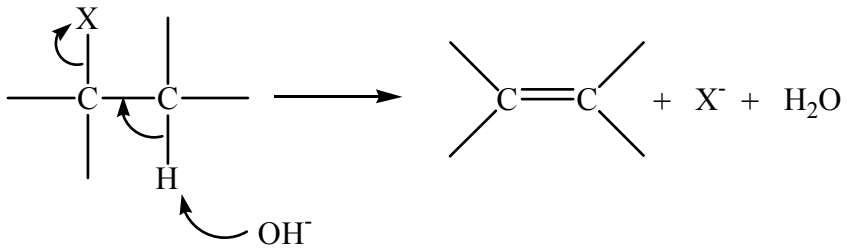

(7.1)

Dehydrofluorination of the fluorocarbon residues in $TMAHCO_3$-methanol solutions can be confirmed by detecting unsaturated bonds on the surface. This was done by derivatizing the surface using Br_2 to detect double bonds. Such chemical derivatization is commonly used to detect specific functional groups (such as OH, NH_2, C=O, C=C) using XPS or mass spectrometry [188]. Br_2 selectively participates in electrophilic addition with C=C bonds as depicted in Equation 7.2 [187]. In the presence of UV light or high temperatures (>250 ^oC), Br_2 can also react with alkanes. Treated and untreated fluorocarbon samples were exposed to Br_2 vapor in a closed vial for 15 min.

The samples were rinsed in DIW and analyzed for bromine concentration by XPS. The Br atomic concentration increased slightly from 0.9±0.1% for an untreated sample to 2.1±0.5% for a sample treated at 50 ^{o}C. No increase in Br concentration was observed for a sample treated at room temperature.

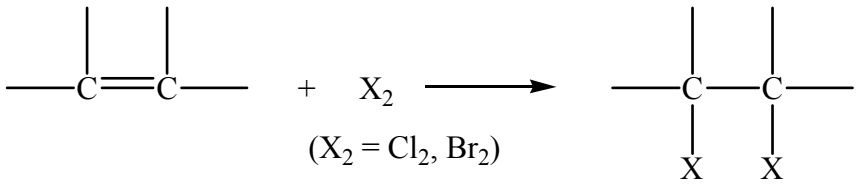

(7.2)

FTIR was also used to monitor the bonding structure of the fluorocarbon samples with $TMAHCO_3$-methanol treatments. For enhanced sensitivity, an ATR-FTIR (with multiple reflections) technique was used. The fluorocarbon films were deposited on a ZnSe ATR crystal (50mm×20mm×2mm). Due to the conformal nature of the plasma, film was also deposited on the beveled edges of the crystal. This film experiences less ion bombardment than the film on the side of the ATR crystal; thus, it was removed using a soft wiper (Kimwipes®) dipped in acetone. The crystal was then placed on the ATR accessory, the mirrors aligned to maximize the IR signal, and a spectrum collected (512 scans, 4 cm^{-1} resolution). The crystal was then exposed to $TMAHCO_3$-methanol solution (50 ^{o}C) for different times (2, 5, 10, 20, 30 min) and the corresponding spectra collected. The spectra are shown in Figure 7.2; absorbance in the range 2700-3200 cm^{-1} is magnified in the inset. The broad peak at ~1220 cm^{-1} which corresponds to C-F stretch decreases with treatment time. The C=O stretching vibration peak at ~1720 cm^{-1} remains constant after the first 2 min of treatment. From the magnified region in the inset, it is clear that the alkane C-H stretching vibration peaks in the region 2840-2975 cm^{-1}

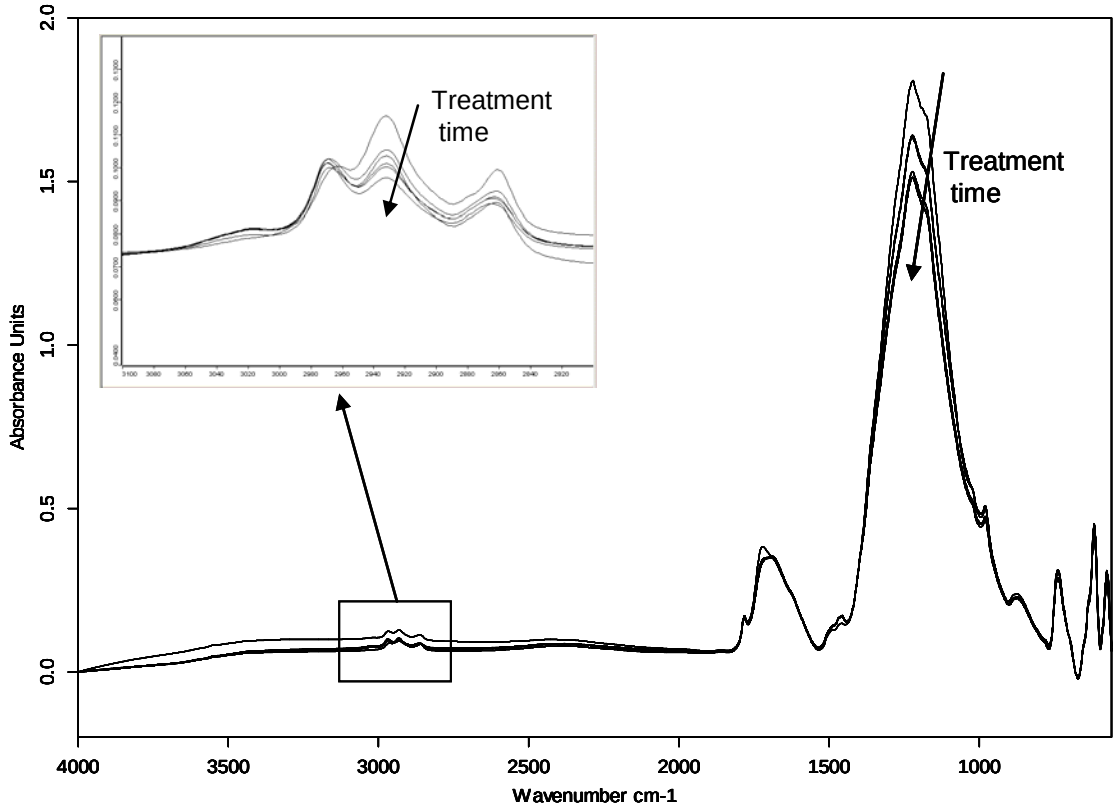

Figure 7.2. ATR-FTIR spectra of model fluorocarbon films treated in $TMAHCO_3$-methanol solutions; C-H stretching region is magnified in the inset.

decrease with treatment time. Also a small shoulder appears at 3025 cm^{-1} after the treatments which corresponds to alkene C-H stretching vibration. This suggests that some dehydrofluorination occurs during $TMAHCO_3$-methanol treatments. An SEM micrograph of the sample revealed defects on the surface such as 'pitting', 'wrinkling' etc. (Figure 7.3). This is likely caused by the extraction of small fluorocarbon fragments from regions with pinholes in the film or stress induced cracking. The extent of surface damage was greater when patterned etch residues were treated in these mixtures (

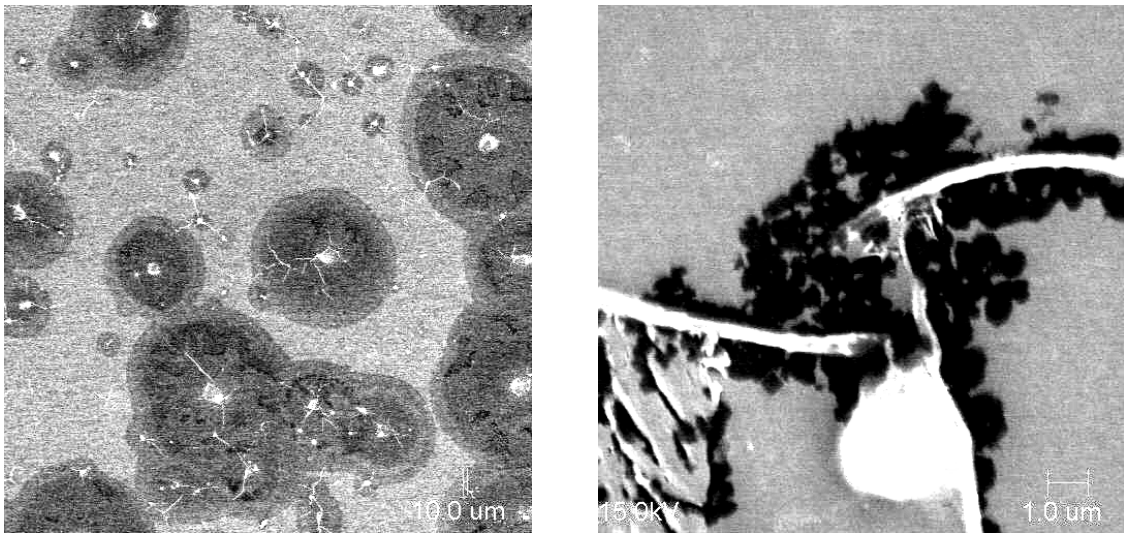

Figure 7.3. SEM micrographs of fluorocarbon films treated in $TMAHCO_3$-methanol solutions.

Figure 7.1c), probably due to a more permeable crust and to the presence of soft photoresist underneath.

7.4 Undercut of the residues

Dehydrofluorination or local extraction of fluorocarbon species by the $TMAHCO_3$-methanol mixture may not cause complete residue removal. These mechanisms do not cause a breakdown of the residue into smaller fragments and cannot account for the crust lifting from the surface during rinsing. The later observation, in fact, suggests that a loss of adhesion between the residue and the substrate may be the dominant mechanism. The cleaning mixture may be attacking the interface causing the residue to lift-off during the rinsing step that follows. The undercut may be caused by the

attack of Si-O bonds (between the residue and the capping layer or the dielectric) by OH^- ions in the weakly basic cleaning mixture [169]. In fact, the F^- ions generated during dehydrofluorination of the fluorocarbon residue (Equation 7.1) may also contribute to this mechanism [170]. This mechanism was verified by measuring the etch rates of the SiO_2 capping layer in $TMAHCO_3$-methanol solutions.

Blanket films of plasma deposited SiO_2, the capping layer in the patterned samples, were exposed to $TMAHCO_3$-methanol solutions both in a beaker and at high pressures. The average etch rate was calculated from the ellipsometric thickness before and after treatment. The measurements were taken at the same point on the samples and were repeated for consistency. The etch rate of CORAL™ low-*k* dielectric was also monitored to ensure that these cleaning mixtures do not attack the dielectric. Etch rate is a common metric used to evaluate compatibility of cleaning mixtures with dielectric materials. A slight undercut of the dielectric may also aid in removal of the sidewall polymer. The average etch rate of plasma deposited SiO_2 in $TMAHCO_3$-methanol mixture (concentrated solution) was 0.55±0.05 nm/hr at 50 ^oC and ~0 nm/hr at 20 ^oC. CORAL™ etched at 0.36±0.02 nm/hr and 0.19±0.19 nm/hr at 50 ^oC and 20 ^oC respectively. These measurements support the hypothesis that undercut of the residues may be the dominant mechanism of residue removal. Elevated temperatures are necessary to attack the interface and facilitate residue lift-off; hence, residue removal using $TMAHCO_3$-methanol mixtures was limited by temperature. During the rinsing step, the rinse solvent may remove the loosened residue from the surface.

Although $TMAHCO_3$-methanol mixtures seem to rely on undercutting to remove residues, the etch rates of SiO_2 and CORAL™ were small. The ITRS roadmap stipulates that the dielectric thickness loss due to cleaning steps must be less than 2.5%. Hence, for a 90 nm via, the amount of dielectric etched during the cleaning step must not be more than 2.25 nm. The low etch rates of CORAL™ (0.36 nm/hr) and SiO_2 (0.55 nm/hr) in these solutions ensure that these requirements are satisfied. In addition, FTIR of the films after the treatment indicated no change in the bonding structure of the bulk dielectric film. Therefore, these mixtures are compatible with dual damascene processing with CORAL™ as the dielectric material (or other materials with similar bonding structure). In fact, negligible etch rates were observed on samples exposed to CO_2-$TMAHCO_3$-methanol mixtures. This could be due to the lower concentration of $TMAHCO_3$ in the high pressure mixture relative to the liquid mixture. The etch rate is still sufficient to undercut the residue and loosen it. Addition of water (1 volume per 4 volumes of $TMAHCO_3$-methanol) to the co-solvent resulted in an increase in SiO_2 etch rate to 1.6 nm/hr, due to greater dissociation of $TMAHCO_3$ in the high dielectric constant medium, forming a higher concentration of OH^- (which causes the etching) in the presence of water. Hence, the presence of excess water may be detrimental to compatibility of cleaning solutions that rely on an undercut mechanism. In these experiments, addition of water resulted in two phase mixtures since pressure and temperature were constant.

7.5 Role of CO_2

From the discussion in the previous sections, it appears that the primary mechanism of residue removal is attack of the interface between the residue and the

capping layer by the basic $TMAHCO_3$-methanol solutions. The role of CO_2 is to enhance mass transport of the cleaning agents to the interface [189]. This is especially important with the sidewall residues in small, high aspect ratio features where aqueous solvents may have difficulty wetting [83] and thus removing the residues. CO_2 also facilitates diffusion of the additives through the highly cross-linked crust on the surface. CO_2 can also be used to dry the samples *in-situ* after rinsing the samples in solvents such as methanol, which has appreciable solubility in CO_2.

7.5.1 Angle-resolved XPS

In section 7.3 , evidence of extraction of residues from the sample by $TMAHCO_3$-methanol mixtures was presented. The depth of extraction of the residues/modification of the film by the liquid cleaning mixture will be determined by the diffusion of additives into the film and diffusion of the residue fragments out of the film. The depth of modification of the film by the cleaning mixture was measured using angle-resolved XPS. The iterative algorithm developed by Diao and Hess [122] (and introduced in Chapter 3) was used to estimate the depth dependent surface composition of the film after cleaning treatments. An infinite source diffusion model was assumed for the composition dependence (Equation 7.3) and the XPS data at several angles was used to fit the data to obtain the model parameters. The model equation describing infinite source diffusion is:

$$c_i(z,t) = c_{B,i} + c_{S,i}\,\mathrm{erfc}[\Delta_i z] \tag{7.3}$$

where, $c_i(z,t)$ is the time dependent atomic concentration of element i at depth z into the film, $c_{B,i}$ is the bulk concentration of element i, and $\frac{1}{\Delta_i}$ is the penetration depth of element i at time t. Using the XPS composition of the film immediately after deposition as the bulk composition, the parameters c_i and Δ_i were estimated by this algorithm. The model used the attenuation lengths of the photoelectrons emitted from the individual atoms (C, O, F, in this case, since H is not included in the model). These numbers were obtained using the NIST Electron Effective Attenuation-Length Database Version 1.0 (EEALD 1.0) [190].

Shown in Figure 7.4 is the atomic concentration profile in a fluorocarbon film (to simulate the fluorocarbon residue, described in Chapter 4) after treatment in $TMAHCO_3$-methanol solution (beaker, 50 ^oC, 30 min). There is a surface enhancement in carbon and oxygen concentration, and depletion in fluorine concentration; the depth of modification appears to be 5-6 nm approximately. In general, the change in surface concentration was higher for treatment at higher temperatures and for longer times. The depth of modification is larger when the samples were treated at higher temperatures where the diffusion coefficients are higher. Based on these measurements, it would take approximately 40 min for the cleaning solution to penetrate the fluorocarbon crust thickness on etch residue samples which was estimated to be 7.8 nm. In fact, the time it takes to clean the patterned samples in a beaker at 50 ^oC was found to be 30-40 min.

Similar measurements were made on fluorocarbon samples exposed to CO_2 at 70 ^oC and 3000 psi for 30 min. As shown in Figure 7.5, even CO_2 treatment caused modification of the surface composition probably due to extraction of small residues.

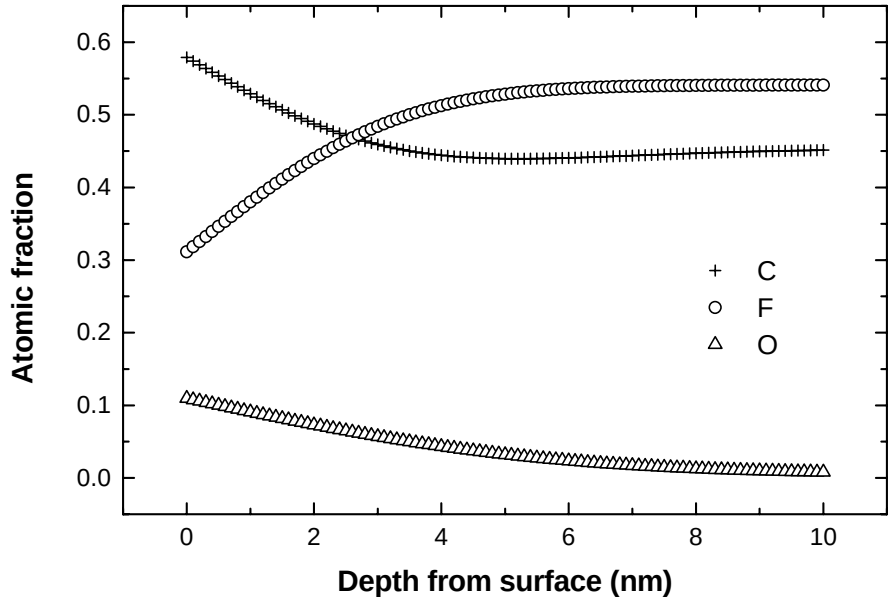

Figure 7.4. Concentration profile by ARXPS in a fluorocarbon film after treatment in $TMAHCO_3$-methanol solution at 50 ^oC for 30 min.

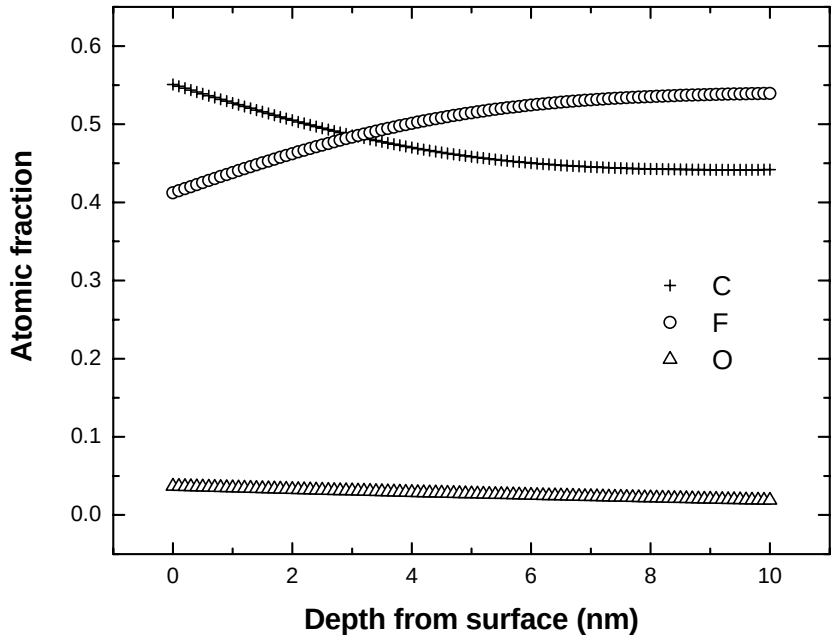

Figure 7.5. Concentration profile by ARXPS in a fluorocarbon film exposed to CO_2 at 70 ^oC for 30 min.

The extent of modification was not as extensive as that observed for $TMAHCO_3$-methanol treatment (Figure 7.4) but the depth of modification was higher. This supports the hypothesis that CO_2 can promote transport of cleaning agents through the crust on the surface. Similar measurements were not performed with CO_2-$TMAHCO_3$-methanol mixture because extensive cracking of the sample was observed after a 45 min treatment.

7.5.2 Attenuated total reflection - Fourier transform infrared spectroscopy

In-situ ATR-FTIR spectroscopy of the fluorocarbon residue during exposure to the cleaning mixtures has established that the presence of high pressure CO_2 promotes diffusion of chemical additives though the residue. A fluorocarbon film coated on an ATR crystal was exposed to CO_2, a $TMAHCO_3$-methanol mixture, and a CO_2-$TMAHCO_3$-methanol mixture to study the diffusion rate of the additives through the model residue. The peaks at 2340 cm^{-1} (O=C=O asymmetric stretching) and 3350 cm^{-1} (O-H stretching vibration) were monitored for diffusion of CO_2 and methanol respectively. The prominent peaks for $TMAHCO_3$ are C-H stretching vibrations (2800-3000 cm^{-1}) and C-O stretching vibration (from HCO_3^-, at 1400-1420 cm^{-1}). The C-H stretching peaks overlap with those of methanol and of the film. Since a Si ATR crystal was used in these studies (Si is more compatible with high pressure gradients than ZnSe), no signatures were obtained below 1500 cm^{-1}. Hence, diffusion of $TMAHCO_3$ was not explicitly monitored. The experiments involving CO_2 were performed at 1000 psi, while the $TMAHCO_3$-methanol experiment was performed at 50 psi. All experiments were performed in the high pressure ATR-FTIR cell (described in Chapter 3) at room temperature.

Shown in Figure 7.6 are typical spectra obtained in the CO_2, methanol signature regions. The areas under the peaks are determined as measures of the concentration of species in the evanescent region of the IR beam. In the figure, t<0 corresponds to the time when the fluid was not in contact with the film. The first spectrum collected after the fluid was introduced into the ATR cell is labeled as t=0. Since the thickness of the film was less than the penetration depth of the evanescent wave, the area under the peak at t=0 was subtracted to estimate the area of the peak due to molecules diffusing into the film. From Equation 3.6, the penetration depth of the evanescent wave for a Si crystal at 2340 cm^{-1} and 3350 cm^{-1} is 340 nm and 240 nm respectively. The fluorocarbon film was non uniform, with thicknesses between 240 nm and 560 nm.

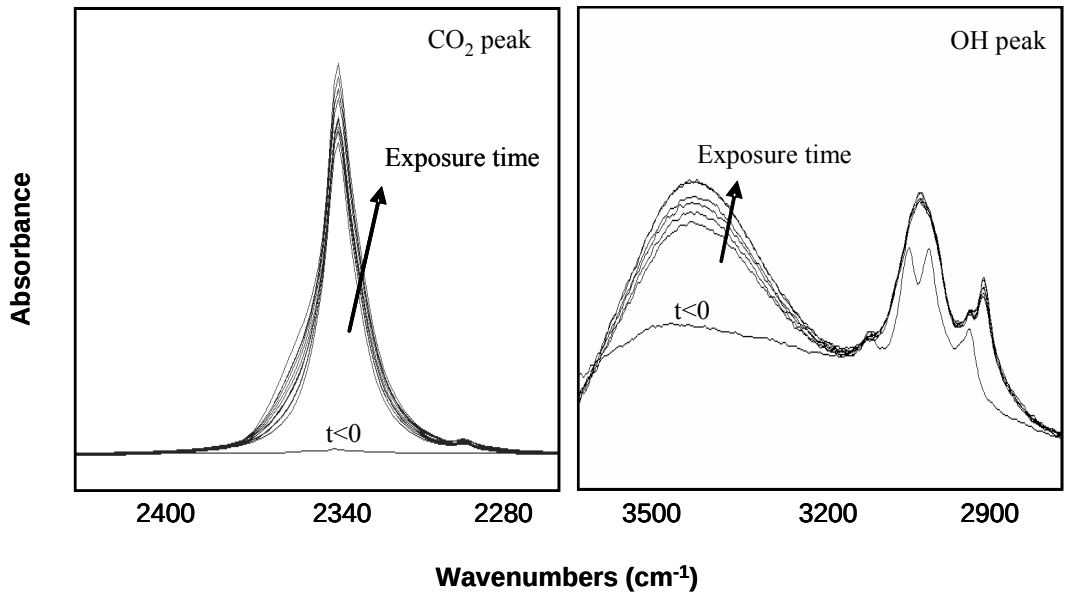

Figure 7.6. FTIR peak evolution for CO_2 (left) and methanol (right) during *in-situ* monitoring of diffusion of these species into a fluorocarbon film.

The integrated areas of the peaks are plotted in Figure 7.7, Figure 7.8, and Figure 7.9 after subtracting the areas at t=0. When the film was exposed to the liquid $TMAHCO_3$-methanol mixture, more than 2500 seconds were required for the methanol peak area to reach a maximum value indicating a very slow diffusion of methanol into the film. CO_2, because of its high diffusivity and affinity towards fluorocarbon species diffused much faster – it equilibrated in ~125 seconds. When the film was exposed to the CO_2-$TMAHCO_3$-methanol mixture, the diffusion rate of CO_2 more or less remained the same; the diffusion rate of methanol, however, increased considerably. The peak area reached a maximum value in ~250 seconds confirming that CO_2 promotes the diffusion of these additives through the crust.

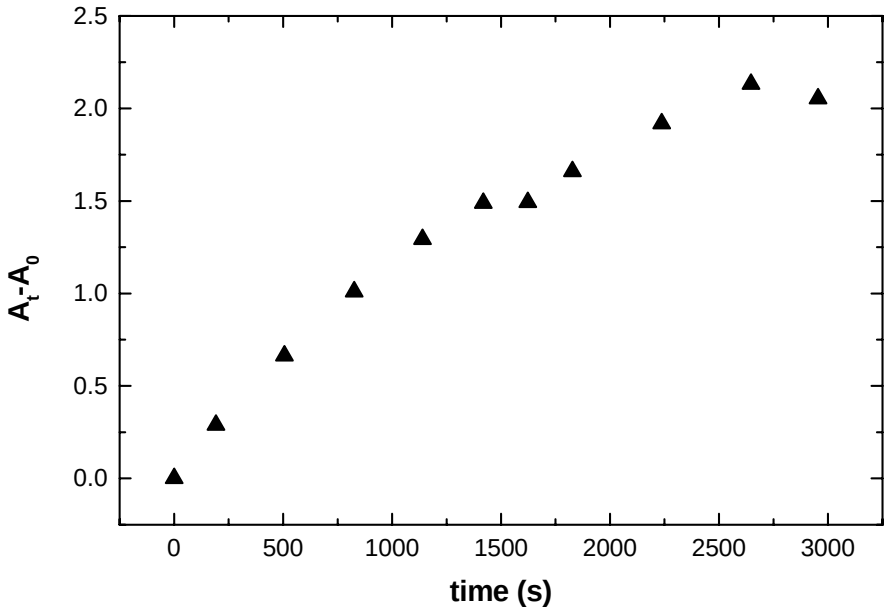

Figure 7.7. Area of O-H stretching vibration peak of *in-situ* ATR-FTIR spectra of methanol diffusing through fluorocarbon film.

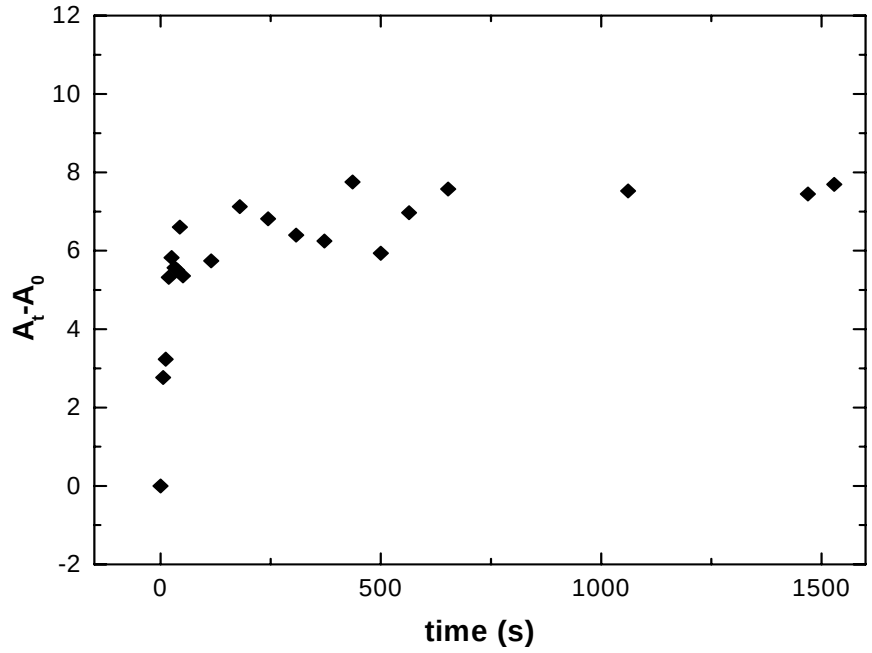

Figure 7.8. Area of O=C=O asymmetric stretching vibration peak of *in-situ* ATR-FTIR spectra of CO_2 diffusing through fluorocarbon film.

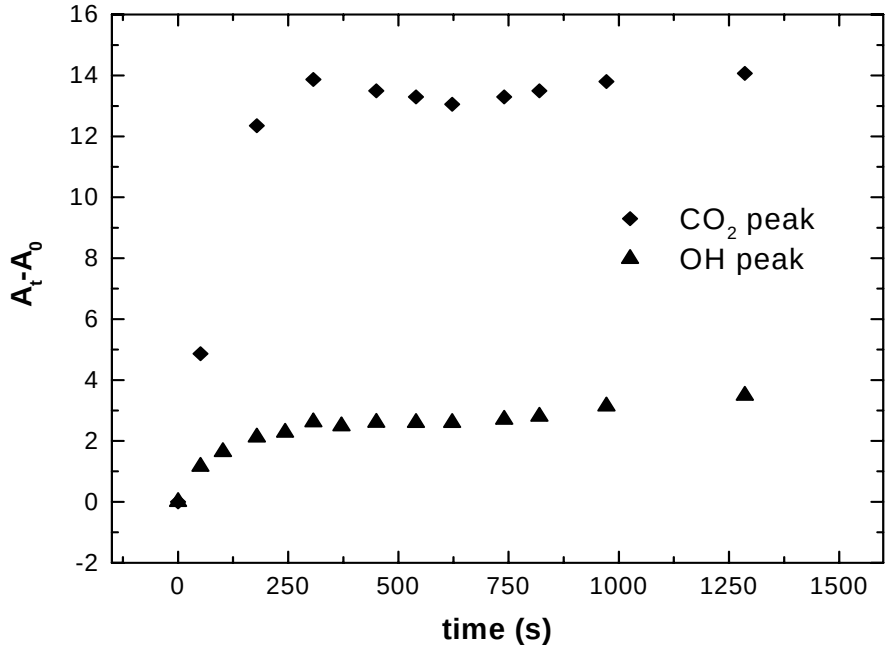

Figure 7.9. Area of CO_2 and methanol peaks of *in-situ* ATR-FTIR spectra during diffusion of CO_2-$TMAHCO_3$-methanol through fluorocarbon film.

7.6 Role of $TMAHCO_3$

$TMAHCO_3$ is a salt of weak acid (H_2CO_3) and a strong base (TMAH); therefore, it acts as a source of OH^- which can attack the interface between the residue and the capping layer. The following equilibria exist in a system comprising CO_2 and a weak base such as $TMAHCO_3$ [191].

$$CO_2 + H_2O \Leftrightarrow HCO_3^- + H^+ \tag{7.4}$$

$$HCO_3^- \Leftrightarrow CO_3^{2-} + H^+ \tag{7.5}$$

$$H_2O \Leftrightarrow H^+ + OH^- \tag{7.6}$$

The concentration of OH^- is, however, very low as the equilibrium in Equation 7.4 shifts towards HCO_3^- in the presence of CO_2. In an aqueous solution, $TMAHCO_3$ has a pH of ~9 or $[OH^-]$ of 10^{-5} M. In pure methanol, the degree of dissociation of $TMAHCO_3$ is expected to be smaller than in water. However, the cleaning solutions do have small amounts of water as the TMAH in methanol solution (from which $TMAHCO_3$-methanol was generated) has ~5.5 wt% water content as estimated by Karl-Fischer titration and this solution was used without purification. This corresponds to ~1.2 moles of water per mole of $TMAHCO_3$.

Since the concentration of OH^- is very low in $TMAHCO_3$ solutions, the solutions are not expected to dissolve phenolic resins (by deprotonation) in the absence of methanol which by itself is a good solvent for PHOST. In fact, aqueous bicarbonate solutions are used to identify phenolic compounds (pKa ~10) by precipitating them while

bases such as NaOH dissolve them. This was confirmed even for the PHOST based resins by dissolution rate monitoring (DRM) studies.

PHOST films 1300 nm thick were spin cast on 4″ Si wafers for these studies. Dissolution of the films in 0.1 N and 1 N aqueous solutions of NaOH, Na_2CO_3 and $NaHCO_3$ were monitored using the multiwavelength DRM apparatus described in Chapter 3; studies were performed at room temperature (RT~20 ^oC) and 70 ^oC. The data analysis was performed using multiwavelength interferometric data analysis software (MIDAS) [129]. The data analysis requires Cauchy parameters of the film to estimate the refractive index; these parameters were measured using ellipsometry. The refractive index of the film was assumed to be constant. For 70 ^oC studies, the wafer was placed on a hot plate, while the solutions were pre-heated to 70 ^oC before dispensing them onto the wafer. Shown in Figure 7.10 is a typical thickness versus time plot for a PHOST film in NaOH, Na_2CO_3 and $NaHCO_3$ at room temperature.

NaOH dissolved PHOST rapidly (52 nm/s). Na_2CO_3 and $NaHCO_3$ swelled the film (by 7.2% and 3.6% respectively) but no dissolution occurred. Swelling of the film is attributed to the formation of a gel layer; a gel layer forms when the solvent species diffuse into the film at a rate faster than that of film dissolution. Such swelling or gel layer formation causes a change in the refractive index of the film (or the gel layer). Hence, the reported thickness values are not accurate. Results from similar experiments with wafer heating and the use of solutions of higher concentrations are summarized in Table 7.3. Dissolution of the film occurred only in NaOH solution, and the dissolution rate was rapid (<1 s) at 70 ^oC or when 1 N solution was used. In Na_2CO_3 solution, the film initially swelled and lifted-off upon prolonged exposure (>1500 s). In $NaHCO_3$ at

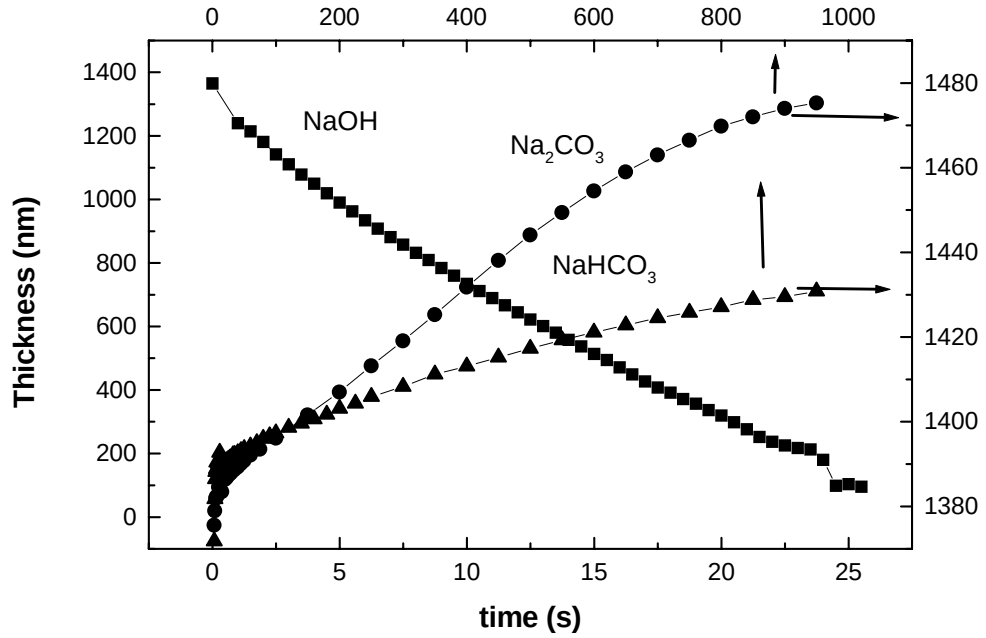

Figure 7.10. Plot of thickness versus time obtained from multiwavelength DRM analysis of PHOST film immersed in NaOH, Na_2CO_3 and $NaHCO_3$.

~20 ^oC, however, the film swelled but no dissolution or lift-off occurred. At 70 ^oC, the film delaminated during a rinse in DIW. This may be due to attack of the interface by the OH^- at higher temperature leading to film lift-off during rinsing. These studies suggest that $TMAHCO_3$-methanol solutions may not remove the soft photoresist underneath the etch residues by a chemical mechanism. However, pure methanol may dissolve the soft resist by physical dissolution. Hence resist (or etch residue) removal by $TMAHCO_3$ can occur only by interfacial attack at elevated temperatures.

Table 7.3. Summary of DRM studies on PHOST film.

Solution	Conc.	Temp.	Rinse?	Final thickness	Comments
NaOH	0.1N	RT	No	0 (52 nm/s)	Film dissolves
NaOH	0.1N	70^{o}C	No	0 (very fast)	Film dissolves
NaOH	1N	RT	No	0 (very fast)	Film dissolves
NaOH	1N	70^{o}C	No	0 (very fast)	Film dissolves
Na_2CO_3	0.1N	RT	Yes	~initial	Film swells
Na_2CO_3	0.1N	70^{o}C	Yes	0	Swells then lifts-off
Na_2CO_3	1N	RT	Yes	0	Swells then lifts-off
Na_2CO_3	1N	70^{o}C	Yes	0	Swells then lifts-off
$NaHCO_3$	0.1N	RT	Yes	~initial	Film swells; no removal
$NaHCO_3$	0.1N	70^{o}C	Yes	>0	Partial lift off during rinsing
$NaHCO_3$	1N	RT	Yes	~initial	Film swells; no removal
$NaHCO_3$	1N	70^{o}C	Yes	0	Film lifts off during rinsing

7.7 Analysis of the crust

The part of the photoresist residue that undergoes cross-linking due to plasma exposure or pre-etch photostabilization may no longer dissolve in methanol during the cleaning or rinsing step (referred to as the 'crust' in this work). Knowledge of the crust thickness and composition can provide an estimate of the cleaning time required based on the diffusion rate of $TMAHCO_3$ or methanol through the crust. For this reason, characterization of undissolved crust was performed using SEM (for thickness) and FTIR (for bonding structure). The crust was collected by immersing the post treated sample in DIW; a Si wafer sample was then used to scoop the floating crust without allowing it to fold or break into fragments. For ATR-FTIR (single reflection) analysis, the crust was collected on a gold film coated onto a silicon wafer.

Cross-sectional SEM micrographs were taken by carefully cleaving through the middle of the crust under liquid N_2. Gold sputtering was then performed to coat the samples to prevent charging by the electron beam and provide good contrast in the micrographs. Shown in Figure 7.11 are the top and cross-sectional views of the crust. Figures a through c are the top view micrographs at magnifications of 24, 700 and 3350 respectively. It is evident that the crust is highly porous even in the areas that were not etched. This may be due to extraction of some of the residues by the cleaning mixtures and to stress induced by CO_2 and the additives. From the cross-sectional micrograph (Figure 7.11d), the thickness of the crust appears to be ~300 nm while the total photoresist residue (in the untreated sample) was ~400 nm. Thus some of the photoresist might have dissolved during the cleaning or the rinsing steps.

The FTIR spectrum of the crust in the wavenumber range 570-4000 cm^{-1} is shown in Figure 7.12. Also included for comparison are the spectra of patterned etch residue (ATR-FTIR) and a film of PHOST-tBOC (transmission). The spectrum of the patterned etch residue was shown only in the range 1350-4000 cm^{-1} because of overlap with the broad Si-O-Si stretching peak of the capping layer at 1010 cm^{-1}. The crust seems to be highly aromatic as indicated by the strong ring C-C stretch at 1500 cm^{-1}, out-of-plane C-

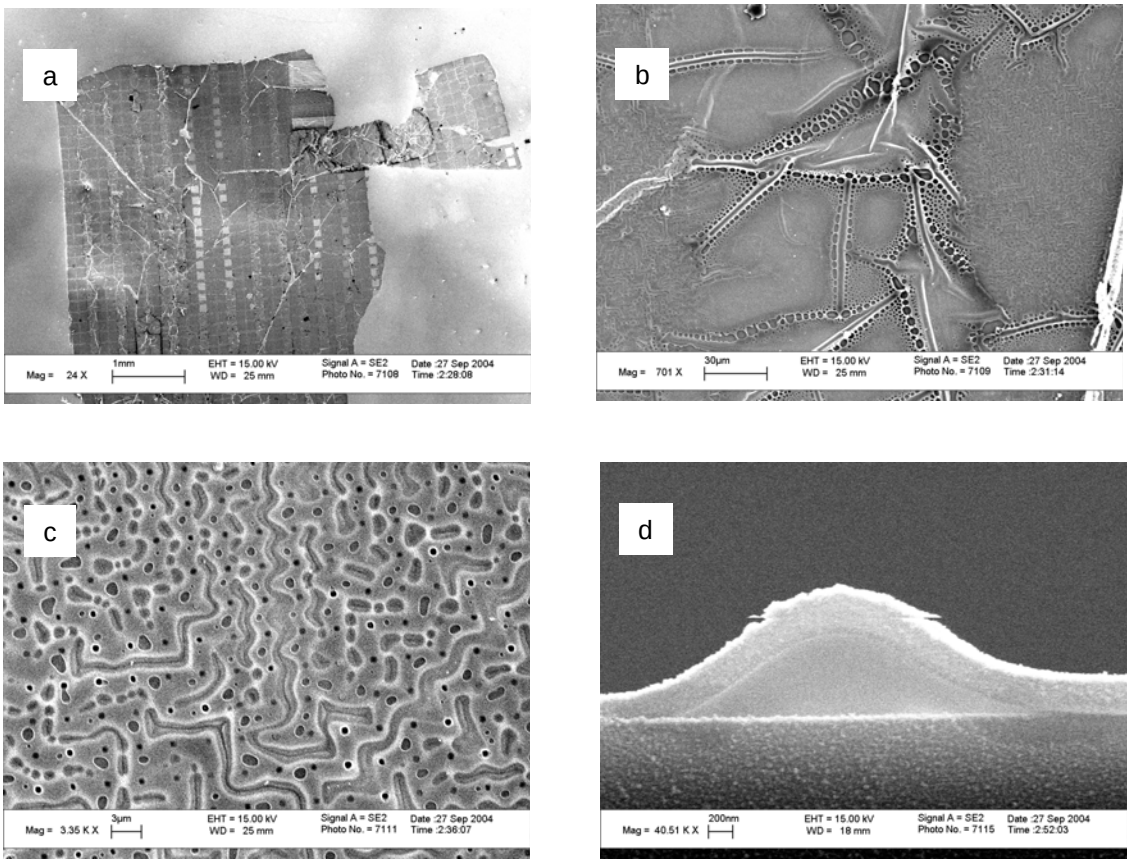

Figure 7.11. SEM micrographs of crust collected from the patterned residue samples: (a), (b), (c) are the plan views at increasing magnifications, (d) is the cross-sectional view.

H deformation vibration (~850 cm^{-1}) and aromatic C-H stretching vibrations (~3030 cm^{-1}). Compared to the etch residue sample, this material has a much lower content of aliphatic C-H groups as shown by smaller alkyl C-H stretching peaks (2850-3000 cm^{-1}) and the symmetric (1370-1390 cm^{-1}) and asymmetric (1440-1465 cm^{-1}) C-H deformation peaks. Compared to the etch residue sample, the C=O stretching vibration peak (~1700 cm^{-1}) is also reduced considerably. This suggests that the crust has undergone significant deprotection; this probably occurred due to processes such as ion bombardment or plasma radiation (discussed in Chapter 3).

As discussed previously, deprotection of the phenolic groups must result in an increased O-H stretching peak (~3350 cm^{-1}), but this was not observed for the crust; in fact, the O-H peak in the crust sample is much smaller than the etch residue or the PHOST-tBOC film. This suggests that the O-H group in the phenolic resin may have undergone condensation with other O-H groups to form a cross-linked network (Figure 7.13). It has been reported that phenol-formaldehyde based resins undergo such condensation at ~300 ^{o}C [192]. Although the film might not have experienced temperatures that high, the plasma atmosphere can provide the necessary activation energy to cause cross-linking. In fact, the increase in asymmetric C-O-C stretching vibration peak at 1330 cm^{-1} (Figure 7.12, top) is consistent with this hypothesis. Thus, the part of the residue that underwent cross-linking due to either plasma exposure or pre-etch hardbaking remains undissolved after the cleaning and rinsing step.

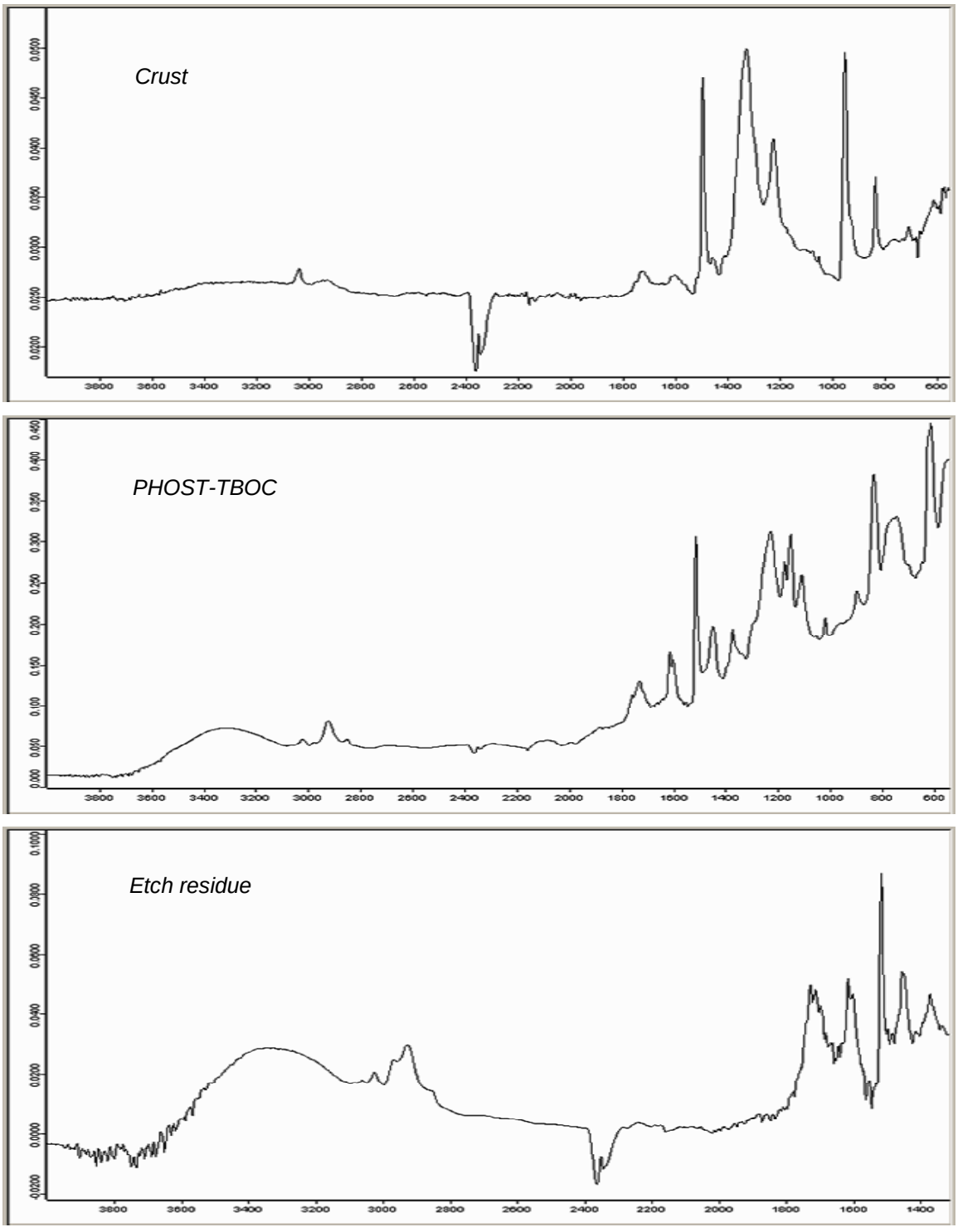

Figure 7.12. FTIR spectra of the crust (top) from the etch residue samples is compared to the spectra of PHOST-tBOC film (middle) and the patterned etch residue itself (bottom).

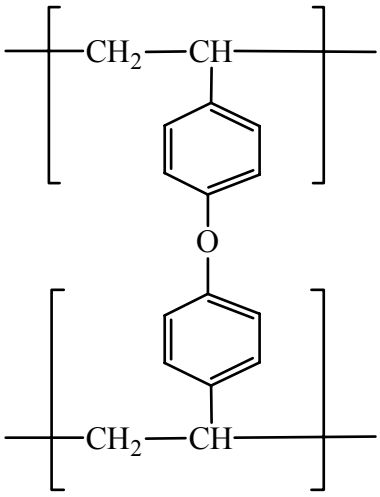

Figure 7.13. The crust from the etch residue samples consists of a cross-linked PHOST network.

7.8 Conclusions

From the analyses of the crust that lifts off the plasma etched samples after CO_2-$TMAHCO_3$-methanol treatments, it is evident that ~300 nm of the photoresist residue has undergone deprotection and cross-linking by an O-H condensation reaction. This observation can explain the incomplete residue removal via dissolution in the cleaning mixtures. Such conclusions are consistent with the fact that, blanket films of PHOST-tBOC with no cross-linking dissolve in the CO_2-$TMAHCO_3$-methanol mixtures.

The $TMAHCO_3$-methanol mixtures diffuse through the crust and attack the interface between the residue and the substrate at elevated temperatures. These mixtures do not cause observable degradation of the capping or dielectric films and their etch rates

are very small. $TMAHCO_3$-methanol (due to OH^- content) also causes some dehydrofluorination of the fluorocarbon crust. At elevated temperatures when the rate of interfacial attack is sufficiently large, diffusion of the cleaning species to the interface may be rate limiting. In this study, plasma deposited fluorocarbon films were used to study diffusion of the cleaning species through the fluorocarbon crust on the surface of the residues. CO_2 enhances the transport of these species into the film by swelling and increasing the free volume in the film. The additives may also dissolve some of the unmodified photoresist underneath the crust.

Unlike $TMAHCO_3$, TMAH (or other strong bases) can dissolve the PHOST based resin by chemical reaction. Hence, TMAH cleaned the samples even at room temperature. Because it can dissolve even moderately cross-linked parts of the residue, the remaining residue degraded into smaller fragments (no continuous crust such as in Figure 7.11 was obtained).

CHAPTER 8

EVALUATING THE COMPATIBILITY OF CO_2-$TMAHCO_3$-METHANOL MIXTURES WITH A POROUS LOW DIELECTRIC FILM

8.1 Introduction

While the semiconductor industry continues to scale down devices for better performance, lower power consumption and higher packing density, there is a necessity to reduce the interconnect delay and cross-talk between adjacent metal lines. The industry achieves these objectives by increasing the conductivity of metal lines and lowering the permittivity of the dielectric medium between them. Hence SiO_2 (*k* or ε=3.9) is being replaced as the intermetal dielectric with newer materials that have lower dielectric constant ($\varepsilon = \varepsilon_o \varepsilon_r$) and also satisfy other requirements such as low moisture absorption, good mechanical, thermal, and chemical stability and ease of integration into fabrication process. The relative permittivity ε_r of a molecule is given by the Debye equation [135]:

$$\frac{\varepsilon_r - 1}{\varepsilon_r + 2} = \frac{N}{3\varepsilon_o}\left(\alpha_e + \alpha_d + \frac{\mu^2}{3kT}\right) \tag{8.1}$$

where, α_e represents the electronic polarization, α_d represents the distortion (or ionic) polarization, and μ is the orientation polarizability (arising from permanent dipoles) of the molecule.

Two approaches are taken to lower the dielectric permittivity of the medium. The first approach involves a decrease in the polar or polarizable bonds (related to μ). This is achieved by incorporating organic or fluorinated groups into the material. A variety of dielectric films have been developed through this approach e.g. fluorine doped SiO_2 [193], carbon doped SiO_2 [194], hydrocarbon [195] or fluorocarbon [196] polymers. Dielectric constants below 3 have been achieved by doping SiO_2 with C or F. For a polytetrafluoroethylene (PTFE) type film, *k* as low as 1.93 was obtained [197]. The second approach to lowering the dielectric constant involves lowering the density of the medium (N in Equation 8.1). Although incorporation of bulky organic groups lowers the film density to a certain extent, incorporation of pores is necessitated by the requirement for ultra low-*k* ($k< 2.1$) films for sub 45 nm generation devices slated for production in the year 2010 [2]. Porosity in these films can be either constitutive or subtractive. Constitutive porosity arises as a result of a porous backbone in the film (e.g. methyl silsesquioxane) and the pore size is generally <2 nm (microporous, according to IUPAC nomenclature). Subtractive porosity is generated either by breaking down sacrificial porogen molecules or by evaporating solvent in the film. The mean pore size is generally >2 nm (mesoporous). Depending on the weight percent loading of the porogen, the porous structure can be interconnected (open) or closed.

Methyl silsesquioxane (MSSQ) is a dielectric film with a CH_3-$SiO_{3/2}$ backbone structure [135]. Because of the bulky -CH_3 groups and the lower polarizability of Si-CH_3 bonds compared to Si-O bonds, MSSQ has a lower dielectric constant than SiO_2. The cage or ladder structure of the film (Figure 8.1) results in a microporous structure. Additional porosity is incorporated by a subtractive approach, thereby lowering the *k* to

as low as 1.9 with 30 wt% porogen loading [198]. Thermally labile organic polymers are used as sacrificial materials which phase separate, degrade, and volatilize upon heating, leaving behind pores in the dielectric film. Commercially available dielectric films such as JSR's LKD 5109™ are based on this porous MSSQ structure.

A number of integration challenges have to be overcome before these porous low-*k* films can be included in device fabrication. One such challenge is to be able to remove post plasma etch residues from these films without causing damage or modifying the dielectric constant of the film. The cleaning mixtures must be able to enter the small pores and remove residues deposited inside them [37] without leaving behind residual solvent. Incomplete removal of either the residues or the solvent may increase the effective dielectric constant of the film and cause corrosion of the metal lines.

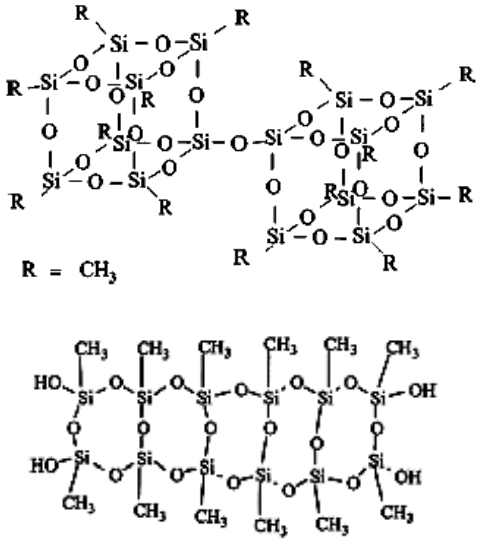

Figure 8.1. Cage (top) or a ladder (bottom) structure of methyl silsesquioxane [135].

In this chapter, compatibility studies of CO_2-$TMAHCO_3$-methanol cleaning mixtures with a porous low-*k* dielectric material are reported. X-ray photoelectron spectroscopy (XPS) and Fourier transform infrared spectroscopy (FTIR) studies indicated no chemical modification of the CORAL™ low-*k* dielectric film (non porous) present in the etch residue samples [199]. However, porous dielectric materials may be more susceptible to degradation by chemical additives or by the high pressures than are the plasma deposited dielectrics. Because of their porosity, the additives can penetrate the porous material and modify the film. Because of their enhanced mass transport properties, high pressure CO_2 based fluids can penetrate the pores faster than aqueous or organic solvents. Hence, the impact of these high pressure fluids on the pore structure and composition of a porous low-*k* material film was investigated.

The subject of pore degradation in these films during plasma ashing has been studied previously [136], but the effect of cleaning solutions on pore structure has not been investigated. Even though dielectric constant is commonly used as an indicator to monitor the integrity of these films, it does not detect changes due to chemical attack or pore size modification. A pore size measurement technique in conjunction with composition (bonding information) can give a more accurate picture of film modification. Hence, positronium annihilation lifetime spectroscopy (PALS) was used to study the pore structure of the porous MSSQ film before and after various high pressure treatments.

8.2 Experimental

The MSSQ samples (~400 nm on silicon substrate; JSR's LKD 5109™) were supplied by Novellus Systems, Inc. Two kinds of measurements were made on MSSQ samples treated under different sets of conditions: % Ps formation and mean pore size. The percentage of positrons forming Ps (free Ps and trapped Ps) is dependent on the chemistry of the film. Certain molecules (such as CCl_4) present in the film inhibit Ps formation by capturing free electrons that are captured by positrons to form Ps [142]. Similarly, certain molecules such as naphthalene can act as a positronium formation enhancer by scavenging holes or free radicals. To estimate pore sizes, it is desirable to have a high intensity of trapped o-Ps for greater precision. For MSSQ films with ~29% porosity, the percentage of positrons leading to formation of trapped o-Ps is <50%. The remaining Ps diffuse out of the film into the vacuum atmosphere and decay at vacuum lifetime (140 ns) and, therefore, cannot provide information about the film. Hence, for pore size measurements, a thin film of SiO_2 or aluminum was deposited onto the MSSQ to confine o-Ps to the film. The deposited layer must be thin in order for the positrons to penetrate and implant in the film underneath. A 70 nm layer of SiO_2 (by RF sputtering) or aluminum (DC sputtering) has been used for this purpose. Care was taken to prevent the film from being heated during the deposition process because this may lead to diffusion of sputtered material into the pores. Sets of samples (one with the capping layer and one without) were sent to the University of Michigan (Prof. David Gidley) for PALS analyses. The instrument configuration and the data analysis procedure were described in Chapter 4. The lag time between sample generation and analysis was usually between 7 and 10 days.

8.3 Results and discussion

Transmission FTIR was first used to determine if MSSQ underwent detectable changes in bonding structure after exposure to the cleaning mixtures. The sample was exposed to CO_2-$TMAHCO_3$-methanol under the following conditions: single phase, 3200 psi, 70 ^oC, 45 min. The sample was then rinsed in methanol and dried under vacuum. The FTIR spectrum of this sample was compared to the spectrum of an untreated sample; results are shown in Figure 8.2. Also included in the figure is the spectrum of a sample exposed for 1 min to an O_2 downstream plasma used for 'ashing' photoresists.

Clearly, the sample exposed to the single phase mixture did not undergo detectable changes in bonding structure. The sample exposed to O_2 ashing underwent oxidation; the CH_3 groups in the MSSQ structure were oxidized leaving behind Si-OH moieties in the film. This is evident from the decrease in C-H stretching vibration peaks (ii, 2900-3000 cm^{-1}) and in the symmetric CH_3 deformation peak around 1250 cm^{-1} (iii), combined with a corresponding increase in the O-H stretching vibration peak (i, ~3500 cm^{-1}). This renders the film hydrophilic and increases the dielectric constant of the film. Thus, oxidizing plasmas may not be used to remove etch residues from porous MSSQ based dielectrics.

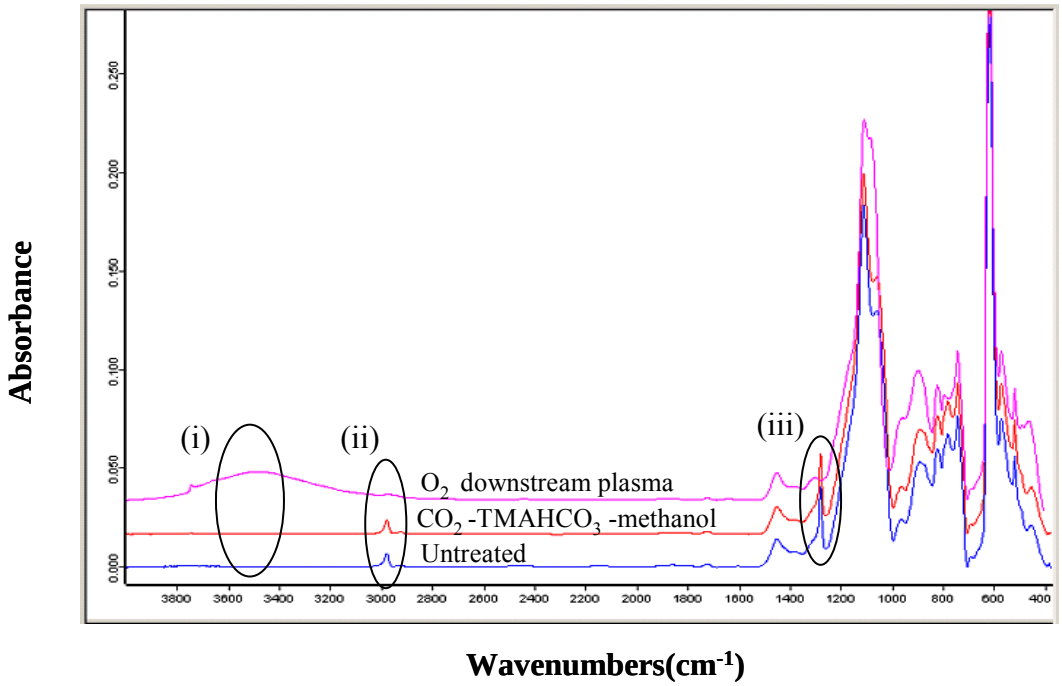

Figure 8.2. FTIR spectra comparing porous MSSQ sample after CO_2-$TMAHCO_3$-methanol treatment and O_2 downstream plasma exposure to the untreated film.

8.3.1 Samples without capping layer

Another set of samples processed under the same conditions were analyzed by PALS. In addition to the above samples, a sample treated in CO_2 alone (3000 psi, 70 ^oC, 45 min) and a sample treated in CO_2-$TMAHCO_3$-methanol under two phase conditions were also included for comparison. Considering the 400 nm nominal thickness of the samples, three beam energies, 1.1, 2.1, and 3.1 keV, were chosen to depth-profile the films. These beam energies correspond to mean implantation depths of 30 nm, 90 nm, and 170 nm for a hypothetical film density of 1.0 g/cm^3 (these depths will be

proportionately deeper for lower actual film density and vice-versa). The PALS fitting results for each positronium (Ps) lifetime and corresponding intensities are listed in Table 8.1. The samples were treated as follows: A: CO_2 only, 3000 psi, 70 ^oC, 45 min; B: CO_2-$TMAHCO_3$-methanol under two phase conditions, 3000 psi, 70 ^oC, 45 min; C: CO_2-$TMAHCO_3$-methanol under single phase conditions, 3200 psi, 70 ^oC, 45 min; D: $TMAHCO_3$ in methanol (beaker), 50 ^oC, 30 min; E: downstream O_2 ashing for 1 min.

I_{Ps} is the percentage of positrons forming Ps which decay with lifetimes corresponding to vacuum (I_{vacuum}) and micropore environments (I_{micro}). The lifetimes of the Ps were fitted to 4 lifetime components; the best fits were obtained at higher beam implantation energies where greater numbers of Ps were generated. Hence, the lifetimes and the corresponding intensities for the individual components were not reported for 1.1 keV. The shortest lifetime component (~0.5 ns) was mainly due to positrons annihilating within the material and is hence uninteresting, although this peak marks t=0 in the data analysis. There were 3 physically interesting Ps lifetime components observed at approximately 1.5 ns, 10 ns, and 140 ns. The last of these values is the lifetime of Ps in vacuum after diffusing through interconnected pores and escaping through the film surface into vacuum. The shorter lifetimes are related to Ps in micropores (2-7 ns is a typical value) and the 10-12 ns component suggests that some Ps annihilate in mesopores before escaping into vacuum. There was no lifetime component corresponding to mesopores (~50 ns) indicating that the samples have a high degree of mesopore openness (interconnectivity).

In films A through D, the majority of Ps annihilated with the vacuum lifetime. The mesopore size could not be determined because of this reason. Typical of LKD

5109™, the pores were highly interconnected and Ps readily diffused through the mesopore network and escaped through the film surface into vacuum. From Table 8.1, it is noticeable that the processing of A-D films produced a gradual decrease in the fitted Ps intensities (Figure 8.3) at all beam energies. This observation appears consistent with an overall decrease in the Ps formation intensity throughout the film and is not consistent with a depth dependent pore morphology change, such as pore collapse or surface densification of the film. Had the vacuum Ps intensity decreased with a concomitant increase of Ps intensity in micropores, this would be an indication of densification. The fraction of Ps that escaped through the pore network (I_{vacuum}/I_{Ps}) remained essentially constant, suggesting that the mesopore size was unaffected. The small reduction in Ps formation by processing suggests that the chemistry of the film has changed. In sample E, however, the vacuum Ps intensity decreased while the intensity of Ps decaying with micropore lifetimes increased. This suggests that the mesoporous structure has partially collapsed – supporting the conclusions from the previous section that oxidizing plasmas are not compatible with low-*k* materials that have a carbon doped SiO_2 structure.

Table 8.1. PALS lifetimes and corresponding Ps intensities for porous MSSQ samples treated under different conditions.

Sample	Energy (keV)	Component 1		Component 2		I_{vacuum} (%)	I_{Micro} (%)	I_{Ps} (%)
		τ_1 (ns)	I_1 (%)	τ_2 (ns)	I_2 (%)			
Untreated	1.1	/	/	/	/	46	5	47
	2.1	1.3±0.2	2.3±0.4	13.3±0.8	2.9±0.1	43	5	46
	3.1	1.4±0.1	4.0±0.3	11.8±0.7	3.4±0.1	38	7	44
A	1.1	/	/	/	/	39	4	39
	2.1	1.5±0.2	1.9±0.2	12.5±0.8	2.5±0.1	35	5	38
	3.1	1.6±0.1	3.3±0.2	12.3±0.8	3.0±0.1	32	6	37
B	1.1	/	/	/	/	38	5	39
	2.1	1.4±0.1	2.5±0.3	12.1±0.6	2.8±0.1	35	5	38
	3.1	1.3±0.1	4.8±0.4	10.1±0.5	3.3±0.1	30	8	37
C	1.1	/	/	/	/	36	4	36
	2.1	1.2±0.1	2.9±0.6	12.4±0.7	2.6±0.1	32	5	35
	3.1	1.2±0.1	4.6±0.7	10.7±0.5	3.1±0.1	28	7	34
D	1.1	/	/	/	/	35	5	36
	2.1	1.1±0.1	3.4±0.8	11.6±0.7	2.2±0.1	31	6	35
	3.1	1.2±0.1	5±2	9.0±0.5	2.5±0.1	28	7	34
E	1.1	/	/	/	/	27	4	27
	2.1	2.1±0.2	2.0±0.2	10.6±0.5	3.2±0.1	23.5	5.2	27
	3.1	1.3±0.1	7±1	9.7±0.3	3.8±0.1	19.4	10.8	28

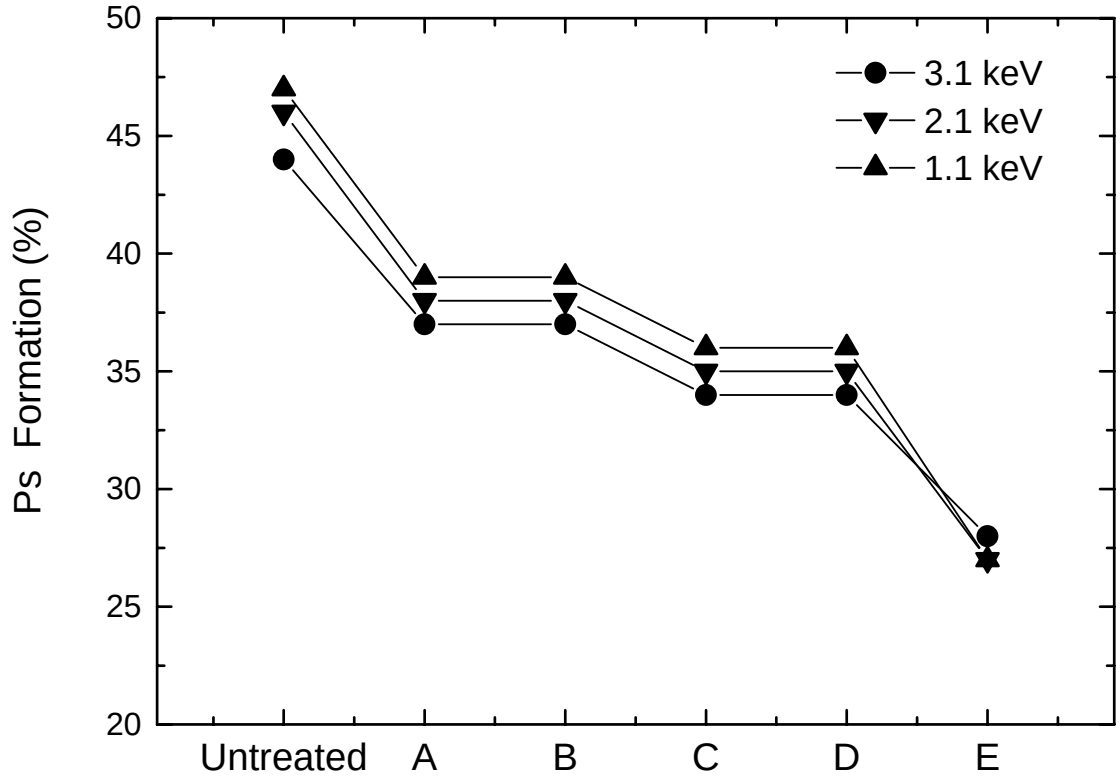

Figure 8.3. Ps formation intensity in porous MSSQ samples with various treatments (see Table 8.1).

From Figure 8.3, the biggest reduction in the Ps formation intensity (outside of the 'ashed' sample) occurred in a sample treated in CO_2 alone. This suggests that CO_2 (or the high pressure) treatment rather than the co-solvent additives may have the most prominent effect on the Ps intensity reduction. This observation was verified by exposing a series of samples to CO_2 for different times and measuring the resulting Ps formation intensities. Shown in Figure 8.4 are the Ps intensities from MSSQ samples exposed to CO_2 at 70 ^oC for 5 min, 20 min, 40 min and at room temperature (RT) for 60 min. Even a 5 minute exposure of the sample to CO_2 decreased the Ps formation by 6% (absolute).

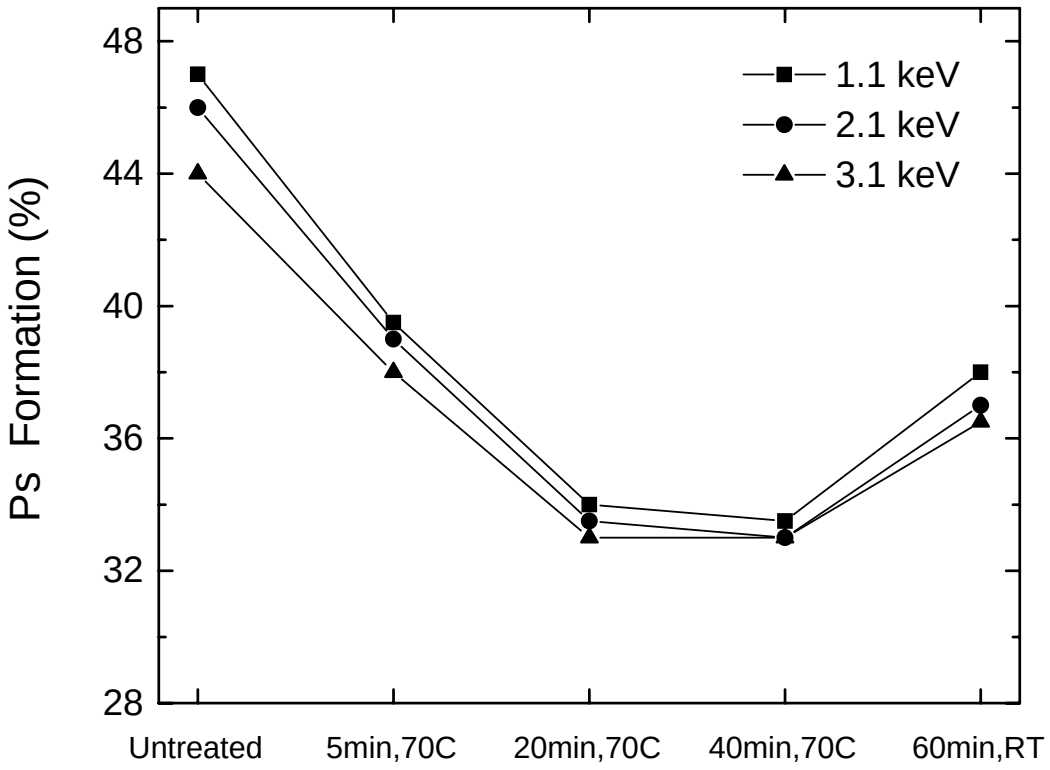

Figure 8.4. Ps formation intensity in porous MSSQ samples exposed to CO_2 under different conditions.

Longer CO_2 exposures further decreased the Ps intensity, but the effect appeared to saturate when the exposure time was more than 20 minutes. However, treatment at a lower temperature (RT) produced less suppression of the Ps formation.

8.3.2 Samples with capping layer

In order to measure the pore sizes in the film, a 70 nm thick SiO_2 was deposited onto the samples by radio frequency (RF) sputtering. The SiO_2 capping confines Ps

inside the film, resulting in a Ps lifetime characteristic of the pore size. For the capped samples, only one beam energy, 4.1 keV, was used to measure the positronium lifetime inside the porous network of the film. The range of mean pore sizes estimated from the capped samples is shown in Figure 8.5. Samples A through D demonstrate essentially unchanged pore size, except a slight decrease observed for sample C. Small changes in pore sizes may also result from local non uniformities in low-*k* sample processing (MSSQ curing). The 50 ns Ps lifetime (i.e., 2.8 nm in cylindrical diameter) was in good agreement with past results on LKD 5109™ [146]. Any physical (only) damage due to the cleaning process (such as pore collapse) may decrease the pore size and change the relative fraction of Ps annihilating in the micropores and mesopores, but will not influence the total Ps formation in the film. Therefore, the decreased Ps formation may be due to changes in the film chemistry resulting from the cleaning process. This conclusion is better supported if the overall porosity was confirmed to be unchanged using an alternative technique such as specular x-ray reflectivity or ellipsometry since PALS is not an absolute porosity measurement but a pore size and pore connectivity metrology [200].

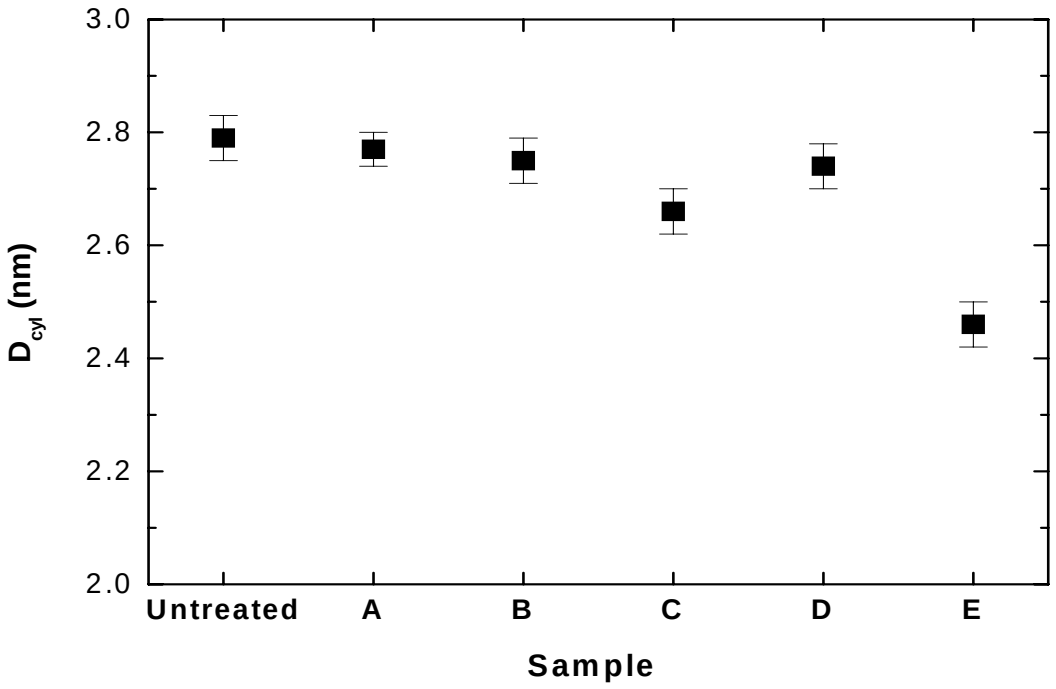

Figure 8.5. Ranges of pore sizes measured on porous MSSQ samples with various treatments (see Table 8.1).

8.3.3 Porosity from variable angle spectroscopic ellipsometry

In order to determine the overall porosity of the films, ellipsometry was used. The interaction of the polarized light with a porous material can be described by an effective medium approximation (EMA) model [134]. In this model, the optical constants of a composite material can be calculated from the properties of the individual components using a specific mixing rule. For example, the Maxwell-Garnett EMA assumes that a material B, having volume fraction, f_B, is mixed into a host material A (f_A=1-f_B) in the form of spherical inclusions. The optical properties of the individual

components can be described using a Cauchy layer when they are dielectrics or polymers [134]. There are three fit parameters for an EMA model for a porous film: optical constants of the host material, void fraction (or total porosity) and film thickness. Voids are modeled as a material with n=1 and k=0.

Variable angle spectroscopic ellipsometry (VASE) scans were collected on a predetermined spot on the sample (LKD 5109™) before and after exposure to the cleaning mixtures. High resolution (step size 2 nm) data was collected over the wavelengths 800-1100 nm and at three angles 65, 70, and 75 degrees. For data analysis, the effective medium approximation (EMA) was used, which modeled the film as a combination of a Cauchy film and voids. Data over 800-1100 nm was used (where the absorption was negligible) to estimate the Cauchy parameters for the host matrix (non porous MSSQ), film thickness and the void fraction. The resulting parameters for the host matrix were consistent with other studies on MSSQ. The results are summarized in Table 8.2.

A small increase (~1%) in overall porosity of the film was observed upon very fast depressurization of CO_2 (<30 s from 3000 psi to atmosphere). However, this increase may not be significant considering the variation in the porosity of the untreated samples. The porosity of the film increased to a greater (~1.6%) extent after treating the film in $TMAHCO_3$-methanol solution in a beaker (sample D). The etch rate is also highest with this mixture suggesting that the liquid may be attacking the Si-O bonds in the matrix, thus increasing the porosity of the film.

Table 8.2. Porosity and thickness of MSSQ samples before and after $TMAHCO_3$-methanol based treatments.

	Before treatment		After treatment	
Sample	Thickness(nm)	Void%	Thickness(nm)	Void%
A (CO_2 alone, very fast depressurization)	403.93	28.1	404.22	29.1
B (CO_2 alone, very slow depressurization)	404.54	28.2	404.9	28.1
C (CO_2-$TMAHCO_3$-methanol mixture)	408.13	27.8	408.01	28.3
D ($TMAHCO_3$-methanol)	405.82	28.6	405.41	30.2

8.4 Conclusions

FTIR, PALS and VASE techniques were used to evaluate the compatibility of $TMAHCO_3$-methanol based mixtures with a porous low-*k* material (porous MSSQ). FTIR indicated no change in the bonding structure of the film after it was exposed to the cleaning mixtures. The etch rate of the film in these mixtures (measured using ellipsometry) was also negligible. Pore size measurements using PALS revealed a small decrease (~5%) in the size of the mesopores when treated in the CO_2-$TMAHCO_3$-methanol mixture. However, the pore size was not affected by depressurization rate after the cleaning process, or the rinsing solvent used (DIW and methanol were tested). The percentage of Ps annihilating in the mesopores remained the same suggesting that the decrease in mesopore size may be very small if any. Overall porosity measurements from VASE also revealed no significant change in the porosity which means that the size

of the micropores, in addition to the mesopores, remain unchanged.

However, Ps formation intensity in the film decreased after these treatments; even a CO_2 treatment alone caused a decrease in Ps formation in the film. The contaminants or residual solvents (methanol, water vapor) from previous experiments in the high pressure cell may be responsible for the decrease in Ps formation. Although the system was cleaned (purged with DIW, then methanol, and dried with $scCO_2$) before each run, cross contamination from residues remaining in the valves, mixing chamber, or other fittings can affect the results. In order to avoid such issues, the volume inside the cleaning system must be minimized and periodic replacement of the fittings and tubing is recommended. It has to be determined if such a slight change in pore chemistry has any influence on the electrical characteristics of the dielectric film. In particular, the dielectric constant, dielectric loss and breakdown voltage of the film should be measured after the treatment.

CHAPTER 9

SUMMARY AND RECOMMENDATIONS FOR FUTURE WORK

9.1 Summary

In this work, a CO_2 based single liquid phase mixture was developed for post plasma etch residue removal. The cleaning performance of the mixture was studied as a function of process variables such as temperature, time, composition of the additives and phase state of the mixture. Mechanistic studies were performed that provided better understanding of the cleaning process; the role of additives and the effect of process variables was clarified by these studies. Compatibility studies were performed to ensure that the cleaning mixtures can be integrated with materials used in current integrated circuit (IC) processing.

First cleaning studies were performed in a beaker (atmospheric pressure) to evaluate potential additives to CO_2. These additives were chosen based on specific applications from the literature and based on the chemical nature of the residues that must be removed. Patterned samples with plasma etch residues were procured from the industry to provide a realistic basis for testing the cleaning solutions. Techniques such as x-ray photoelectron spectroscopy (XPS), Fourier transform infrared (FTIR) spectroscopy, and scanning electron microscopy (SEM) were used to characterize these samples. By comparing the SEM micrographs and the surface atomic composition from XPS, it was concluded that an average Si>22% would mean that no bulk residues remain on the

sample (considered 'clean'). Using XPS sputter depth profiling, the thickness of the fluorocarbon residue on the surface of these samples was estimated to be ~8 nm which is slightly higher than values reported in the literature for similar residues (measured using angle-resolved XPS).

In the beaker studies, none of the organic solvents studied (such as methanol, acetone, N-methyl-2-pyrrolidone etc.) removed the residues. This suggests that the photoresist residue has undergone cross-linking due to the plasma etching process. Sometimes, the photoresist is hardbaked under deep UV radiation to cross-link the photoresist to impart higher stability to the photoresist in the plasma etch atmosphere. In that case, solvents may not dissolve the film by physical dissolution. Hence, basic additives were explored since the bases can react with the acidic phenolic moieties in the residue to promote dissolution. Amines (such as hydroxylamine, diethylamine) which are common constituents of commercial photoresist removers, were effective in photoresist and residue removal only upon addition of water. These and similar studies with solution of various salts indicated that only OH^- containing solutions are effective in removing the residues. Because it is used extensively in the IC industry (as an etchant and a photoresist developer) and because it is available as a solution in methanol, 25 wt% tetramethylammonium hydroxide (TMAH) in methanol solution was chosen as the co-solvent to CO_2.

The acid-base reactions between CO_2 and TMAH were studied by bubbling CO_2 through TMAH-methanol solutions. Titrations were performed to identify the reaction products. TMAH reacts with CO_2 to form TMA_2CO_3 which precipitates in methanol. Upon continued reaction, the solute ($TMAHCO_3$ eventually) re-dissolves and the solution

becomes transparent. Even the weakly basic $TMAHCO_3$ solution was effective in removing the residues although higher temperatures ($\geq 50\ ^oC$) were required.

Based on the phase behavior studies by G. Levitin et al. [179], the $TMAHCO_3$-methanol solution was diluted with methanol to formulate a single phase CO_2-$TMAHCO_3$-methanol mixture for residue removal. The cleaning studies were performed in a table top high pressure system equipped with dual high pressure pumps and an optical window for *in-situ* observation of the cleaning process. The system was designed to run under flow conditions and was optimized for minimal interference from additives condensing on the sample surface. After the minimum amount of $TMAHCO_3$ necessary to remove residues in the CO_2 phase was identified, a series of experiments was performed to compare the performance of single phase mixtures with two phase mixtures (where vapor and liquid phases coexist). The results suggested that because of more efficient use of the additives and enhanced transport properties of the single phase mixtures, residue removal progressed at faster rates and to a greater extent when single phase mixtures were used. In all cases, temperatures above 50 ^oC were necessary to achieve complete cleaning. Following these high pressure treatments, a solvent rinse step is necessary during which undissolved residue (referred to as the 'crust') lifted off the sample surface.

Next, mechanistic studies were performed to gain insight into how cleaning proceeds and to determine the rate limiting factors. The possible mechanisms investigated were: dissolution of the unmodified resist underneath the crust, chemical attack of the crust, and undercut of the residue. To perform these studies, blanket films of model residues were generated to act as surrogates for the fluorocarbon crust (the top

part of the residue with fluorine incorporation) and the unmodified photoresist. A parallel plate plasma enhanced chemical vapor deposition (PECVD) system was used to deposit thick (~500 nm) fluorocarbon films to emulate the fluorocarbon crust. Parameters such as plasma power, substrate temperature and precursor gases (C_4F_8, O_2, Ar) were tailored to deposit cross-linked films that are resistant to solvent dissolution and have similar bonding structure to that of the fluorocarbon etch residues. Blanket films of poly 4-hydroxystyrene (PHOST) protected by tert-butoxy carbonyl (PHOST-tBOC) groups were used to study dissolution rates of unmodified resist in the cleaning mixtures. In addition, PHOST-tBOC film was exposed to $Ar/C_4F_8/O_2$ reactive ion etch (RIE) plasma to generate planar residues that are similar to the patterned samples.

Dissolution rate studies using multiwavelength interferometry revealed that aqueous solutions of $TMAHCO_3$ do not dissolve PHOST based photoresist resin because of the latter's weak acidity. However, $TMAHCO_3$-methanol solutions can dissolve the photoresist because methanol is a good solvent for PHOST type resins. Hence, if the underlying soft (unmodified) resist is dissolved by this mechanism, the crust can lift-off from the samples. However, no evidence of this mechanism was observed since methanol (or CO_2-methanol) does not remove the residues even at elevated temperatures where diffusion rates are higher. In fact, analysis of the crust that remains after CO_2-$TMAHCO_3$-methanol treatment indicated that <25% of the residue dissolved during the cleaning/rinsing steps. FTIR spectroscopy indicated that the crust consists of highly cross-linked PHOST moieties which do not dissolve in methanol.

Next, the interaction of the cleaning mixtures with the fluorocarbon crust was studied. The blanket model films were exposed to cleaning solutions and changes in

composition and bonding structure monitored. From the XPS and ATR-FTIR studies, it appears that the $TMAHCO_3$-methanol (or CO_2-$TMAHCO_3$-methanol) mixtures cause some dehydrofluorination of the residue at elevated temperatures. Depth profiles of composition of C, O, and F (determined by ARXPS) showed that the depth of modification of the residue is on the order of 6 nm after a 30 min treatment at 50 ^oC in a beaker experiment. The film morphology after treatment suggests that these mixtures also extract residue fragments from the film. However, the extent of modification of the film by these mixtures was not sufficient to remove it completely. In the patterned residue samples, since the fluorocarbon crust is thin (~8 nm), the cleaning mixtures may penetrate it fully; however, since the underlying resist is cross-linked, the removal does not occur immediately.

The next mechanism investigated was residue removal by interfacial chemical attack. This mechanism was evident in the fluorocarbon film treatments, where the film begins to lift-off from the sample edges upon prolonged (≥30 min) treatment in $TMAHCO_3$-methanol mixtures. The fluorocarbon crust in the etch residue samples is thinner (~8 nm compared to ~500 nm for the model films); hence, the additives can diffuse through the crust and the cross-linked resin before attacking the interface. Also, fluorocarbon films deposited on a ZnSe substrate (used as an ATR crystal) were not removed by $TMAHCO_3$-methanol mixtures even after 2 hrs of treatment at 50 ^oC which suggests that these mixtures are effective only for residues with interfaces that can be attacked. Etch rate studies showed that $TMAHCO_3$-methanol mixtures etch the SiO_2 (capping layer in the patterned samples) at 0.55 nm/hr at 50 ^oC and negligibly at room temperature. This explains why higher temperatures are necessary for cleaning. This

mechanism was also substantiated by the inteferometric studies: PHOST films delaminated after treatment in $NaHCO_3$ at 70 ^oC but not at room temperature. The interfacial attack may occur by cleavage of the Si-O bond by OH^- ions. The concentration of these ions, even though very small (10^{-5} M in aqueous solution and lower in non-aqueous solvents such as methanol and CO_2), may be sufficient to delaminate the film. On the other hand, much higher concentration of OH^- would be required in order to dissolve the photoresist by deprotonation of the large concentration of phenolic groups. The interfacial attack may also be promoted by the F^- ions that are generated by dehydrofluorination of the fluorocarbon residue by the cleaning mixtures.

The role of CO_2 in the cleaning mixtures is to provide enhanced transport of additives to the film interface. CO_2 may also swell the residues due to its affinity to fluorocarbon and carbonyl moieties in the residue. The accelerated transport of additives in the presence of CO_2 was substantiated by ATR-FTIR studies; diffusion of cleaning species through the fluorocarbon crust was monitored *in-situ*. Fluorocarbon films coated on Si crystals were exposed to the cleaning mixture in a high pressure ATR-FTIR cell. Methanol in the $TMAHCO_3$-methanol solution diffused through the crust and attained a steady state after 2500 seconds whereas, in CO_2-$TMAHCO_3$-methanol mixtures at 1000 psi, methanol diffused through the crust within 250 seconds. Thus, for mixtures at identical temperatures and concentrations of additives, CO_2 based mixtures would facilitate faster removal. However, the processing time in these mixtures is substantially higher than liquid mixtures when considering the time needed to pressurize, purge, and depressurize the system. From an industrial point of view, these times have to be minimized to exploit the kinetic advantages offered by CO_2 based cleaning.

Etch rate and compositional measurements confirmed that cleaning mixtures are compatible with plasma deposited C-doped SiO_2 (CORAL™) and porous methyl silsesquioxane (MSSQ, LKD 5109™). Positronium annihilation and ellipsometry studies after exposing the porous MSSQ samples to these mixtures revealed very small changes in mesopore sizes and overall porosity of the films. A small drop in Ps formation probability was observed after these treatments; electrical tests are needed to determine if these observations affect the dielectric properties of the film.

9.2 Recommendations for future work

Further kinetic studies are needed to determine the rate limiting step during CO_2-$TMAHCO_3$-methanol cleaning. Diffusion studies such as the ones reported in this work should be performed using the cross-linked PHOST resin since it constitutes the majority of the etch residue. Such cross-linked PHOST film can be formed by baking PHOST resin under deep ultraviolet (DUV) radiation. The extent of cross-linking can also be varied and cleaning studies performed to determine if diffusion of the additives through the cross-linked photoresist or interfacial chemical attack is rate determining. These studies can be performed at different temperatures to gauge the relative importance of the diffusion rates with respect to the overall cleaning rate.

Diffusion coefficients can also be determined for the cleaning species in the fluorocarbon crust and cross-linked resin. Knowledge of the thickness of these layers would then allow prediction of the time required for the additives to penetrate the etch residue and from this, the time required to clean the samples. Diffusion coefficients can

be estimated using a Fickian diffusion model modified for ATR analysis. Shown below is an analytical expression for ATR absorbance of a chemical group associated with the diffusing molecule as a function of time [125]; this expression is applicable to weak-to-moderate IR absorption levels. The diffusion coefficient can be determined by regressing the experimental data as a function of time to Equation 9.1. Similar equations are available for Case II diffusion where the penetrant concentration front moves into the polymer with a constant velocity [201]. For multi-component diffusion, cross-term diffusion coefficients which are a measure of one component's concentration gradient on the flux of another component have also been determined [202].

$$\frac{A_t - A_0}{A_{eq} - A_0} = 1 - \frac{8\gamma}{\pi\left[1 - \exp(-2\gamma L)\right]} \times \sum_{n=0}^{\infty}\left[\frac{\exp(g)\left[f\exp(-2\gamma L) + (-1)^n(2\gamma)\right]}{(2n+1)\left(4\gamma^2 + f^2\right)}\right] \qquad (9.1)$$

where,
$$g = \frac{-D(2n+1)^2\pi^2 t}{4L^2} \qquad (9.2)$$

and
$$f = \frac{(2n+1)\pi}{2L} \qquad (9.3)$$

where, γ is the inverse of depth of penetration of evanescent wave at the wavenumber of interest (from Equation 3.6), L is the thickness of the film, and D is the diffusivity of the penetrant.

Similarly, interfacial attack should be investigated further to determine to what extent the attack must occur to delaminate the etch residue samples. Etch residues deposited on a Si ATR crystal can be monitored *in-situ* while treating residues in the cleaning solutions. However, Si ATR crystals have a useful ATR range only above 1500

cm^{-1}. Hence, some of the peaks of interest such as the asymmetric Si-O-Si stretching vibration (1010 cm^{-1}), asymmetric Si-O-C stretching vibration (1100 cm^{-1}), and C-F stretching vibration (~1220 cm^{-1}) are not detected. One possible approach to overcome this problem and have the same interface is by coating a very thin SiO_2 film (by PECVD) on a ZnSe crystal. The ZnSe crystal would allow IR spectra to be obtained in the wavenumber range of interest; since the SiO_2 is very thin, it should essentially be transparent to IR radiation. Hence, the interface can be probed under the influence of cleaning solutions.

The primary focus of this dissertation was on photoresist residues; in addition to photoresist residues, there are sidewall polymers and line-of-sight residues that need to be removed completely. SEM micrographs of the patterned samples were not conclusive in inferring if these residues were removed during CO_2-$TMAHCO_3$-methanol treatments. Since these mixtures act by undercutting, the sidewall polymer and line-of-sight residues might have also been attacked since Si-O linkages are present at the interface of these residues with the substrate. In fact, after treating a Si wafer exposed to fluorocarbon RIE plasma (to deposit fluorocarbon residues) in CO_2-$TMAHCO_3$-methanol mixture for 15 min, the fluorine concentration in the residues decreased from 17% to 9%. Since CO_2 facilitates enhanced wetting of the residues and faster penetration into high aspect ratio vias, these mixtures may easily reach the sidewall polymer and the line-of-sight residues. In order to confirm if these residues are removed, electrical testing should be performed. Electrical testing may be a more sensitive indicator of cleanliness rather than optical imaging techniques. Test structures such as the ones proposed by T. Shimmura et al. [58] (shown in Figure 9.1) may be fabricated to evaluate sidewall cleanliness. SiO_2 may be

replaced with the dielectric of choice (CORAL™ here). If sidewalls exist, the conductivity of these structures would be higher due to the unsaturated nature of the residues. In fact, such structures may also be used to evaluate different cleaning solutions for their ability to enter small vias. If incomplete removal is found, a more aggressive chemistry (such as F^-) has to be used to attack these residues. Small quantities of F^- salts (e.g. tetraalkylammonium fluoride) may be added to CO_2-$TMAHCO_3$-methanol mixture to enhance residue removal. Similar chemistries may also be used to remove residues from samples with alternative capping films such as Si_3N_4 and SiC.

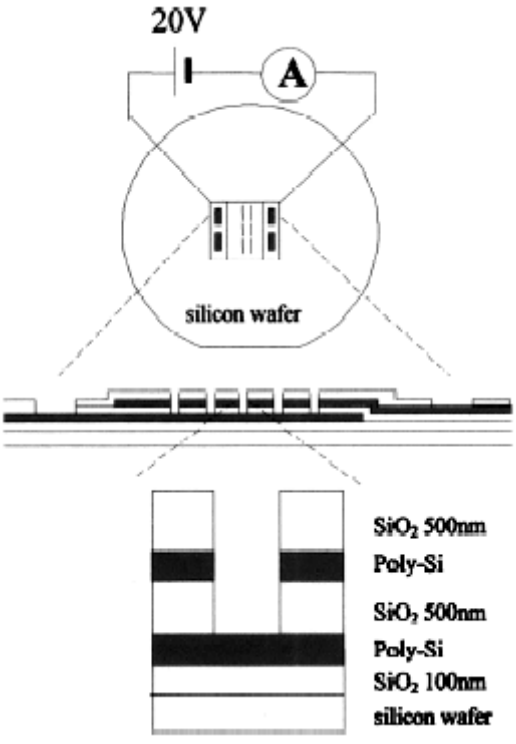

Figure 9.1. Schematic of a test structure proposed by T. Shimmura et al. that can be used to determine extent of sidewall removal [58].

As mentioned in Chapter 8, electrical tests should be performed on the porous MSSQ film to determine if small changes observed in the film by the PALS technique affect film dielectric properties. Metal-insulator-semiconductor (MIS) capacitance structures can be fabricated to determine the dielectric permittivity and loss factor of the film [203]. In addition, properties of the dielectric such as mobile charge density (from the flat band voltage shift) and minority carrier lifetimes can be determined from capacitance versus voltage and capacitance versus time plots respectively. If significant changes in properties are found, additional studies should be performed to establish if contaminants or interaction of the film with the cleaning fluids cause these effects. The samples may be treated in an alternative (clean) high pressure cell to resolve if contamination in the system is the primary cause.

The cleaning mixtures also come in contact with copper after the etch stop break through step in dual damascene processing (step g in Figure 2.2). Hence, the compatibility of these mixtures with copper should be evaluated. Corrosion inhibitors such as benzotriazole (BTA) may be used to passivate copper surfaces and prevent attack by these solutions [204].

One additional concern for integration of nitrogen containing (or basic) cleaning solutions is that residual cleaning agents may cause photoresist poisoning during the subsequent lithography step [54]. This would cause unpredictable changes in the UV dose required to develop patterns. Even trace amounts (ppb level) of such species are considered poisonous to lithography. Although XPS does not show residual $TMAHCO_3$ (from N1s peak) after cleaning and rinsing, a more sensitive technique is necessary to confirm that no salt is left behind on the sample (adsorbed to the capping layer or trapped

in the vias). Analytical techniques such as TOF-SIMS and FTIR have been used previously to detect nitrogen containing species that could potentially cause photoresist poisoning [205]. An alternative method is the 'dose compensation matrix' method [205]. In this method, the minimum dose of UV radiation required to fully develop a pattern is measured. Any residual $TMAHCO_3$ would shift this dose to higher values (since it reacts with the photoacids), which would be an indicator of poisoning. A Si wafer with small vias etched and post etch residue removed using CO_2-$TMAHCO_3$-methanol mixtures can be used as a test substrate; the dose required to pattern a second set of patterns on this substrate can be compared to the dose required for the original exposure. If any residual salts were detected, the rinsing protocol must be modified/optimized to remove the salts completely.

REFERENCES

[1] W. Shockley, *US Patent 2,569,347*, 1951.

[2] "Executive Summary," *International Technology Roadmap for Semiconductors*, Semiconductor Industry Association (2003).

[3] Gordon E. Moore, presented at *International Solid State Circuits Conference*, 2003.

[4] Gordon E. Moore, *Electronics*, **38** (8), pp. 114-117 (1965).

[5] S. A. Campbell, *The Science and Engineering of Microelectronic Fabrication*, Oxford University Press (1996).

[6] J. D. Meindl, Q. Chen, and J. A. Davis, *Science*, **293**, pp. 2044-2049 (2001).

[7] http://public.itrs.net/, accessed in Oct, 2004.

[8] L. F. Thompson, "An Introduction to Microlithography," in *Introduction to Microlithography*, L. F. Thompson, C. G. Willson, and M. J. Bowden, 2nd Edition, Washington, DC, American Chemical Society (1994).

[9] J. A. Mucha, D. W. Hess, and E. S. Aydil, "Plasma Etching," in *Introduction to Microlithography*, L. F. Thompson, C. G. Willson, and M. J. Bowden, 2nd Edition, Washington, DC, American Chemical Society (1994).

[10] S. Verhaverbeke, S. Kuppurao, C. Beaudry, and J. K. Truman, *Semiconductor International*, **25** (8), pp. 91-98 (2002).

[11] M. A. Hartney, D. W. Hess, and D. S. Soane, *Journal of Vacuum Science & Technology*, **B7** (1), pp. 1-13 (1989).

[12] K. M. Takahashi, and M. E. Gross, *Journal of The Electrochemical Society*, **146** (12), pp. 4499-4503 (1999).

[13] M. T. Spuller, *PhD Dissertation*, Georgia Insitute of Technology (2003).

[14] M. Perrut, *Industrial & Engineering Chemistry Research*, **39**, pp. 4531-4535 (2000).

[15] G. L. Weibel, and C. K. Ober, *Microelectronic Engineering*, **65**, pp. 145-152 (2003).

[16] "Interconnect," *International Technology Roadmap for Semiconductors*, Semiconductor Industry Association (2003).

[17] G. A. Brown, P. M. Zeitzoff, G. Bersuker, and H. R. Huff, *Materials Today*, **7** (1), pp. 20-25 (2004).

[18] C. K. Hu, and J. M. E. Harper, *Materials Chemistry and Physics*, **52** (1), pp. 5-16 (1998).

[19] H. Miyazaki, K. Takeda, N. Sakuma, S. Kondo, Y. Homma, and K. Hinode, *Journal of Vacuum Science & Technology*, **B15** (2), pp. 237-240 (1997).

[20] K. Choi, and C. Han, *Japanese Journal of Applied Physics, Part 1*, **37** (11), pp. 5945-5948 (1998).

[21] P. Singer, *Semiconductor International*, **22** (9), pp. 68-72 (1999).

[22] D. Shamiryan, T. Abell, F. Iacopi, and K. Maex, *Materials Today*, **7** (1), pp. 34-39 (2004).

[23] M. Morgen, E. T. Ryan, J. Zhao, C. Hu, T. Cho, and P. S. Ho, *Annual Review of Materials Science*, **30**, pp. 645-680 (2000).

[24] "Lithography," *International Technology Roadmap for Semiconductors*, Semiconductor Industry Association (2003).

[25] M. J. Bowden, "The Lithographic Process: The Physics," in *Introduction to Microlithography*, L. F. Thompson, C. G. Willson, and M. J. Bowden, 2nd Edition, Washington, DC, American Chemical Society (1994).

[26] H. Ito, *IBM Journal of Research and Development*, **45** (5), pp. 683-695 (2001).

[27] A. P. Mahorowala, and D. R. Medeiros, *Journal of Vacuum Science & Technology*, **A19** (4), pp. 1374-1378 (2001).

[28] B. Mortini, P. Spinelli, F. Leverd, V. Dejonghe, and R. Braspenning, *Proceedings of SPIE*, **5039**, pp. 847-857 (2003).

[29] G. Jordhamo, and W. Moreau, *Proceedings of SPIE*, **2724**, pp. 588-600 (1996).

[30] P. Gillespie, R. Mohondro, M. A. Jones, W. L. Krisa, and T. Romig, *Semiconductor International*, **20** (8), pp. 161-173 (1997).

[31] S. Kishimura, Y. Kimura, J. Sakai, K. Tsujita, and Y. Matsui, *Proceedings of SPIE*, **3049**, pp. 944-955 (1997).

[32] M. Matsui, T. Tatsumi, and M. Sekine, *Plasma Sources Science and Technology*, **11**, pp. A202-A205 (2002).

[33] T. E. F. M. Standaert, M. Schaepkens, N. R. Rueger, P. G. M. Sebel, G. S. Oehrlein, and J. M. Cook, *Journal of Vacuum Science & Technology*, **A16** (1), pp. 239-249 (1998).

[34] Ch Cardinaud, and G. Turban, *Applied Surface Science*, **45**, pp. 109-120 (1990).

[35] N. R. Rueger, J. J. Beulens, M. Schaepkens, M. F. Doemling, J. M. Mirza, T. E. F. M. Standaert, and G. S. Oehrlein, *Journal of Vacuum Science & Technology*, **A15** (4), pp. 1881-1889 (1997).

[36] G. S. Oehrlein, and Y. Kurogi, *Materials Science and Engineering R*, **24**, pp. 153-183 (1998).

[37] T. E. F. M. Standaert, E. A. Joseph, G. S. Oehrlein, A. Jain, W. N. Gill, Jr P. C. Wayner, and J. L. Plawsky, *Journal of Vacuum Science & Technology*, **A18** (6), pp. 2742-2748 (2000).

[38] I. Morey, and A. Asthana, *Solid State Technology*, **42** (6), pp. 71-78 (1999).

[39] M. R. Baklanov, S. Vanhaelemeersch, H. Bender, and K. Maex, *Journal of Vacuum Science & Technology*, **B17** (2), pp. 372-379 (1999).

[40] S. Lassig, S. McClatchie, and A. Kiermasz, *Semiconductor Fabtech*, **15**, pp. 185-190 (2001).

[41] S. A. Vitale, and H. H. Sawin, *Journal of Vacuum Science & Technology*, **A20** (3), pp. 651-660 (2002).

[42] C. Hibert, S. Aachboun, M. Boufnichel, and P. Ranson, *Journal of Vacuum Science & Technology*, **A19** (2), pp. 646-650 (2001).

[43] M. F. Doemling, N. R. Rueger, and G. S. Oehrlein, *Journal of Vacuum Science & Technology*, **B16** (4), pp. 1998-2005 (1998).

[44] G. S. Oehrlein, Y. Zhang, D. Vender, and M. Haverlag, *Journal of Vacuum Science & Technology*, **A12** (2), pp. 323-332 (1994).

[45] M. Schaepkens, T. E. F. M. Standaert, N. R. Rueger, P. G. M. Sebel, and G. S. Oehrlein, *Journal of Vacuum Science & Technology*, **A17** (1), pp. 26-37 (1999).

[46] G. S. Oehrlein, Y. Zhang, D. Vender, and M. Haverlag, *Journal of Vacuum Science and Technology A*, **12** (2), pp. 323-332 (1994).

[47] M. T. Radke, J. W. Coburn, and D. B. Graves, *Journal of Vacuum Science & Technology*, **A21** (4), pp. 1038-1046 (2003).

[48] Y. K. Siew, R. Joy, D. Tan, W. Liu, R. Srivastava, J. B. Tan, and L. Hsia, *Semiconductor International*, **26** (9), pp. 62-66 (2003).

[49] T. Tatsumi, K. Nagahata, T. Saitoh, and Y. Morita, *Proceedings of the IEEE International Interconnect Technology Conference*, pp. 239-241 (2003).

[50] H. Doh, J. Kim, and K. Whang, *Journal of Vacuum Science & Technology*, **A14** (3), pp. 1088-1091 (1996).

[51] Y. Wang, S. W. Graham, L. Chan, and S. Loong, *Journal of The Electrochemical Society*, **144** (4), pp. 1522-1528 (1997).

[52] D. Beery, K. Reinhardt, P. B. Smith, J. Kelley, and A. Sivasothy, *Proceedings of the IEEE International Interconnect Technology Conference*, pp. 140-142 (1999).

[53] W. Kleemeier, V. Leon, and S. Graham, *Diffusion and Defect Data, Part B*, **65-66**, pp. 143-152 (1999).

[54] O. Louveau, D. Louis, M. Assous, R. Blanc, P. Brun, S. Lamy, and E. Lajoinie, *Microelectronic Engineering*, **61-62**, pp. 867-874 (2002).

[55] A. Somasekhar, H. Ying, P. B. Smith, D. B. Aldrich, and R. J. Nemanich, *Journal of The Electrochemical Society*, **146** (6), pp. 2318-2321 (1999).

[56] G. N. Liu, N. Ikegami, H. Uchida, N. Hirashita, and J. Kanamori, *Journal of Vacuum Science & Technology*, **B17** (2), pp. 355-361 (1999).

[57] D. Louis, A. Beverina, C. Arvet, E. Lajoinie, C. Peyne, D. Holmes, and D. Maloney, *Microelectronic Engineering*, **57-58**, pp. 621-627 (2001).

[58] T. Shimmura, S. Soda, S. Samukawa, M. Koyanagi, and K. Hane, *Journal of Vacuum Science & Technology*, **B20** (6), pp. 2346-2350 (2002).

[59] I. Tohno, M. Saito, K. Omiya, and Y. Kataoka, *Japanese Journal of Applied Physics, Part 1*, **40**, pp. 798-802 (2001).

[60] G. Hills, *Semiconductor International*, **24** (7), pp. 193-196 (2001).

[61] R. Kwong, W. Moreau, and W. Yan, *Proceedings of SPIE*, **3678**, pp. 1209-1214 (1999).

[62] H. Motomura, S. Imai, and K. Tachibana, *Thin Solid Films*, **390**, pp. 134-138 (2001).

[63] T. Kropewnicki, D. Doan, B. Tang, and C. Bjorkman, *Journal of Vacuum Science & Technology*, **A19** (4), pp. 1384-1387 (2001).

[64] M. R. Breen, C. M. Foster, S. Bass, J. J. Lee, and W. Mlynko, *Journal of Vacuum Science & Technology*, **B18** (3), pp. 1314-1321 (2000).

[65] J. R. Hu, W. Uesato, P. Schoenborn, P. Clark, M. Boumerzoug, and H. Xu, presented at *AVS First International Conference on Microelectronics and Interfaces*, 2000.

[66] D. L. Flamm, *Solid State Technology*, **35** (9), pp. 43-48 (1992).

[67] C. Yeh, Y. Lee, Y. Su, K. Wu, and C. Lin, *Proceedings of the International Symposium on Plasma Process-Induced Damage*, pp. 81-84 (2000).

[68] D. Shamiryan, M. R. Baklanov, S. Vanhaelemeersch, and K. Maex, *Journal of Vacuum Science & Technology*, **B20** (5), pp. 1923-1928 (2002).

[69] P. G. Clark, B. D. Schwab, J. W. Butterbaugh, H. J. Martinez, and P. J. Wolf, *Semiconductor International*, **26** (9), pp. 46-52 (2003).

[70] D. Louis, C. Arvet, E. Lajoinie, C. Peyne, S. Lee, I. Berry, and Q. Han, *Microelectronic Engineering*, **53**, pp. 381-384 (2000).

[71] D. Louis, E. Lajoinie, F. Pires, W. M. Lee, and D. Holmes, *Microelectronic Engineering*, **41-42**, pp. 415-418 (2002).

[72] Y. Lee, S. Loong, M. Zhou, and Y. Lu, *Journal of The Electrochemical Society*, **145** (11), pp. 3966-3973 (1998).

[73] K. Ueno, V. M. Donnelly, and T. Kikkawa, *Journal of The Electrochemical Society*, **144** (7), pp. 2565-2572 (1997).

[74] L. Archer, S. Henry, and D. Nachreiner, *Micro*, **19** (6), pp. 95 (2001).

[75] D. Louis, C. Peyne, C. Arvet, E. Lajoinie, D. Maloney, and S. Lee, *Proceedings of the IEEE International Interconnect Technology Conference*, pp. 103-105 (1999).

[76] D. Louis, E. Lajoinie, D. Holmes, S. Lee, and C. Peyne, *Proceedings of SPIE*, **3333**, pp. 1420-1425 (1998).

[77] R. Small, S. Kirk, and M. Cernat, *Journal of Vacuum Science & Technology*, **B20** (2), pp. 635-639 (2002).

[78] S. Ma, R. Parker, R. Kavari, I. Leal, and D. G. Boyers, *Proceedings of the IEEE International Interconnect Technology Conference*, pp. 46-48 (2000).

[79] S. De Gendt, P. Snee, I. Cornelissen, M. Lux, R. Vos, P. W. Mertens, D. M. Knotter, M. M. Meuris, and M. Heyns, *Diffusion and Defect Data, Part B*, **65-66**, pp. 165-168 (1998).

[80] C. R. Olson, J. J. Rosato, and J. A. Fahrenkrug, *Proceedings of the Sixth International Symposium on Cleaning Technology in Semiconductor Device Manufacturing*, **PV 99-36**, pp. 327-334 (2000).

[81] "Environment, Safety, and Health," *International Technology Roadmap for Semiconductors*, Semiconductor Industry Association (2003).

[82] A. Hand, *Semiconductor International*, **24** (9), pp. 62-66 (2001).

[83] M. T. Spuller, and D. W. Hess, *Journal of The Electrochemical Society*, **158** (8), pp. G476-G480 (2003).

[84] Y. Jincao, M. A. Matthews, and C. H. Darwin, *Industrial & Engineering Chemistry Research*, **40**, pp. 5858-5860 (2001).

[85] D. L. Goldfarb, J. J. de Pablo, P. F. Nealey, J. P. Simons, W. M. Moreau, and M. Angelopoulos, *Journal of Vacuum Science & Technology*, **B18** (6), pp. 3313-3317 (2000).

[86] H. Namatsu, *Journal of Vacuum Science & Technology*, **B18** (6), pp. 3308-3312 (2000).

[87] R. H. Perry, and D. W. Green, *Perry's Chemical Engineers' Handbook*, 7th Edition, McGraw-Hill Professional (1997).

[88] A. Iezzi, R. Enick, and J. Brady, "Direct Viscosity Enhancement of Carbon Dioxide," in *Supercritical Fluid Science and Technology*, K. P. Johnston, and J. M. L. Penninger, Washington, DC, American Chemical Society (1989).

[89] R. Purtell, L. Rothman, B. Eldridge, and C. Chess, *Journal of Vacuum Science & Technology*, **A11** (4), pp. 1696-1701 (1993).

[90] M. M. Hills, *Journal of Vacuum Science & Technology*, **A13** (1), pp. 30-34 (1995).

[91] C. K. Ober, A. H. Gabor, P. Gallagher-Wetmore, and R. D. Allen, *Advanced Materials*, **9** (13), pp. 1039-1043 (1997).

[92] E. N. Hoggan, D. Flowers, J. M. DeSimone, and R. G. Carbonell, *Proceedings of SPIE*, **4690 II**, pp. 1217-1223 (2002).

[93] H. G. P. Lewis, G. L. Weibel, C. K. Ober, and K. K. Gleason, *Chemical Vapor Deposition*, **7** (5), pp. 195-197 (2001).

[94] C. Shi, Z. Huang, S. Kilic, J. Xu, R. M. Enick, E. J. Beckman, A. J. Carr, R. E. Melendez, and A. D. Hamilton, *Science*, **286**, pp. 1540 (1999).

[95] N. Kawakami, Y. Fukumoto, T. Kinoshita, K. Suzuki, and K. Inoue, *Proceedings of the IEEE International Interconnect Technology Conference*, pp. 143-145 (2000).

[96] R. A. Pai, R. Humayun, M. T. Schulberg, A. Sengupta, J. Sun, and J. J. Watkins, *Science*, **303**, pp. 507-510 (2004).

[97] D. P. Long, J. M. Blackburn, and J. J. Watkins, *Advanced Materials*, **12** (12), pp. 913-915 (2000).

[98] J. M. Blackburn, D. P. Long, A. Cabanas, and J. J. Watkins, *Science*, **294**, pp. 141-145 (2001).

[99] E. Bok, D. Kelch, and K. S. Schumacher, *Solid State Technology*, **35** (6), pp. 117-120 (1992).

[100] X. Zhang, J. Q. Pham, N. Ryza, P. F. Green, and K. P. Johnston, *Journal of Vacuum Science & Technology*, **B22** (2), pp. 818-825 (2004).

[101] E. L. V. Goetheer, M. A. G. Vorstman, and J. T. F. Keurentjes, *Chemical Engineering Science*, **54**, pp. 1589-1596 (1999).

[102] S. G. Kazarian, M. F. Vincent, F. V. Bright, C. L. Liotta, and C. A. Eckert, *Journal of the American Chemical Society*, **118**, pp. 1729-1736 (1996).

[103] K. F. Webb, and A. S. Teja, *Fluid Phase Equilibria*, **158-160**, pp. 1029-1034 (1999).

[104] S. M. Sirard, K. J. Ziegler, I. C. Sanchez, P. F. Green, and K. P. Johnston, *Macromolecules*, **35**, pp. 1928-1935 (2002).

[105] J. B. Rubin, L. B. Davenhall, C. M. V. Taylor, L. D. Sivils, T. Pierce, and K. Tiefert, *Proceedings of the IEEE International Symposium on Electronics and the Environment*, pp. 13-20 (1999).

[106] J. M. DeSimone, *Science*, **297**, pp. 799-803 (2002).

[107] V. Perrut, A. Danel, C. Millet, J. Daviot, M. Rignon, and F. Tardif, *Proceedings of the International Symposium on Cleaning Technology in Semiconductor Device Manufacturing VII*, **25**, pp. 246-253 (2003).

[108] Vaartstra, *US Patent 6,242,165*, 2001.

[109] W. H. Mullee, M. A. Biberger, and P. E. Schilling, *World Patent 01/33613*, 2001.

[110] J. M. DeSimone, T. Romack, D. E. Betts, and J. B. McClain, *US Patent 5,783,082*, 1998.

[111] P. M. Wetmore, V. J. Krukonis, and M. P. Coffey, *US Patent 5,514,220*, 1996.

[112] M. Nishikawa, K. Nakagawa, and Y. Yamaguchi, *US Patent 4,944,837*, 1990.

[113] J. Klier, C. J. Tucker, T. H. Kalantar, and D. P. Green, *Advanced Materials*, **12** (23), pp. 1751-1757 (2000).

[114] J. B. McClain, D. E. Betts, D. A. Canelas, E. T. Samulski, J. M. DeSimone, J. D. Londono, H. D. Cochran, G. D. Wignall, D. Chillura-Martino, and R. Triolo, *Science*, **274**, pp. 2049-2051 (1996).

[115] W. Ryoo, S. E. Webber, and K. P. Johnston, *Industrial & Engineering Chemistry Research*, **42** (25), pp. 6348-6358 (2003).

[116] Z. Guan, and J. M. DeSimone, *Macromolecules*, **27**, pp. 5527-5532 (1994).

[117] W. Guo, Z. Li, B. M. Fung, E. A. O'Rear, and J. H. Harwell, *Journal of Physical Chemistry*, **96**, pp. 6738-6742 (1992).

[118] X. Zhang, J. Q. Pham, H. J. Martinez, P. J. Wolf, P. F. Green, and K. P. Johnston, *Journal of Vacuum Science & Technology*, **B21** (6), pp. 2590-2598 (2003).

[119] D. A. Skoog, D. M. West, and F. J. Holler, *Fundamentals of Analytical Chemistry*, 6th Edition, Saunders College Publishing (1992).

[120] D. Briggs, and M. P. Seah, *Practical Surface Analysis: Auger and X-Ray Photoelectron Spectroscopy*, 2nd Edition, John Wiley & Sons Ltd (1996).

[121] M. P. Seah, and M. T. Anthony, *Surface and Interface Analysis*, **6** (5), pp. 230-241 (1984).

[122] J. Diao, and D. W. Hess, *Journal of Electron Spectroscopy and Related Phenomena*, **135** (2-3), pp. 87-104 (2004).

[123] M. W. Urban, *Attenuated Total Reflection Spectroscopy of Polymers*, Washington, DC, American Chemical Society (1996).

[124] P. Sutandar, D. J. Ahn, and E. I. Franses, *Macromolecules*, **27** (25), pp. 7316-7328 (1994).

[125] Y. A. Elabd, M. G. Baschetti, and T. A. Barbari, *Journal of Polymer Science, Part B*, **41**, pp. 2794-2807 (2003).

[126] www.harrricksci.com, accessed in Oct, 2004.

[127] T. Kamal, *PhD Dissertation*, Georgia Institute of Technology (2000).

[128] G. Socrates, *Infrared Characteristic Group Frequencies*, 2nd Edition, Chichester, John Wiley & Sons (1994).

[129] A. Agrawal, and C. L. Henderson, *Proceedings of SPIE*, **5038 II**, pp. 1026-1037 (2003).

[130] N. Layadi, S. J. Molloy, T. C. Esry, T. Lill, J. Trevor, M. N. Grimbergen, and J. Chinn, *Journal of Vacuum Science & Technology*, **B17** (6), pp. 2630-2637 (1999).

[131] O. S. Heavens, *Optical Properties of Thin Solid Films*, New York, Dover Publications (1991).

[132] H. G. Tompkins, *Spectroscopic Ellipsometry and Reflectometry*, New York, Wiley-Interscience (1999).

[133] www.jawoollam.com, accessed in Oct, 2004.

[134] *Guide to Using WVASE32^{TM}*, J. A. Woollam, Co.

[135] K. Maex, M. R. Baklanov, D. Shamiryan, F. Iacopi, S. H. Brongersma, and Z. S. Yanovitskaya, *Journal of Applied Physics*, **93** (11), pp. 8793-8841 (2003).

[136] J. N. Sun, D. W. Gidley, Y. Hu, W. E. Frieze, and E. T. Ryan, *Applied Physics Letters*, **81** (8), pp. 1447-1449 (2002).

[137] J. N. Sun, Y. Hu, W. E. Frieze, W. Chen, and D. W. Gidley, *Journal of The Electrochemical Society*, **150** (5), pp. F97-F101 (2003).

[138] J. N. Sun, D. W. Gidley, Y. F. Hu, W. E. Frieze, and S. Yang, *Materials Research Society Symposium - Proceedings*, **726**, pp. 311-322 (2002).

[139] http://positrons.physics.lsa.umich.edu, accessed in Oct, 2004.

[140] J. N. Sun, Y. F. Hu, W. E. Frieze, and D. W. Gidley, *Radiation Physics and Chemistry*, **68**, pp. 345-349 (2003).

[141] M. P. Petkov, M. H. Weber, K. G. Lynn, and K. P. Rodbell, *Applied Physics Letters*, **77** (16), pp. 2470-2472 (2000).

[142] Y. Ito, "Radiation Chemistry: Intraspur Effects and Positronium Formation Mechanisms," in *Positron and Positronium Chemistry*, D. M. Schrader, and Y. C. Jean, Amsterdam, Elsevier Science Publishing Company, pp. 120-158 (1988).

[143] www.sematech.org, accessed in Oct, 2004.

[144] K. MacWilliams, K. Huang, M. Schulberg, and P. Van Cleemput, presented at *IEEE International Symposium on Semiconductor Manufacturing (ISSIM)*, 2001.

[145] L. Peters, *Semiconductor International*, **22** (13), pp. 56-64 (1999).

[146] A. Das, T. Kokubo, Y. Furukawa, H. Struyf, I. Vos, B. Sijmus, F. Iacopi, J. Van Aelst, Q. T. Le, L. Carbonell, S. Brongersma, M. Maenhoudt, Z. Tokei, I. Vervoort, E. Sleeckx, M. Stucchi, M. Schaekers, W. Boullart, E. Rosseel, M. Van Hove, S. Vanhaelemeersch, A. Shiota, andK. Maex, *Microelectronic Engineering*, **64** (1-4), pp. 25-33 (2002).

[147] G. S. Oehrlein, J. G. Clabes, and P. Spirito, *Journal of The Electrochemical Society*, **133** (5), pp. 1002-1008 (1986).

[148] H. Park, K. Kwon, J. Lee, K. Suh, O. Kwon, K. Cho, and S. Park, *Journal of Applied Physics*, **76** (8), pp. 4596-4602 (1994).

[149] J. F. Moulder, W. F. Stickle, P. E. Sobol, and K. D. Bomben, *Handbook of X-ray Photoelectron Spectroscopy*, Physical Electronics, Inc. (1995).

[150] C. L. McAdams, L. W. Flanagin, C. L. Henderson, A. R. Pawloski, P. Tsiartas, and C. G. Willson, *Proceedings of SPIE*, **3333**, pp. 1171-1179 (1998).

[151] R. Bashir, J. Z. Hilt, O. Elibol, A. Gupta, and N. A. Peppas, *Applied Physics Letters*, **81** (16), pp. 3091-3093 (2002).

[152] M. Padmanaban, J. Bae, M. Cook, W. Kim, A. Klauck-Jacobs, T. Kudo, M. D. Rahman, R. R. Dammel, and J. D. Byers, *Proceedings of SPIE*, **3999 II**, pp. 1136-1146 (2000).

[153] S. Oswald, and S. Baunack, *Thin Solid Films*, **425** (1-2), pp. 9-19 (2003).

[154] Th Albers, M. Neumann, D. Lipinsky, L. Wiedmann, and A. Benninghoven, *Surface and Interface Analysis*, **22** (1), pp. 9-13 (1994).

[155] S. Agraharam, D. W. Hess, P. A. Kohl, and S. A. B. Allen, *Journal of Vacuum Science & Technology*, **B19** (2), pp. 439-446 (2001).

[156] W. Kern, *Handbook of Semiconductor Wafer Cleaning Technology: Science, Technology and Applications*, New Jersey, Noyes Publications (1993).

[157] H. Ito, *Journal of Polymer Science, Part A*, **41**, pp. 3863-3870 (2003).

[158] B. A. Miller-Chou, and K. L. Koenig, *Progress in Polymer Science*, **28**, pp. 1223-1270 (2003).

[159] B. Hunek, and E. L. Cussler, *AIChE Journal*, **48** (4), pp. 661-672 (2002).

[160] P. C. Tsiartas, L. W. Flanagin, C. L. Henderson, W. D. Hinsberg, I. S. Sanchez, R. T. Bonnecaze, and C. G. Willson, *Macromolecules*, **30**, pp. 4656-4664 (1997).

[161] A. Reiser, Z. Yan, Y. Han, and M. S. Kim, *Journal of Vacuum Science & Technology*, **B18** (3), pp. 1288-1293 (2000).

[162] K. L. Chavez, and D. W. Hess, *Journal of The Electrochemical Society*, **150** (4), pp. G284-G291 (2003).

[163] "Alternative disinfection," in *Cleanroom Technology*, vol. 10, pp. 27-28 (2004).

[164] R. Wiebe, *Chemical Reviews*, **29**, pp. 475-481 (1941).

[165] S. Yeo, S. Park, J. Kim, and J. Kim, *Journal of Chemical and Engineering Data*, **45**, pp. 932-935 (2000).

[166] L. L. Williams, E. M. Mas, and J. B. Rubin, *Journal of Chemical and Engineering Data*, **47**, pp. 282-285 (2002).

[167] T. S. Reighard, S. T. Lee, and S. V. Olesik, *Fluid Phase Equilibria*, **123**, pp. 215-230 (1996).

[168] H. Byun, K. Kim, and M. A. McHugh, *Industrial & Engineering Chemistry Research*, **39**, pp. 4580-4587 (2000).

[169] T. Kamal, and D. W. Hess, *Journal of Vacuum Science & Technology*, **B19** (2), pp. 461-466 (2001).

[170] K. R. Williams, and R. S. Muller, *Journal of Microelectromechanical Systems*, **5** (4), pp. 256-269 (1996).

[171] O. Tabata, R. Asahi, H. Funabashi, K. Shimaoka, and S. Sugiyama, *Sensors and Actuators*, **A34** (1), pp. 51-57 (1992).

[172] T. M. Pan, T. F. Lei, F. S. Ko, T. S. Chao, T. H. Chiu, Y. H. Lee, and C. P. Lu, *IEEE Transactions on Semiconductor Manufacturing*, **14** (4), pp. 365-371 (2001).

[173] H. Satoh, M. Fukui, and C. Kawakami, *US Patent 5,354,434*, 1994.

[174] S. A. Nolen, J. Lu, J. S. Brown, P. Pollet, B. C. Eason, K. N. Griffith, R. Glaser, D. Bush, D. R. Lamb, C. L. Liotta, andC. A. Eckert, *Industrial & Engineering Chemistry Research*, **41**, pp. 316-323 (2002).

[175] J. L. Ellingboe, and J. H. Runnels, *Journal of Chemical and Engineering Data*, **11**, pp. 323-324 (1966).

[176] A. Y. Platonov, A. N. Evdokimov, A. V. Kurzin, and H. D. Maiyorova, *Journal of Chemical and Engineering Data*, **47** (5), pp. 1175-1176 (2002).

[177] S. T. Lee, T. S. Reighard, and S. V. Olesik, *Fluid Phase Equilibria*, **122** (1-2), pp. 223-241 (1996).

[178] A. K. Dillow, S. L. J. Yun, D. Suleiman, D. L. Boatright, C. L. Liotta, and C. A. Eckert, *Industrial & Engineering Chemistry Research*, **35** (6), pp. 1801-1806 (1996).

[179] G. Levitin, D. Bush, C. A. Eckert, and D. W. Hess, *Journal of Chemical and Engineering Data*, **49** (3), pp. 599-606 (2004).

[180] T. Adrian, M. Wendland, H. Hasse, and G. Maurer, *Journal of Supercritical Fluids*, **9** (1), pp. 19-25 (1998).

[181] M. A. Biberger, P. Schilling, D. Frye, and M. E. Mills, *Semiconductor Fabtech*, **12**, pp. 239-243 (2000).

[182] J. J. Rosato, E. G. Baiya, J. A. Imonigie, M. R. Yalamanchili, and E. Hansen, *Future Fab International*, **13**, pp. 236-242 (2002).

[183] Y. Kim, M. R. Baklanov, T. Conard, M. de Potter, and S. Vanhaeleemeersch, *Journal of The Electrochemical Society*, **146** (4), pp. 1549-1556 (1999).

[184] R. J. Carter, T. P. Schneider, J. S. Montgomery, and R. J. Nemanich, *Journal of The Electrochemical Society*, **141** (11), pp. 3136-3140 (1994).

[185] F. Lanckmans, M. Baklanov, C. Alaerts, S. Vanhaelemeersch, and K. Maex, *Diffusion and Defect Data, Part B*, **65-55**, pp. 89-92 (1999).

[186] M. Jolley, *Diffusion and Defect Data, Part B*, **65-55**, pp. 105-108 (1999).

[187] R. T. Morrison, and R. N. Boyd, *Organic Chemistry*, 3rd Edition, Boston, Allyn and Bacon, Inc. (1974).

[188] T. K. Markkula, J. A. Hunt, F. R. Pu, and R.L. R. L. Williams, *Surface and Interface Analysis*, **34** (1), pp. 583-587 (2002).

[189] T. Cao, K. P. Johnston, and S. E. Webber, *Macromolecules*, **37**, pp. 1897-1902 (2004).

[190] "NIST Electron Effective-Attenuation-Length Database - Version 1.0," C. J. Powell, and A. Jablonski (2001).

[191] B. Rumpf, J. Xia, and G. Maurer, *Industrial & Engineering Chemistry Research*, **37**, pp. 2012-2019 (1998).

[192] L. Costa, L. Rossi di Montelera, G. Camino, E. D. Weil, and E. W. Pearce, *Polymer Degradation and Stability*, **56**, pp. 23-35 (1997).

[193] T. Usami, K. Shimokawa, and M. Yoshimaru, *Japanese Journal of Applied Physics, Part 1*, **33** (1B), pp. 408-412 (1994).

[194] A. Nara, and H. Itoh, *Japanese Journal of Applied Physics, Part 1*, **36**, pp. 1477-1480 (1997).

[195] J. D. Lamb, and J. A. Woollam, *Extended Abstracts and Program - Biennial Conference on Carbon*, pp. 216 (1985).

[196] S. Takeishi, H. Kudo, R. Shinohara, M. Hoshino, S. Fukuyama, J. Yamaguchi, and M. Yamada, *Journal of The Electrochemical Society*, **144** (5), pp. 1797-1802 (1997).

[197] R. Sharangpani, R. Singh, M. Drews, and K. Ivey, *Journal of Electronic Materials*, **26** (4), pp. 402-409 (1997).

[198] C. V. Nguyen, K. R. Carter, C. J. Hawker, J. L. Hedrick, R. L. Jaffe, R. D. Miller, J. F. Remenar, H. Rhee, P. M. Rice, M. F. Toney, M. Trollsås, andD. Y. Yoon, *Chemistry of Materials*, **11**, pp. 3080-3085 (1999).

[199] G. Levitin, S. Myneni, and D. W. Hess, *Journal of The Electrochemical Society*, **151** (6), pp. 1-7 (2004).

[200] M. P. Petkov, M. H. Weber, K. G. Lynn, and K. P. Rodbell, *Applied Physics Letters*, **79** (23), pp. 3884-3886 (2001).

[201] G. T. Fieldson, and T. A. Barbari, *AIChE Journal*, **41** (4), pp. 795-804 (1995).

[202] Y. A. Elabd, and T. A. Barbari, *AIChE Journal*, **48** (8), pp. 1610-1620 (2002).

[203] P. S. Burggraaf, *Semiconductor International*, **3** (9), pp. 29-42 (1980).

[204] T. Koito, K. Hirano, and K. Nakabeppu, *IEEE Transactions on Semiconductor Manufacturing*, **15** (4), pp. 429-433 (2002).

[205] S. Lamy, O. Louveau, G. Fanget, M. Fayolle, N. Rochat, D. Louis, and L. Broussous, *Proceedings of the IEEE International Interconnect Technology Conference*, pp. 30-32 (2002).

VITA

Satyanarayana Myneni was born on August 30, 1979, in Madhira, India, to Murali Krishna and Venkata Ramulu Myneni. After schooling in Kothagudem and Hyderabad, he attended Indian Institute of Technology, Madras, where he obtained Bachelor of Technology degree in Chemical Engineering in the year 2000. Soon after, he came to the US to pursue graduate study at Georgia Institute of Technology, Atlanta. He obtained his PhD in Chemical Engineering in December, 2004, and is currently employed as a Sr. Process Engineer at Intel, Santa Clara.